UNIVERSITY OF CALIFORNIA,
IRVINE

Spin Torque Oscillators

DISSERTATION

submitted in partial satisfaction of the requirements
for the degree of

DOCTOR OF PHILOSOPHY

in Physics

by

Christopher Safranski

Thesis Committee:
Professor Ilya Krivorotov, Chair
Donald Bren Professor Wilson Ho
Professor Zuzanna Siwy

2018

TABLE OF CONTENTS

LIST OF FIGURES

ACKNOWLEDGMENTS

First off I would like to thank my advisor Ilya Krivorotov for the chance to work under him for these years. Not only has he been incredibly supportive, but patient as well when there are large gaps in knowledge. Also I would like to thank him for his monumental efforts to ensure that everyone in the lab was funded and was able to get the tools needed to further our research. I would also like to acknowledge the helpful group he has help put together which without, it would have been impossible to learn so much in these past years. Whether it be learning the first few things about the lab with Alejandro Jara, nanofab from Andrew Smith and Liu Yang, or Igor Barsukov handling the first round of questions all the time. I thank Eric Montoya for all the help and knowledge as well. I would like to also thank Yu-Jin Chen, Jen-Ru Chen, Han Kyu Lee, Chengcen Sha, Brian Youngblood, Jieyi Zhang for all the conversations about research and the sharing of knowledge. I also would like to thank those I worked with during my internship at IBM, Jonathan Sun and Ching–Tzu Chen, for helping me learn new techniques and materials and giving me a chance to come work there.

CURRICULUM VITAE

Christopher Safranski

EDUCATION

Doctor of Philosophy in Physics — **2018**
University of California Irvine — *Irvine, Ca*

Master of Science in Physics — **2016**
University of California Irvine — *Irvine, Ca*

Master of Science in Applied Physics — **2012**
California State University Long Beach — *Long Beach, Ca*

Bachelor of Science in Physics — **2010**
California Polytechnic State University at San Luis Obispo — *San Luis Obispo, Ca*

RESEARCH EXPERIENCE

Graduate Research Assistant — **2013–2016**
University of California, Irvine — *Irvine, Ca*

Internship — **Summer 2015 and 2016**
IBM T. J. Watson Research Center — *Yorktown Heights, NY*

TEACHING EXPERIENCE

Teaching Assistant — **2012–2013**
University of California, Irvine — *Irvine, Ca*

Teaching Assistant — **2010–2012**
California State University Long Beach — *Long Beach, Ca*

PUBLICATIONS

C. Safranski, E. A. Montoya, and I. N. Krivorotov. *Planar Hall Torque.* arXiv:1712.07335 (2017)

M. Evelt, **C. Safranski**, Mohammed Aldosary, V. E. Demidov, I. Barsukov, A. P. Nosov, A. B. Rinkevich, K. Sobotkiewich, Xiaoqin Li, Jing Shi, I. N. Krivorotov and S. O. Demokritov. *Spin Hall-induced auto-oscillations in ultrathin YIG grown on Pt.* Sci. Rep. **8**, 1269 (2018).

C. Safranski, I. Barsukov, H. K. Lee,T. Schneider, A. A. Jara, A. Smith, H. Chang, K. Lenz, J. Lindner, Y. Tserkovnyak, M.Wu, and I. N. Krivorotov. *Spin calortronic nano-oscillator*, Nat Commun **8**, 117 (2017)

C. J. Safranski, Y.-J. Chen, I. N. Krivorotov and J. Z. Sun, *Material parameters of perpendicularly magnetized tunnel junctions from spin torque ferromagnetic resonance techniques*, Appl. Phys. Lett. **109**, 132408 (2016)

I. Barsukov , Y. Fu , **C. Safranski** , Y, Chen , B. Youngblood , A. Gonalves , M. Spasova , M. Farle , J. Katine , C. C. Kuo, I. N. Krivorotov. *Magnetic phase transitions in Ta/CoFeB/MgO multilayers,* Appl. Phys. Lett. **106**, 192407 (2015)

A. Jara, **C. Safranski**, I. Krivorotov, C. T. Wu, A. Malmi-Kakkada, K. Halterman, *Angular dependence of superconductivity in superconductor/spin-valve heterostructures*, Phys. Rev. B **89**, 184502 (2014).

CONFERENCE PRESENTATIONS

C, Safranski, E. Montoya, A. Smith, J.-R. Chen, I. Krivorotov. *"Easy-Plane Spin Hall Nano-Oscillator,"* APS March Meeting, 2018

C. Safranski, E. Montoya, A. Smith, J.-R. Chen, I. Krivorotov. *"Spin torque ferromagnetic resonance for probing magnetic disorder in nanostructures,"* MMM 2017

C. Safranski , I. Krivorotov , C.-T. Chen , J. Sun. *"Thermal spin current control of magnetic damping in Py/Ag/CoFe2O4/Pt multilayers,"* APS March Meeting, 2017

C. Safranski, I. Barsukov, H. K. Lee, T. Schneider, A. Jara, A. Smith, H. Chang, Y. Tserkovnyak, M. Wu, I. Krivorotov. *"Spin current control of damping in YIG/Pt nanowires,"* APS March Meeting, 2016

C. Safranski, I. Barsukov, H. K. Lee, T. Schneider, A. Jara, A. Smith, H. Chang, Y. Tserkovnyak, M. Wu, I. Krivorotov. *"Spin current control of damping in YIG/Pt nanowires,"* 13th Joint MMM-Intermag Conference, 2016

ABSTRACT OF THE DISSERTATION

Spin Torque Oscillators

By

Christopher Safranski

Doctor of Philosophy in Physics

University of California, Irvine, 2018

Professor Ilya Krivorotov, Chair

Manipulation of magnetic materials by the spin degree of freedom is leading way to a new generation of electronics known as spintronics. The nanodevices using these properties are becoming attractive candidates for electronics applications, since they may lead way to less power consumption than their semiconductor counterparts. One particular device of interest is the spin toque oscillator, which is a nanoscale source of microwave power. In this study, multiple types of these devices are fabricated but specifically two novel methods of driving these devices is discovered in the process. One method is based on magnon condensation through the spin Seebeck effect, where high thermal gradients across a magnetic insulator drive a spin current. The second method involved the discovery of a novel spin orbit torque linked to the planer Hall effect present in ferromagnetic materials. The source of the spin orbit torque not only originates from spin currents produced in the ferromagnet, but the action of this torque exhibits a novel angular symmetry in the plane defined by the charge current flow and substrate normal.

Chapter 1

Introduction

The manipulation of the spin degree of freedom has an important role in the development of novel electronic nanodevices with the hope to significantly reduce the power needed to operate devices. With the ever increasing amount of nanodevices inside modern electronics, even a slight reduction in needed power per nanodevice will translate to a large amount of energy savings on a global scale. When speaking of the electronic devices designed in the past several decades, the most common theme is the movement of charge current mediated by electrons. This approach only takes into account the inherent charge of the electron and overlooks another important characteristic, its spin. An electron has a quantized unit of angular momentum and simply put, can be thought of as a charged bar magnet. In traditional electronics this property is overlooked since the spins in simple materials are randomly distributed, resulting in zero net moment. Recently, experiments in polarizing the charge current has given rise to the field of spintronics.

To understand how the spin degree of freedom can be manipulated and used to build a device, we will first consider a toy model. In this model shown in Figure 1.1, say we pass an electron gas through a region (Reference Layer) with a strong magnetic field. The electron's

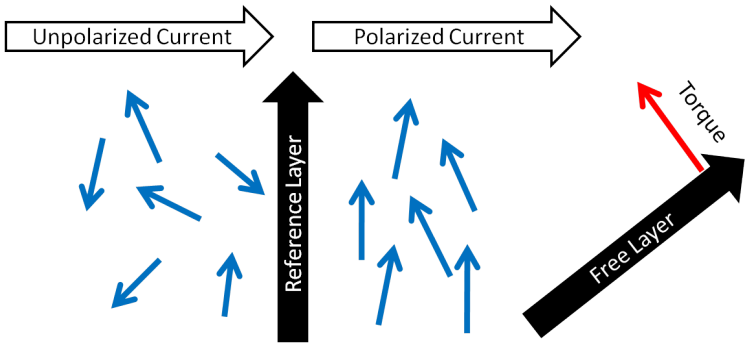

Figure 1.1: Toy model of the concept of spin torque, where charge current gets polarized by a field and then can exert a torque on a magnet.

moment, as indicated by the blue arrows, will be aligned with the field from the region it passed through. If this polarized current is then passed into another moment (free layer), then they will exert a force on it. The interaction of spin current on a magnetic moment is called spin torque [1, 2]. Experimentally, application of large spin currents to a free magnetic layer have been shown to induce switching in multiple experiments [3–6].

While the observation of magnetic switching is important for technical applications, just considering this binary experiment ignores a rich amount of physics. In order to understand other phenomena, the basic principles of magnetization dynamics need to be understood. First, lets consider a magnetic moment sitting in a magnetic field. At equilibrium, the magnetic moment will align with the magnetic field. If it where then pulled out of equilibrium and released, it would then begin to oscillate around its equilibrium position conceptually much like a mass on a spring. However, unlike the simple nature of the restoring force for a mass on a spring, the magnetization obeys what is known as the LandauLifshitzGilbert (LLG) equation[7, 8]:

$$\frac{\partial \mathbf{M}}{\partial t} = -\gamma \left[\mathbf{M} \times \mathbf{H}_{\text{eff}}\right] + \frac{\alpha}{M_{\text{s}}} \left[\mathbf{M} \times \frac{\partial \mathbf{M}}{\partial t}\right], \tag{1.1}$$

Rather that oscillating back and forth like a mass on a spring, a more accurate mechanical analog of the resulting motion is a spinning top. A spinning top will precess about its

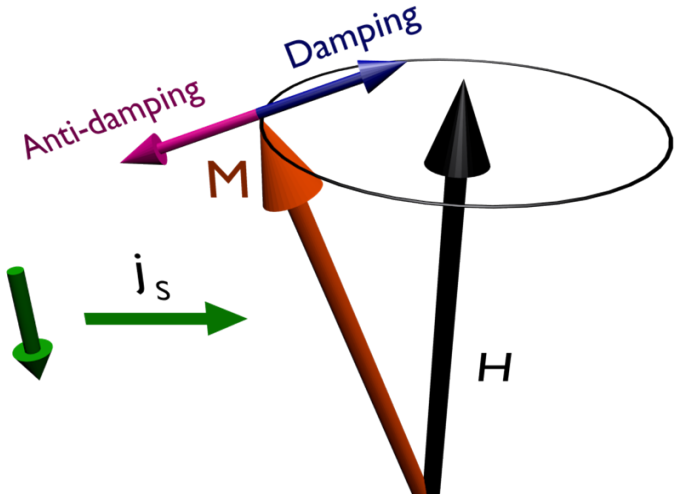

Figure 1.2: Precession of magnetization around an effective magnetic field with damping torques.

angular momentum vector as it begins to fall over and much like this, the magnetization ($\mathbf{M}$) precesses about an effective field (H_{eff})like illustrated in Figure 1.2. The LLG equation contains two important parts. First is the field torque which is analogous to the stiffness of a spring for a harmonic oscillator and provides a restoring force. The second term describes the damping present in the system parameterized by the Gilbert damping coefficient α.

The addition of a spin torque from a spin current polarized in a direction $\mathbf{P}$ then modifies the LLG equation with the addition of two terms [1] resulting in:

$$\frac{\partial \mathbf{M}}{\partial t} = -\gamma \left[\mathbf{M} \times \mathbf{H}_{\text{eff}}\right] + \frac{\alpha}{M_{\text{s}}}\left[\mathbf{M} \times \frac{\partial \mathbf{M}}{\partial t}\right] - \frac{\gamma a}{M_{\text{s}}}\mathbf{M} \times \left[\mathbf{M} \times \mathbf{P}\right] - \gamma b \mathbf{M} \times \mathbf{P}, \tag{1.2}$$

They are often referred to as damping-like and field-like torques since their form makes them act as modifications to the original two terms of the LLG. The damping-like term strength is controlled by the parameter a where the damping like term b, which describe the magnitude of spin current available. The more important term for this discussion is the damping-like term, which depending on the sign of the spin polarized current can be used to either enhance or negate the internal damping of a ferromagnet[9–11]. This torque is the main contributor

to controlling magnetization in the new generation of electronic spin based electronics.

The ability to tune the damping of a ferromagnetic material leads way to the creation of nanodevices called spin torque oscillators (STO). Going back to the mass on a spring analogy, if the damping of such a system is zero any oscillation will continue on forever. Moreover, if the mass where at equilibrium, changing the sign of damping will actually drive the system into oscillation. A STO is essentially a realization of this concept. When a large enough spin current is injected into a ferromagnet, its damping is reduced to zero resulting in a precession of the magnetization [9, 12–16]. The natural frequency of these devices is typically on the order of a few GHz, which is a typical frequency range used in modern communications.

Application wise, STO have a potential use in hard drive write heads through the concept of microwave assisted magnetic recording (MAMR). In MAMR a rf magnetic field can be used to assist in switching of a nanoparticle [17, 18]. When the magnetization precesses in an STO, so does the magnetic field around the device. Recently Western Digital has announced plans to incorporate STO into their hard drives, claiming that this will allow for potentially higher density of bits to be achieved.

Aside from an oscillating magnetic field, the electrical resistance of a STO oscillates as well. This arises from another property associated with magnetic materials and multilayer stacks, where their resistance changes depending on the relative direction of electrical flow and the magnetization. In the ferromagnet itself, anisotropic magnetoresistance [19] can lead to resistance changes. Bilayers of ferromagnets and materials with high spin orbit coupling can give rise to other effects such as spin Hall magnetoresistance [20] and unidirectional spin Hall magnetoresistance [21]. Structures containing two ferromagnetic layers separated by a spacer can give rise to even larger resistance changes through giant magnetoresistance [22, 23] or tunneling magnetoresistance [24, 25]. These resistance changes are then converted into a microwave voltage by the applied DC current used to create spin current. This results in a compact source of microwave power.

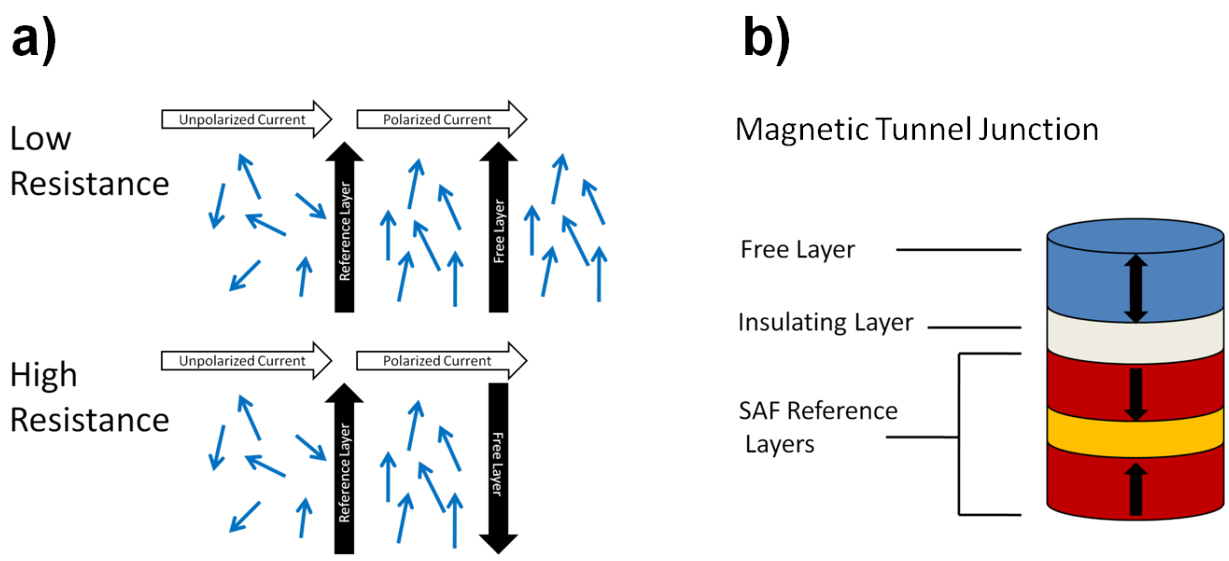

Figure 1.3: **a)** Toy model for the resistance change in two states of an MTJ. **b)** Simplified schematic for a magnetic tunnel junction.

For the generation of a spin current, there are different methods that will be discussed here. The first is similar to the toy model presented earlier and deals with passing a current through a ferromagnet and into another. In this case, the internal field of the reference layer polarizes an incoming charge current and then is injected into a free layer. This method is used in many spintronic applications [3, 5, 9, 26] and so far is the most popular method for use in potential market products. For memory applications, the readout on a device like this can be understood again with a toy model. Figure 1.3a shows the modifications to the spin torque toy model, where the polarized electrons leaving the reference layer are passed through to the free layer. When these electrons enter the free layer there needs to be an empty state in the valence band for them to occupy. In a ferromagnet, the density of states for spin up and spin down electrons is different resulting in different transmission through the second layer. When the two layers are aligned, electrons are able to pass through whereas if anti-aligned, they are blocked. In reality, in the anti-aligned state there is still transmission, but the difference in resistance for the two states can reach over 100%.

One realization of this toy model is known as the magnetic tunnel junction (MTJ). A

schematic of the basic parts of this device are shown in Figure 1.3b for a out of plane magnetized device. The free layer is the layer that is switched during the operation of the device and referenced to a fixed layer across a thin insulating layer. Usually CoFeB is used for the magnetic layers with MgO for the insulating layer [27]since these two materials band structures work well together. The magnetoresistance of this structure depends on establishing a tunneling current through the insulating layer. The tunneling probability is highly dependent on the relative orientation of the magnetic layers giving for a high change in resistance of the device and forms the basis for tunneling magnetoresistance (TMR).

Recently, interest has turned towards exploring other methods of generating spin current. One potential source is known as the spin Hall effect, which was first observed in semiconductors [28]. However, in the early materials it was observed in the effect was too small to be useful. It was not until the observation of the giant spin Hall effect [6] in the metallic material Tantalum did this become a promising alternative. The spin Hall effect in these materials relies on the spin-orbit interaction present in heavy atoms, but conceptually spin Hall materials mimic the classic quantum mechanics problem of the Stern-Gerlach experiment. In a different rest frame, the orbitals of materials with a strong spin Hall effect resemble a magnetic field gradient. When a spin passes through this gradient, it is deflected in a direction that depends on the direction its spin had been pointing. If a ferromagnet is placed such that these currents are deflected into them, the result is a transfer of spin current into the ferromagnet. Figure 1.4 shows the resulting spin current generated from a spin Hall material such as Platinum being injected into a ferromagnet.

In this study, the ferromagnet used was not always metallic. The insulating ferromagnet Yttrium Iron garnet (YIG) has gained popularity due to it having low magnetic damping. This allows for long distance propagation of spin waves and for studying the effect of spin currents that are not accompanied by a charge current. It has been shown in these materials that despite their lack of conductivity, they can still be manipulated by spin currents gener-

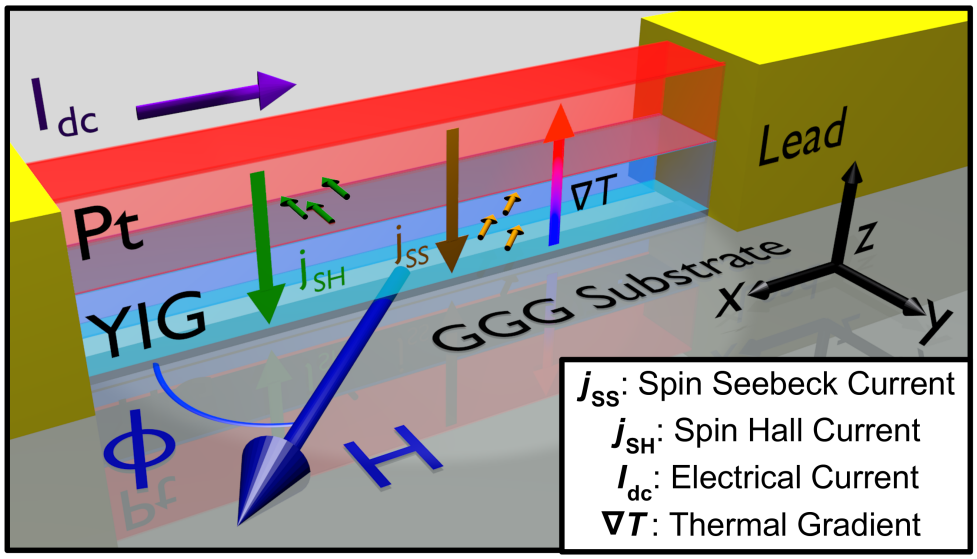

Figure 1.4: Model of a Pt/YIG nanowire based spin torque oscillator.

ated by the spin Hall effect [15, 16, 29]. Further, another potential source of spin current was found in these materials that becomes more apparent due to their insulating nature. Not only are they poor electrical conductors, they are poor thermal conductors as well allowing for the generation of large thermal gradients. If a structure similar to that of Figure 1.4 is made and a thermal gradient is produced as shown, a spin current flows perpendicular to the sample plane through what is known as the spin Seebeck effect [30]. This spin current is theorized to be carried by quasi-particles of magnetic vibrations, known as magnons[31–33]. The interaction of the magnonic spin current and the adjacent normal material results in the flow of a net spin current that depends on the direction the thermal gradient. The magnetic damping of YIG was theorized [34] to be controlled through this effect and has been shown in ferromagnetic resonance studies on films [35, 36]. Further, in nano-structures where large thermal gradients from Ohmic heating can be easily produced, the spin Seebeck effect has been able to drive STO [16, 37]

Aside from thermal means, in this manuscript a new source of spin torque that requires only a single ferromagnet (FM) and an adjacent nonmagnetic material (NM)is presented. The origin of the torque lies in the spin-orbit coupling, specifically $s-d$ scattering, in metallic

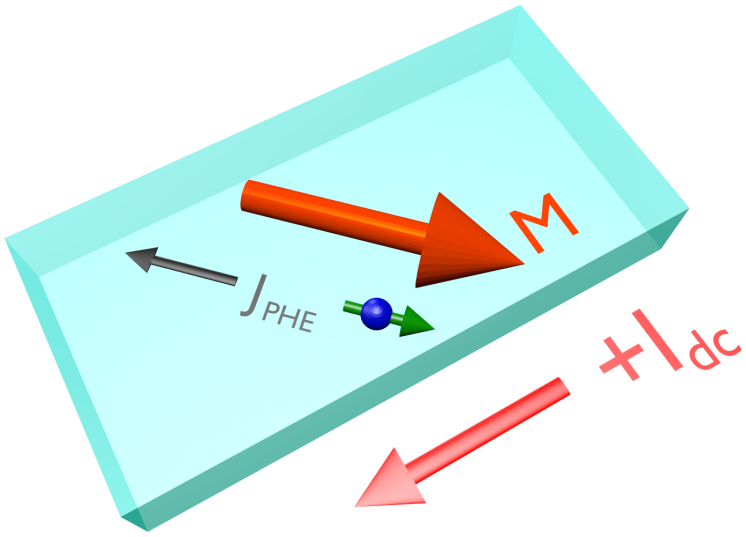

Figure 1.5: Schematic representing the spin polarized current produced by the planar Hall effect.

ferromagnets. This same $s-d$ scattering mechanism leads to the well known anisotropic magnetoresistance (AMR), where the resistivity of the ferromagnet differs whether the magnetization is parallel ($\rho_{\parallel}$) or perpendicular ($\rho_{\perp}$) to the electric-field E used to drive an electric current [19, 38]. In the case of intermediate angles between the magnetization and electric-field, $s-d$ scattering leads to additional electron flow along the axis of the magnetization in the direction $(\mathbf{m}\cdot\mathbf{E})\,\mathbf{m}$ [39] giving rise to the Planar Hall effect schematically represented in Fig. 1.5. In the case of Ni and Co, theoretical studies[40] have shown that the spin of the conduction electrons contributing dominantly to the AMR transport have their magnetic moment aligned to the magnetization direction $\mathbf{m}$. Therefore, AMR leads to the additional electron and spin currents (expressed here as magnetic moment) in the FM [39],

$$\mathbf{J}_{\mathrm{PHE}} = \frac{\Delta\rho_{\mathrm{AMR}}}{\rho_{\parallel}^{2}}\,(\mathbf{m}\cdot\mathbf{E})\,\mathbf{m} \tag{1.3}$$

$$\mathbf{Q}^{\mathrm{z}}_{\mathrm{PHE}} = \frac{g\mu_{\mathrm{B}}}{2e}\eta\mathbf{m}\otimes\mathbf{J}_{\mathrm{PHE}}, \tag{1.4}$$

respectively. Here $\Delta\rho_{\mathrm{AMR}} = \rho_{\parallel} - \rho_{\perp}$, the first term in 1.4 converts from charge to magnetic moment flow, g is the Landé g-factor, μ_{B} is the Bohr magneton, and η accounts for polarization efficiency. When this current is injected into an adjacent NM layer, it looses its polarization resulting in a net momentum transfer, and an exertion of a torque on the magnetization and is the origin of the Planar Hall torque (PHT). While torques from the planar Hall effect have been proposed in systems of two ferromagnets[39], this work shows that torques can be induced with only a single FM layer.

Chapter 2

Methods

2.1 Spin Torque Ferromagnetic Resonance (ST-FMR)

2.1.1 Basics

In a typical spin torque ferromagnetic resonance experiment, microwave current is directly applied to a sample [11, 41, 42] to excite magnetic oscillations. In the case of the nanowires measured here, the microwave current exerts an ac spin torque and Oersted field drive on the adjacent ferromagnetic layer. Typically, anywhere from -20 dBm to 0 dBm of microwave power is sourced from the generator. A DC signal is then produced from the rectification of the microwave drive and the resistance oscillations during resonance. In metallic based nanowires, anisotropic magnetoresistance provides a mechanism for detection. However, in the case of a YIG/Pt wire where the ferromagnet is insulating, the resistance oscillations come from a combination of the spin Hall magnetoresistance and inverse spin Hall effect [43].

The general schematic for the equipment and connections needed to perform this type of measurement are shown in Fig. 2.1a. A microwave generator is connected to the nanowire

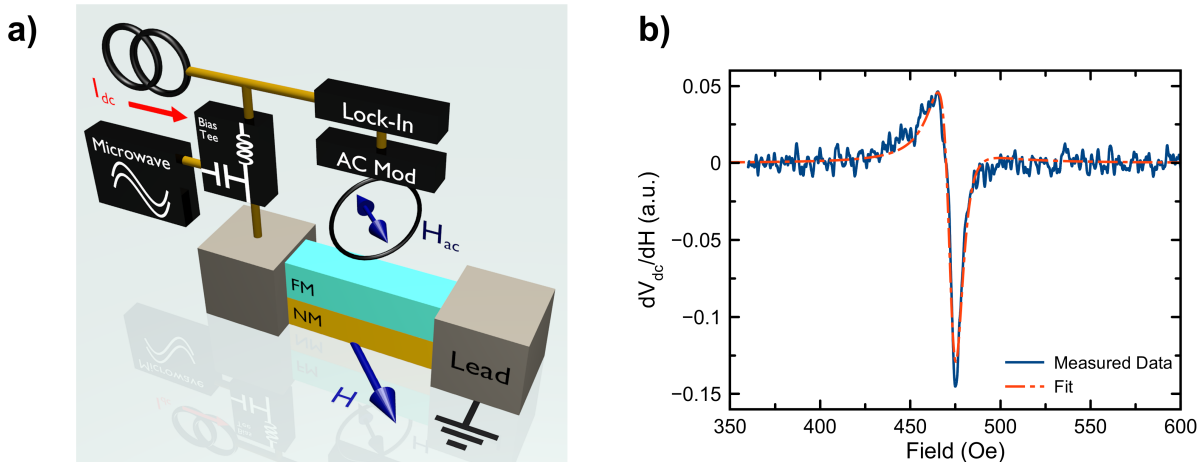

Figure 2.1: **a)** Block diagram for measuring ST-FMR **b)** Example of a measured ST-FMR trace.

through a bias tee which serves to isolate the DC and microwave electronics. The application of DC to the microwave ports on many types of equipment will cause damage so this is critical. On the DC port of the bias tee, the rectified voltage is measured and an additional DC current can be added to study the effect of static spin current.

Since the signal voltage is small relative to the typical noise in this type of circuit, a field modulation technique and lock-in detection is employed [44] where an AC magnetic field (317 Hz) is used to modulate the resonance. The modulated voltage is then detected using a lock-in amplifier to measure voltage. This method is highly sensitive to low level magnetic signals since the modulation scheme only affects voltages that can respond to magnetic fields near where the modulation field is applied. This differs from the commonly used amplitude modulation technique where the signal produced can still have large background voltages due resonances in the entire circuit.

An example trace is shown in Fig. 2.1b. The typical resonance peak in ferromagnetic resonance is a sum of a Lorentzian and anti–Lorentzian functions when the magnetic field H is swept and microwave drive frequency held constant. However, with the addition of field

modulation, the measured signal is the field derivative:

$$\frac{dV_{mix}(H)}{dH} \propto \frac{2A}{\Delta H\left(1+\frac{4(H-H_r)^2}{\Delta H^2}\right)} - \frac{16A(H-H_r)^2}{\Delta H^3\left(1+\frac{4(H-H_r)^2}{\Delta H^2}\right)^2} - \frac{8S(H-H_r)}{\Delta H^2\left(1+\frac{4(H-H_r)^2}{\Delta H^2}\right)^2} \quad (2.1)$$

Where H_r is the resonance field, ΔH the linewidth expressed as full width half maximum, A the amplitude of the anti–symmetric component and S the symmetric.

2.1.2 Lock–In Setup

Proper setup of the lock–in used in the measurement is critical for getting a good signal. The specifics here are mostly related to the Signal Recovery branded units, but many of the settings carry over to other lock–ins. One specific setting to these lock–ins is the type of detector (bipolar or FET) that can be used. For most ST-FMR measurements, the FET detector is used. The bipolar detector is meant for low impedance samples and does not like the presence of DC voltages. Since most ST-FMR measurements performed here study the effect of DC bias, this detector can not be used. However, for field dispersion measurements on samples with resistances of a few hundred ohms the bipolar detector gives much lower noise. So sometimes it is useful to change between the detectors depending on the type of measurement done.

The input signal to the lock–in can be set up as a single input measurement (A) or look at the differential voltage between two inputs (A-B). Which setting works better seems to be very sample dependent. Single input seems to work better for most samples in ST-FMR measurements. However, in measurements where transverse voltage is measured A–B gives a much better signal. Either way, the best thing to do is test back to back these two configurations and see which gives lower noise.

The time constant also is an important setting. In the more modern lock–ins this can be

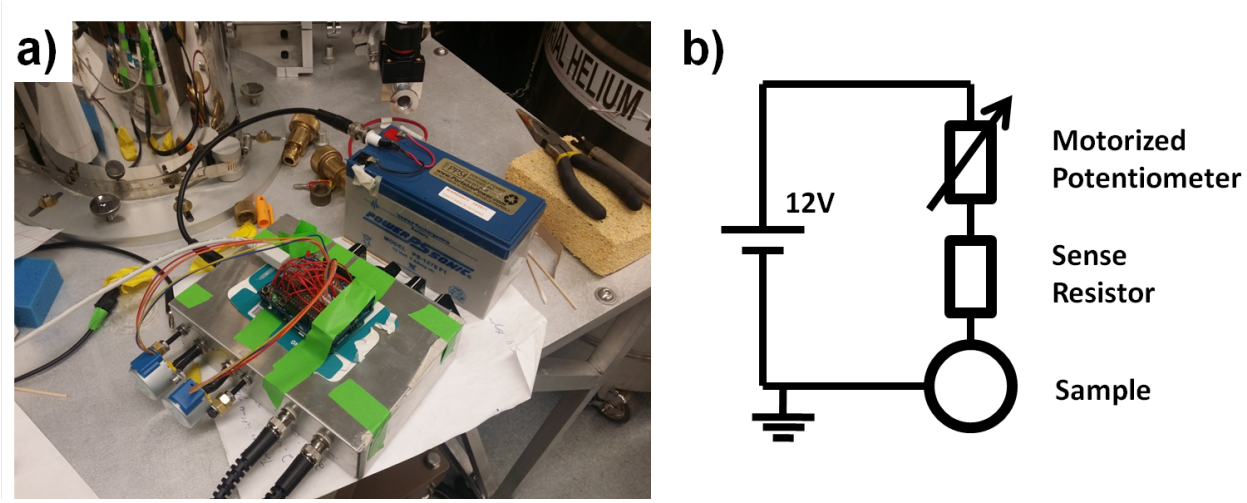

Figure 2.2: **a)** Battery based DC current source **b)** Equivalent circuit diagram for the DC current source.

thought of as more of an integration time describing how long the lock–in averages for. In the later DAQ section the importance of setting this value correctly will be explained. In general though, this setting is set between 10 ms and 100 ms.

2.1.3 Current Source for ST-FMR

The lock–in amplifier is very sensitive to the noise of any attached current source. To improve signal quality it is very important that the DC current source be as clean as possible. Current sources such as Keithley 2400s and Yokogawa GS200s claim to be low noise, but for the low level signals that are measured in some of the devices these sources are not sufficient. Typically there are different current ranges on these sources and the noise observed is directly related to the range used. For the lowest range (1 mA), the noise is the least and it is possible to obtain a decent signal, however, does not provide enough current for this study. Ideally, this noise can be eliminated by decoupling the digital electronics from the DC side.

A decent solution for decoupling the digital electronics and making a low noise current source is surprisingly the simplest imaginable way of varying the current thorough a resistor,

a voltage divider. A 12V battery provides for a very stable low noise voltage source. By placing a variable resistor in series with the measured sample the DC current can then be varied. The samples used in this study have small percentage changes in resistance, so the current provided by this divider is relatively constant. The biggest drawback to this method is if the study being performed is a DC bias study, the grad student performing the measurement gets very tired of turning a knob every few minutes very quickly. The solution to this was to use an arduino and stepper motor to allow computer operation. The use of a mechanical control decouples the digital electronics from the DC line preserving the low noise qualities of a battery source. The motor is secured to the knob with tape in a way that allows some give in case the motor vibrates slightly when powered.

Figure 2.2 shows the actual current source and a schematic of the DC circuit used. Feedback for the current value of DC current is achieved by placing a sense resistor in series with the sample and monitoring the voltage across it with a Keithley 2182A low noise voltmeter. Sadly, the inclusion of a voltmeter increases the noise level slightly, but the remote control makes up for it. Running the current through an ammeter was tried as well, but the ammeter introduced far more noise than the voltmeter.

The control software for this source can be found on the main group storage computer in the folder called "Battery Source Software." The control scheme is fairly crude and contains no safeties against applying too much current to a nanodevice. The program entitled "arduinofirmware.ino" needs to be loaded into the arduino memory. This program configures the arduino such that if any numerical string is sent to it through the serial connection, it rotates the stepper motor by that many steps.

On the python side, the program "BattI.py" can be used with the version of the lab standard python library that was common at the time. This software uses a crude proportional–like method to adjust the current. One difficulty with control of the current is that the variable resistor is non-linear, in that as you go to higher currents the knob needs to be turned less

and less to keep the current step size the same. The program has an attempt to try and deal with this, however for currents higher than 3 mA control becomes difficult. For setting the current, the program allows for some mismatch between the set-point current and the set current to decrease the amount of time that the program spends hunting for a current. Also the program returns the actual value of the current so it can be used in calculations.

When using the source it is best to test it on a resistor box first with a sample roughly the same resistance since there are no safeties in the software. Usually, I check that all the currents I need for a sample can be easily accessed with minimal overshoot before an important sample is connected.

2.2 Emission Measurements

2.2.1 Standard Method

Spectrum analyzers are a powerful tool for measuring microwave power at multiple frequencies since conceptually, they act like performing a fast Fourier transform on any incoming signal. This function makes one invaluable for the measurement of microwave emission from a spin torque oscillator. Traditionally for this measurement, the equipment is configured in a manner similar to Figure 2.3. The sample is supplied DC current through the DC port of a bias tee and the emission is then detected on the RF port of the bias tee. Usually a low noise microwave amplifier is placed before the spectrum analyzer to increase the signal quality. There are two models of spectrum analyzers available for use in the lab; Agilent E4405 and E4408B. Both models are suitable for many measurements. The E4405 is preferable since it can store a larger amount of data points in its memory. The E4408B can only store 400 data points and requires the user to "window" the measurement range into 400 point bits. This slows down measurements compared to the E4405. For many types of samples, the direct

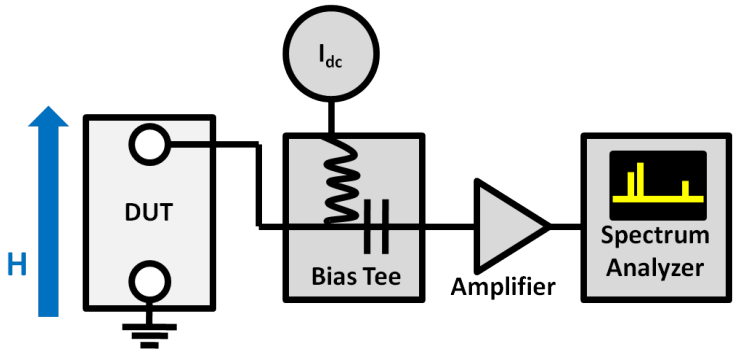

Figure 2.3: Block diagram for a direct measurement of microwave emission from a spin torque oscillator.

method has been successful since their output power is well within the detectable range of a typical analyzer-amplifier combo.

There are a few settings that need to be set for a typical measurement:

- Scale: Linear
- Reference Level: At least twice the value of the largest amplitude peak
- Y–Axis Units: Watts
- Resolution Bandwidth: 3 MHz for broad peaks and less for narrow ones

The typical nanowire based spin torque oscillators studied here have a resistance on the order of a few hundred ohms. However, the microwave equipment used is designed to work with 50 Ohm impedance and the resulting mismatch between the STO and equipment leads to standing waves in the circuit. To try and minimize their presence in spectra, a trace is taken at zero bias and then is subtracted from the traces measured at bias. This eliminates some of the background, but the effects of standing waves still show up as seen by the horizontal lines in Fig. 2.4a. One way to decrease them is to increase the length of cables in the circuit. This not only adds attenuation to the circuit and thus decreases the amplitude of the standing waves, it changes their periodicity since the wavelength is now different. Figure 2.4b shows

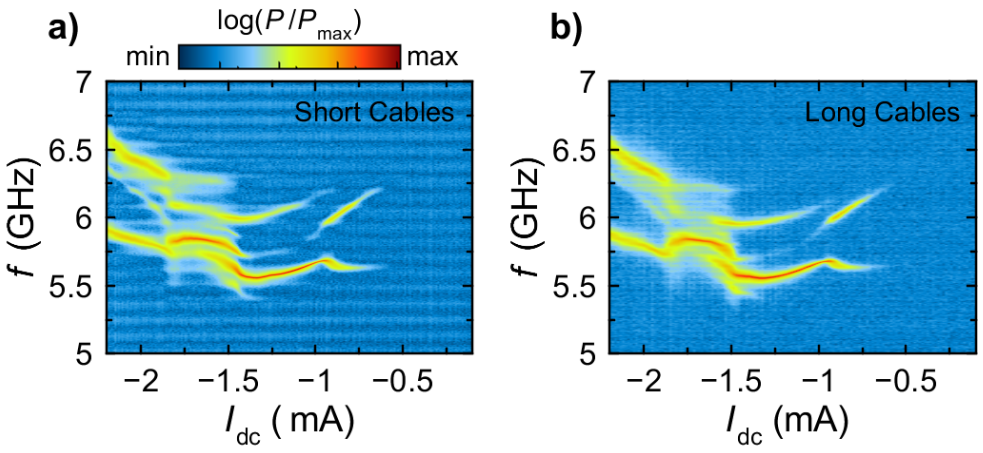

Figure 2.4: Color plots of emission measured from a spin torque oscillator with **a)** short cables and **b)** long cables.

the same STO measured with a few feet of additional cable added in. In this color plot the visual presence of standing waves is much less compared to the measurement done with shorter cables.

The power output of the STO being measured will determine the length of cable that can be used. In Fig. 2.4 the STO measured is based on Ni/Co multilayers and can output up to 100 pW of power. This is easily measured with a good amplifier and longer cables. However, in the case of STO based on YIG, the power output is much less available power with only 6 fW present. In is case, the cables need to be as short as physically possible since the attenuation of the cables can quickly bury signals into the background noise.

2.2.2 Field Modulated Method

In principle, one would think that increasing the amount of points averaged would allow for a low level signal to be measured. This comes with a cost in time that not only makes the measurement time prohibitive, but can make the measurement inaccurate. Typically in the cryostat there is a slight temperature drift over long periods of time which will shift the center

frequency of the emitted power slightly over time. If the measurement period is long, the measured peak will then be artificially broadened. To improve the measurement quality and speed, moving to a modulated technique is desirable since the lock-in measurement technique is powerful for picking out low level signals in a noisy environment. This is implemented in a manner similar to the previous section with the introduction of field modulation.

The field modulated spectrum analyzer method is as follows in the block diagram in Figure 2.5a. Like the direct method, DC current is supplied to the sample through a bias tee. The main difference is the configuration of the spectrum analyzer. Normally measurements are made in the frequency domain on a spectrum analyzer, but there is a mode called "zero span" where the detection frequency can be fixed and then the power over time is displayed. In this mode the analyzer essentially acts as a band-pass filter for a selected frequency and allows for the field modulation technique to be employed. If an emission peak is at the edge of the detected frequency, the field modulation will shift the resonance frequency such that it moves in and out of the band-pass filter, creating an AC signal. This AC signal can be passed to a lock–in amplifier through the video output on the analyzer. Some model analyzers do not have a video output but instead have an audio output in the front that can be enabled. The signal can be taken from there as well and gives about the same quality data as the video out.

There are a couple subtleties to the setup of the spectrum analyzer. One is the resolution bandwidth, which determines the width of the band-pass filter when the spectrum analyzer is operated in zero span mode. A 5 MHz resolution bandwidth works well. The power scale needs to be sent to linear and the reference level power set such that variations in power over time are visible on the main screen. The video output on the spectrum analyzer outputs a voltage proportional to the deflection of the signal on the screen, so if you can not see any variation the lock–in is not likely to either. Lastly there is one more setting that needs to be made or else the measurements will be very noisy. Under the system menu there is an

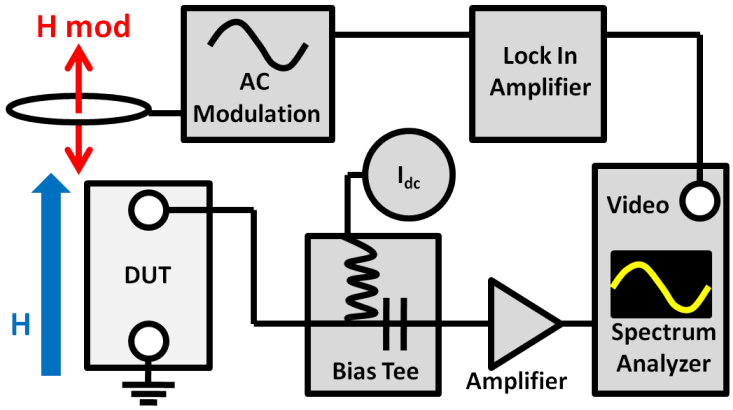

Figure 2.5: Block diagram for the field modulated spectrum analyzer measurement technique.

option called auto-alignments. These alignments need to be turned off or time to time the spectrum analyzer will pause measurement. The lock–in determines these as spikes and will give a bad signal.

In summary the following settings need to be made on the spectrum analyzer:

- Scale: Linear
- Reference Level: A value where you see variations in the signal
- Y–Axis Units: Watts
- Resolution Bandwidth: 5 MHz
- Auto Alignments: off

Since the power emitted from a YIG based oscillators is small [15, 16] due to having a small MR ratio, it is best to first benchmark this new technique using a different type of sample. A magnetic tunnel junction is a good system to test this method since it has high magnetoresistance. The field dispersion and its bias dependence is easily measurable with the ST-FMR method described earlier, allowing for quick determination of the conditions needed to reach a self oscillatory state. Further, the self oscillatory state does not need to

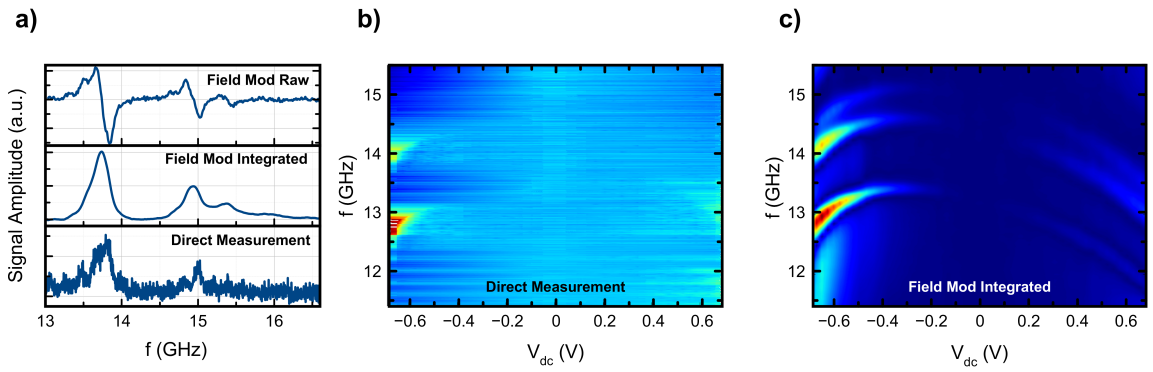

Figure 2.6: **a)** Comparison of single traces for the direct spectrum analyzer method and field modulated method. **b)** Color plot of the emission power as a function of bias voltage using the direct method and **c)** using field modulation.

be reached to observe microwave power from this type of device. The high MR allows for easier observation of thermal FMR, where even small thermal fluctuations in magnetization will give way to a measurable microwave power.

The signal produced by field modulation technique can be seen in Figure 2.6a along with the direct method. In general, the emission peaks should be Lorentzian shaped in the normal measurement method. Like the field modulated ST-FMR described earlier, the signal measured with modulation is the field derivative $(dP\,(H)\,/dH)$ of the emission signal. Since the lock–in integration time is a form of averaging, to compare the effectiveness of field modulation the traces are acquired such that they have the same data density and require the same time to complete. Clearly the signal to noise ratio for the field modulated trace is improved over the direct measurement.

To further illustrate the improvement made by this new technique, color plots for the detected microwave as a function of bias and frequency are made and are shown in Figure 2.6bc. As with the single traces, the averaging on the plots is such that they require the same amount of time to generate. Again a large increase in signal to noise is seen with the addition of field modulation. In both approaches the lowest frequency mode is seen at high bias, but field modulation allows for it to be observed at much lower biases. On top of this field

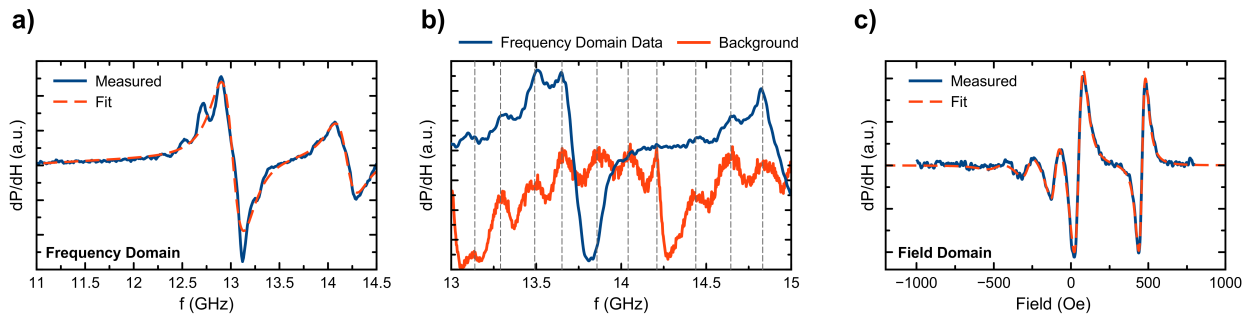

Figure 2.7: **a** Single field modulated spectrum analyzer with Lorentzian derivative fit. **b** Demonstration on the standing wave background's effect on the trace taken in the frequency domain. **c** Single trace taken in the field domain showing the suppression of artifacts from the standing wave background

modulation reveals another high frequency mode that is not visible in the plot generated with conventional means.

With the field modulation technique there is the choice of measuring in either the field or frequency domains. In typical emission experiments the frequency domain has been chosen since the spectrum analyzer trace acquisition is meant to work this way when used in the spectrum analyzer mode. However, in the frequency domain there exist oscillations in the background due to the presence of standing waves. When measuring in the frequency domain these still impact the measurement as seen in the oscillations from the fit in Figure 2.7a. These oscillations are directly related to the background as shown in Figure 2.7b where the direct measurement of the background is compared to a trace. The dotted lines indicate maxima for the background and they appear in the field modulated trace as well.

In principle the field modulation technique should ignore any background which makes the observation of these oscillations surprising. Their presence may be directly related to the physics of microwave circuits rather than just poor background subtraction. It has been recently shown that a spin torque oscillator's performance can be altered by locking to itself. [45] This was accomplished by placing a delay line before the spectrum analyzer to change the phase of the power that gets reflected back to the spin torque oscillator. Since the

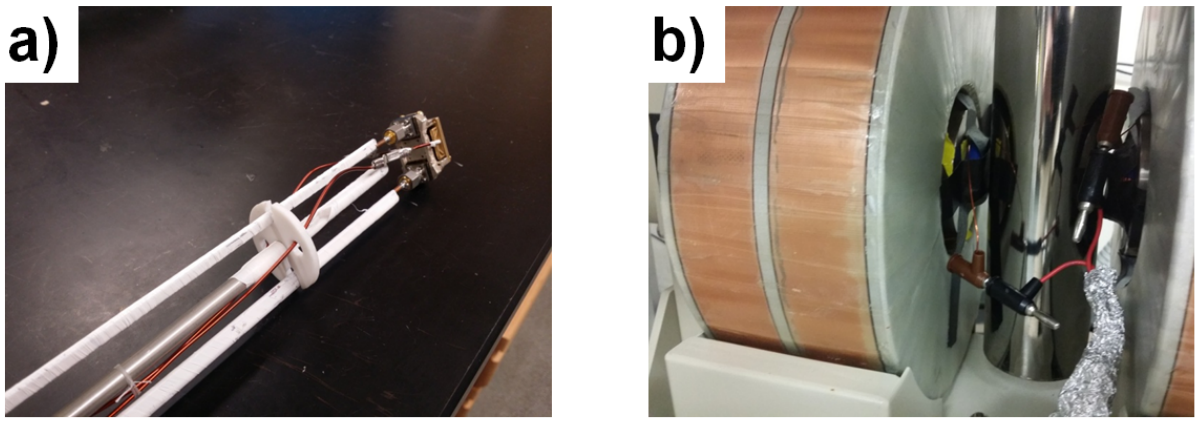

Figure 2.8: **a)** Early prototype sample holder with single wire used for modulation **b)** External modulation coils placed outside of the cryostat

standing waves in the circuit are due to similar interference of reflected waves, it is possible that in the frequency domain these oscillations are inevitable without controlling the phase of reflected power.

A simple approach to decrease the contribution from the standing waves is to perform the measurements in the field domain where the frequency is held constant. The reflected power will still alter the spin torque oscillator measurements, but it will be a constant offset throughout the measurement, rather than an oscillating perturbation. Figure 2.7c shows a trace taken in this domain and compared to the frequency domain, we see an almost perfect fit to the theoretical model for an emission peak.

2.3 Field Modulation Coils

The measurement techniques presented in this chapter rely on the ability to generate a AC magnetic field in order to create a modulation for lock–in detection. There are several experimental details that help improve signal quality. In general, any little bit of improvement that can be made to the setup is worthwhile since it decreases the amount of averaging

needed, and consequently the total measurement time needed. The design and implementation of the field modulation can change the quality of the signal. Even ignoring the design, not all modulation frequencies give the same noise level. It is usually best to optimize the modulation frequency by sweeping it and measuring the noise present. Further, the design of the modulation helps with signal quality.

Adding field modulation to the cryostat is not a completely simple task. The geometry of the cryostat restricts the possible designs and if the coils are placed outside the cryostat, the cryostat's metal attenuates the modulation. Early designs for the setup used a single wire placed in the cap above the sample holder as seen in Figure 2.8a. For a long time in the lab's probe stations, the use of a single wire with a high current of roughly 4 amps had been a proven successful method. However, implementing this into the cryostat did not share the same success. Mainly this is because once installed, the direction of the wire could not be changed. This is problematic since in order for field modulation to work properly, the modulated field direction needs to match the applied field. Secondly, running 4 amps of current through the cryostat seemed to increase the helium consumption and occasionally the wire would short on the sample holder cap resulting in death of the sample.

The best solution was mounting external coils outside the cryostat like in Figure 2.8. Surprisingly, a small modulation frequency of 267 Hz still works even though one would expect the amount of metal in between to block some of the AC modulation. The signal quality from such a coil was found to be similar the wire when the wire's modulation field was aligned with the static applied field. However the modulation from a single wire decreases as the field is rotated where the coils do not. One issue with the external coils is they will tend to vibrate in a strong magnetic field. Aside from producing a loud audible noise, a vibrating coil will cause the AC modulation to have a distorted waveform introducing electrical noise. Since the vibrations depend on the strength of the static applied field, it introduces an additional field dependent background that is often not a simple function.

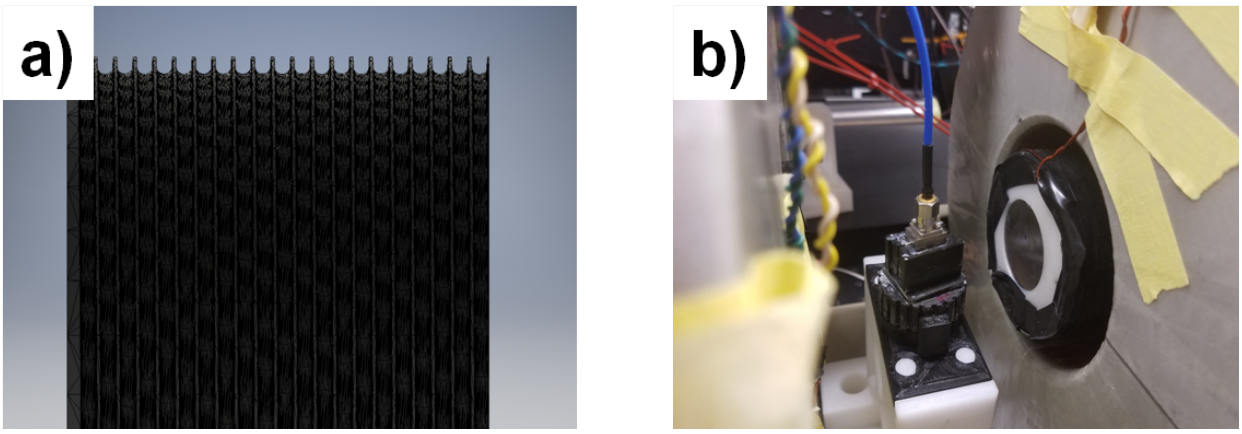

Figure 2.9: **a)** Side view of a 3D printed modulation coil. **b)** Assembled exterior modulation

The early coils were made from wire wrapped around round plastic sample holders. These were taped to the pole pieces and often required cardboard to be jammed between them and the cryostat to keep them from vibrating. While this worked, it was far from ideal. A better approach was made using a 3D printer to design a sleeve that fits over the magnet pole piece. This sleeve had indents patterned into it to hold the modulation wire as shown in Fig. 2.9a. After wrapping wire into this sleeve, electrical tape is tightly wound around it and then it is inserted onto the magnet pole piece. Figure 2.9b shows a completed coil.

2.4 DAQ Based Measurements

In both the ST-FMR and field modulated spectrum analyzer measurements discussed here, the ultimate data collection is performed by a lock–in amplifier and then sent to a computer to be stored. A simple approach to do this is to use GPIB communication between the lock–in and computer. This requires a large amount of queries to the lock–in. Further, in the case of a field sweep one must wait for the field to settle before performing the measurement. If the ferromagnetic material being measured has a narrow linewidth, this requires a finer amount of data points to be collected and increases measurement time.

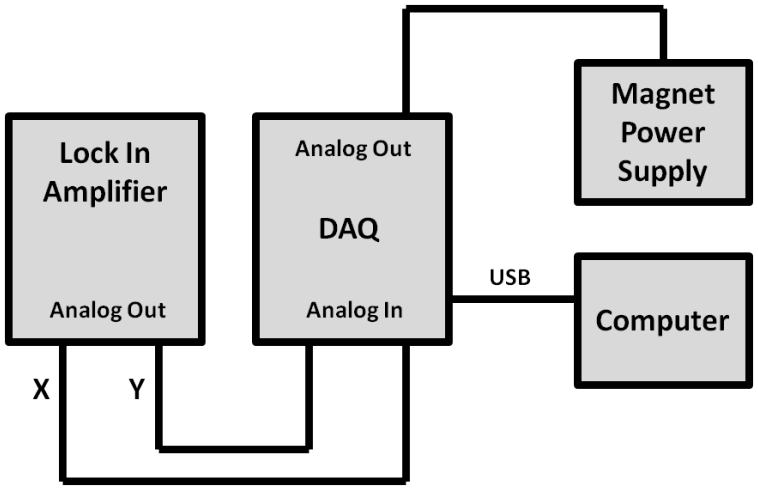

Figure 2.10: Block diagram for the addition of a DAQ to the measurement setup.

The addition of a National Instruments simultaneous DAQ to the measurement station allows one to perform field domain measurements much quicker. A simultaneous DAQ is able to perform a constant sweep of output ports while simultaneously monitoring multiple inputs. In order to use this with the lock–in, there needs to be an analog output on the lock–in as shown in Figure 2.10. Typically these outputs give a voltage ranging from -10 V to 10 V that scales to the voltage the lock–in is measuring.

The main advantage of the DAQ is that it allows for a continuous sweep of the magnetic field. Inevitably, in the connections to the sample that is being measured there is a loop of wiring. When the field is changed, a voltage is produced in the wiring due to Lenz's law. With a continuous sweep, the change in flux over time through the loop is a constant which does not affect the lock–in. In the method where the field is controlled by the lock–in and discrete field steps are taken, the change in flux looks more like a series of pulses which can have components over many frequencies and can sometimes upset the lock–in. Also a continuous sweep allows for a high density of data points in field space to be easily collected. Multiple things can be monitored at the same time like sample resistance and Hall probe voltage with no additional cost of measurement time.

When using a continuous sweep, the sweep rate is an important parameter since the field

can only be swept so fast. The magnet itself an inductive load on the magnet power supply and if the magnetic field is swept quickly the measured field will not keep up with the sweep. Further, the lock–in time constant determines the fastest sweep rate possible. If the sweep rate is faster than the lock–in time constant, the measured peaks will become broadened. Generally the best approach to determining the sweep rate is the experimental one. First, pick the lowest time constant that you can get away with. Next, take a few traces at increasing speed until the trace begins to broaden. Then take that sweep rate and use something a little bit slower.

Another issue with this method is unique to the Signal Recovery series of lock–ins. At some sensitivity settings, there is a low frequency periodic spike on the analog outputs. I still do not know the exact origin of this. The best way to deal with it is to use a filter to block it. A low noise preamplifier with filter works well for this, but a simple RC circuit may be able to take it's place. On the other hand, the Stanford Research lock–in does not have this issue and is probably better suited to this type of measurement.

2.5 Micromagnetics

Micromagnetic simulations are a powerful tool for modeling the magnetic material behavior. Since modeling each atom in a crystal structure is not easily possible, these simulations divide a region into cells and treat each cell as a macrospin coupled to its six nearest neighbors. This division is fairly valid since in a magnetic material variations in the magnetic state occur over an exchange length l_{ex} determined by the materials exchange stiffness and magnetization. Typically this is on the order of a few nanometers.

There are two programs called OOMMF[46] and MumMax3[47] that have been used throughout these studies. Both are similar in the operations they do, but have some major differ-

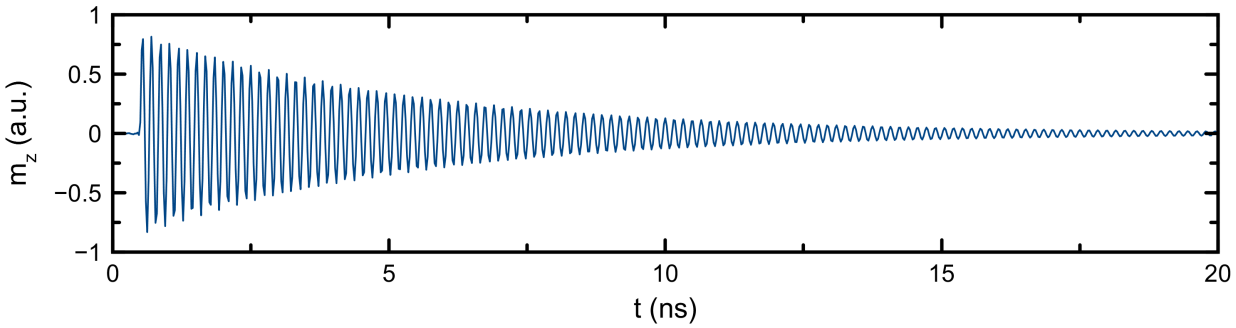

Figure 2.11: Ring-down of magnetization after sinc pulse excitation.

ences. The main difference is the way the data is processed. OOMMF uses the CPU on the computer to make calculations which limits the amount of parallel calculations that can be done. On the other hand, MuMax3 uses GPU processing to take advantage of the parallel processing power of graphics cards. Generally, for small systems OOMMF works better and for larger MuMax3 is better.

2.5.1 Eigenmodes

In the studies presented here, micromagnetics are mainly used to determine the nature of magnetic oscillations and their resonance frequencies. In a nanoscale magnetic element, the edges confine any oscillations. This acts much like the particle in a box quantum mechanics problem, where confinement leads to standing waves that depend on the size of the box.

These standing spin wave modes have discrete frequencies at a given applied field. To determine them, a ring down method is used [48]. This method can be used in either program. In it, the modeled geometry is first allowed to relax to a ground state with any static applied magnetic field. Once relaxed, the system is then excited with a sinc pulse magnetic field. The average magnetization is then recorded in time as the system relaxes from this pulse. The relaxation is shown in Fig. **??** where the magnetization oscillates back and forth as it approaches its ground state. The oscillation of magnetization is governed

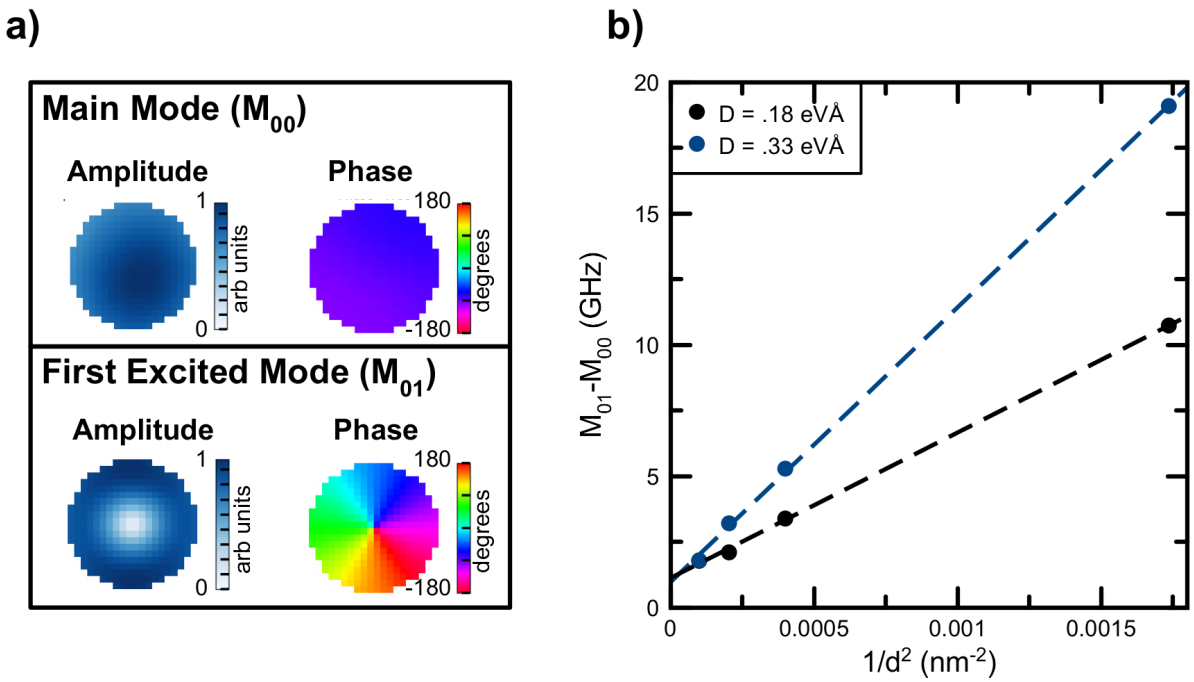

Figure 2.12: **a)**Spatial profiles of an MTJ free layer for the two lowest order modes. **b)** Separation of resonance frequency for the two lowest order modes as a function of inverse diameter squared.

by the system Eigenmodes. Performing a FFT on this data produces the Eigen-frequencies that the various standing spin wave modes that are present.

Unlike electrical experiments, the spatial profile of magnetization dynamics can be easily determined. It just requires recording the magnetic state of the entire modeled geometry over time and performing a fft on each cell. Then knowing the frequency of interest the amplitude of oscillations on that frequency can be mapped.

Figure 2.12a shows an example of this for the free layer of a magnetic tunnel junction free layer discussed in more detail in Reference [49]. Since the free layer is circular, analytically the spatial solution is possible and states that the frequency separation between the two lowest modes should be proportional to the inverse diameter squared of the circle. Figure 2.12b shows that the micromagnetics reproduce this analytical solution.

2.5.2 Granular Studies

Realistic materials are not a single perfect crystal like the square lattice of cells in the micromagnetic simulations. In a later chapter, the role of granular structure on the magnetization dynamics is investigated both experimentally and with micromagnetics. This requires modeling the granular structure into the simulation. Luckily, this has been implemented into MuMax and the code for this exists[47]. The code defines randomly shaped grains of an average size $grainsize$ as a number of regions up to a maximum region size of 255 regions. To implement this, add the following code after defining cell size and geometry:

$grainSize := 30e-9$

$randomSeed := 1234567$

$maxRegion := 230$

$ext\_makegrains(grainSize, maxRegion, randomSeed)$

The simulated structures where based on measurements of devices made from films with large inhomogeneous broadening to the FMR linewidth. This implies the anisotropy varies across the grains. To simulate this, each region of grains is swept through and the anisotorpy K_{u1} is set to K_max plus a random norm times three percent:

$for\, i := 0; i < maxRegion; i++\{$

$\quad Ku1.SetRegion(i, K\_min*1e{-}3/thickness + randNorm()*0.03*K\_min*1e{-}3/thickness)$

$\}$

The resulting anisotropy distribution is shown in Fig. 2.13, where darker grains represent areas with higher anisotropy.

The exchange coupling between grains is often reduced from the bulk value. This can be

Figure 2.13: Anisotropy distribution when modeling the granular structure.

implemented into the simulation by scaling the exchange between the grain regions as follows:

$$
\begin{aligned}
&for\, i := 0; i < maxRegion; i++\{ \\
&\quad for\, j := i+1; j < maxRegion; j++\{ \\
&\qquad ext\_ScaleExchange(i, j, 0.4) \\
&\quad \} \\
&\}
\end{aligned}
$$

Next the sinc pulse excitation needs to be applied to the active region of the wire defined by the leads of the real device. The easiest way to implement this typically is to define a region the size of the active region and apply the excitation only there. However, for the granular studies this method does not work. When the active region is defined, the MuMax code sets the anisotopy in that region back to a constant value. This negates the whole purpose of defining grains. A work around is to make the excitation field spatially dependent. In the version of MuMax used, this was not as simple as typing $B(x)$ directly. To add spatial dependence, each cell needs to be looped over and using $index2coord$, its coordinates are determined. Then a mask can be built where Heaviside functions select only the active region. Once this mask is made, it can be mapped to the sinc excitation and added to the applied field as shown in the last line of code.

$$
\begin{aligned}
&mask := newVectorMask(Nx, Ny, 1) \\
&for\, i := 0; i < Nx; i++\{ \\
&\quad forj\ := 0; j < Ny; j++\{ \\
&\qquad r\ := index2coord(i, j, 0)
\end{aligned}
$$

$x := r.X()$

$y := r.Y()$

$Bz := Heaviside(x + active\_length/2.0) * (1 - Heaviside(x - active\_length/2.0))$

$mask.setVector(i, j, 0, vector(0, 0, Bz))$

}

}

$B\_ext.add(mask, Amp * sin(omega\_cut * (t - 10 * t_cut))/(omega\_cut * (t - 10 * t_cut)))$

2.6 Cryogenic Measurements

The ability to manipulate bath temperatures provides several advantages over room temperature measurements. First it reduces any noise due to thermal fluctuations making the measurement of low level signals easier. Second, due to the nature of the measured devices and the high current densities needed, their temperature can increase significantly (about 150K) over the bath temperature. For room temperature measurements, this means that the device temperature can start becoming close to the ferromagnet's Curie temperature or can burn out. Even though some materials will have a Curie temperature well above the reachable temperatures at room temperature, being in thin film form reduces the Curie temperature and the nanopatterneing process reduces it as well. Aside from this, the properties of many materials are temperature dependent and being able to manipulate the bath temperature helps in determining if they are the cause of any observed effects.

2.6.1 Continuous Flow Liquid Helium Cryostat

The main component of the measurement station built here was a liquid helium cryostat manufactured by CIA industries with a temperature range of 1.5 K to 300 K. Figure 2.15

shows the engineering drawing for the cryostat with additional valves that were added on. The cryostat has two main chambers, the sample space and helium space. As indicated by their names, the helium space is where the liquid helium is stored and samples reside at the bottom of the sample space. A needle flow valve then allows for the flow of helium to the sample space. Since the cryostat works by allowing liquid helium to evaporate near the sample, a vent valve on the sample space allows for the gas to escape to atmosphere.

The fabrication of the station began with the assembly of the table to hold the cryostat. Making a sturdy table was important so that the station does not move and keeps the cryostat centered in the magnet. The older cryostat in the lab had a table that was bolted together and had a small amount of flex. To improve on this, a table structure was fabricated with welded joints and is shown in Figure 2.14a. The welder used was a Miller 211 MIG welder with a spool gun which does not make pretty welds on aluminum, but are structurally sound.

The next part of the fabrication involved building the support structure for the various valves needed to operate the cryostat seen in Figure 2.14b. These where made from aluminum and made on the mill in the machine shop. The then completed station is pictured in figure 2.14c. These valves are crucial to the operation of the cryostat. They can be used to pump on the sample space by closing the vent valve and opening the other valve on the line. A temperature of 1.6 K is then reachable with the valve to the roughing pump fully open and the needle valve mostly closed. For the project described in this study a temperature this low is not necessary, but for previous work on superconductivity it was important.

The more important use of these valves is during the initial cool down of the cryostat. When the cryostat is not in use it is left exposed to atmosphere, meaning that air and water vapor are inside the system. In this state if liquid helium were to be transferred in, all these gasses would solidify and block the flow of helium. As such the chambers need to be pumped out. The general procedure is to use these valves to pump each chamber individually for

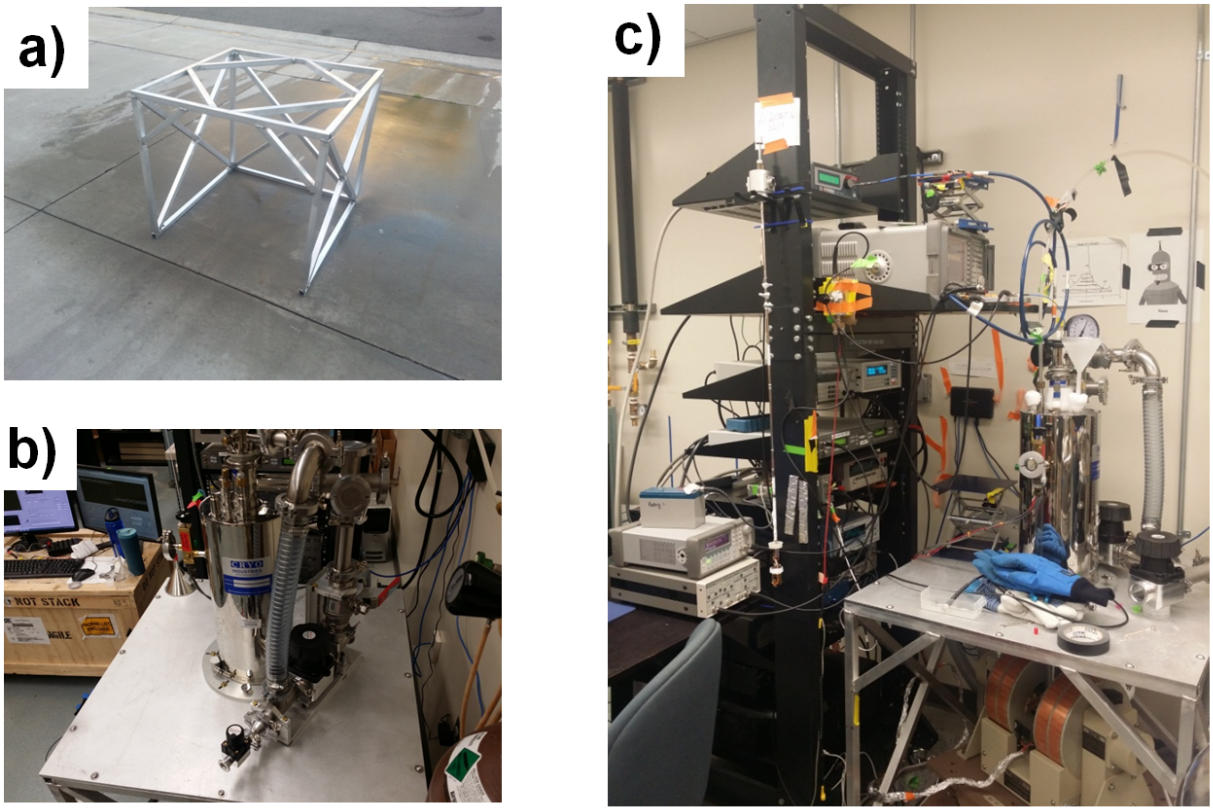

Figure 2.14: **a)** Support structure for the cryostat table. **b)** Valve support structure. **c)** Completed cryostation

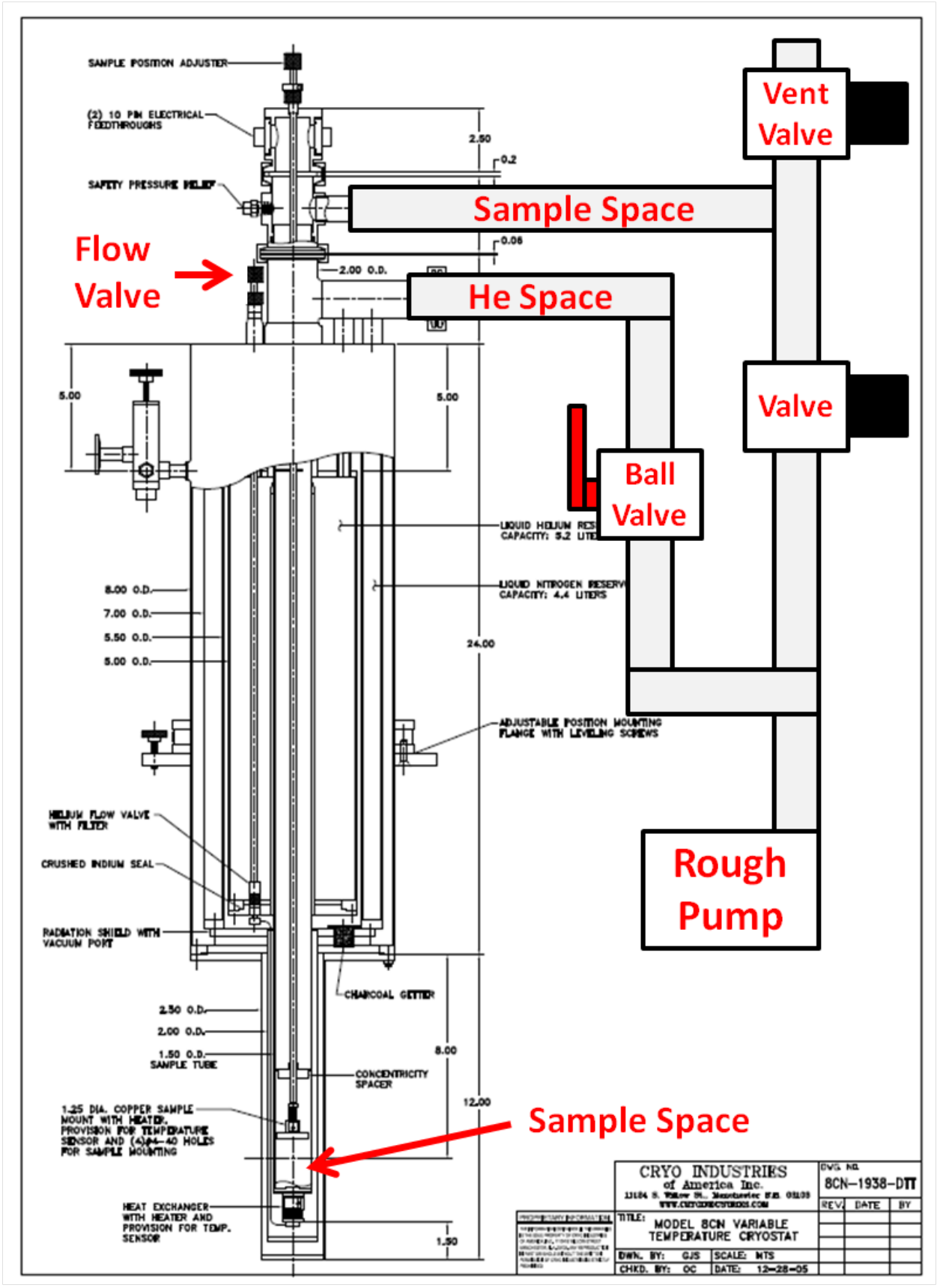

Figure 2.15: Schematic for the cryostat with the valve configuration.

15 minutes. Then usually I fill the spaces with He gas and pump once again to flush the cryostat. If the cryostat has been sitting for a while I will repeat this procedure a few times.

After flushing the cryostat at room temperature, the nitrogen jacket is then filled with liquid nitrogen to start cooling the system. The main purpose of this jacket is to insulate the liquid helium, however the cryostat can be cooled to 100K with just the jacket. Pre-cooling the cryostat like this is not completely necessary, but less liquid helium will be wasted during transfer since the chamber is closer to 4.2 K.

The most common problem with cooling down the cryostat or transferring in liquid helium is freezing the flow valve internally or externally. Freezing on the exterior is relatively simple to fix by using a heat gun to melt the ice on the brass knob. If the knob still refuses to turn, a pair of pliers can be used to free it. Generally rocking the valve left and right gently works for this. Internal freezing of the capillary is the other potential failure point. The sign of this is usually the flow valve knob turns, but the cryostat will not cool. There is a heater on the flow valve placed there for this situation. Applying heat to the capillary can some times free it up. However, this is risky since it operates in open loop and if too much heat is applied it can possibly melt the solders and damage the cryostat. I would not recommend using this too often.

In theory the cryostat can be operated using only liquid nitrogen. This was attempted early in the project but seemed to have caused damage to the cryostat. Inside the helium space there is a mesh grating that ended up getting plugged, requiring the cryostat to be sent back to the manufacture for repair. The clog was caused by a black residue. Although the exact origin of this residue is unknown, it is highly likely it came from the liquid nitrogen since it is not completely free of contaminants.

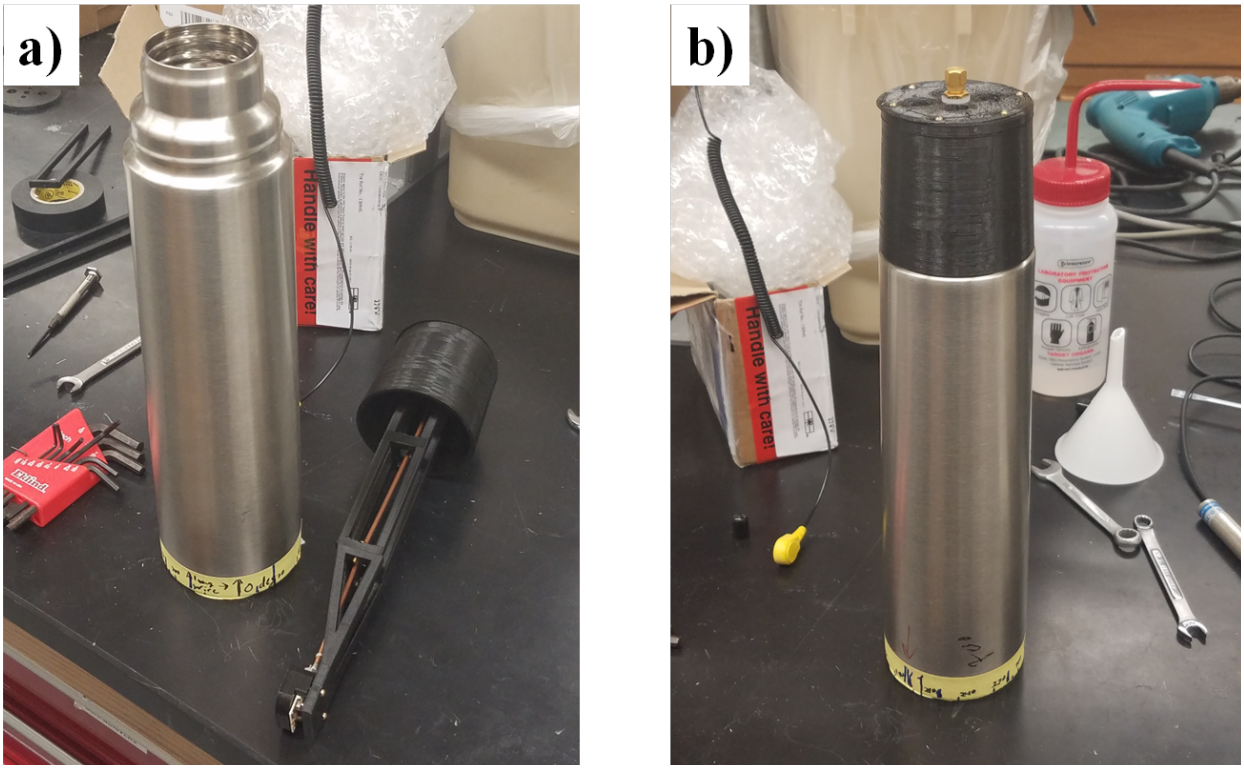

Figure 2.16: Thermos based cryostat with **a)** insert removed and **b)** installed.

2.6.2 High Tech Liquid Nitrogen Cryostat

While the liquid helium cryostats are useful, there are multiple projects using them so there can be long wait times. Also liquid helium is not cheap. For some projects using liquid helium (4.2 K) is overkill and liquid nitrogen temperatures (77 K) works well enough. There are commercially available liquid nitrogen cryostats available, but these are not much cheaper than their helium counterparts. A simple solution is to use a thermos and submerge the sample in liquid nitrogen. Although the temperature can not be controlled, it allows for some exploratory work to be done or just provide simple cooling. In the later chapter describing auto-oscillations induced by the planar Hall torque a thermos worked well for keeping the sample cool enough for emission measurements.

Figure 2.16 shows the exact thermos used, which is a Isosteel VA-9554Q with 0.9 L capacity. This thermos has a vacuum jacket in it and can hold liquid nitrogen for around 12 hours,

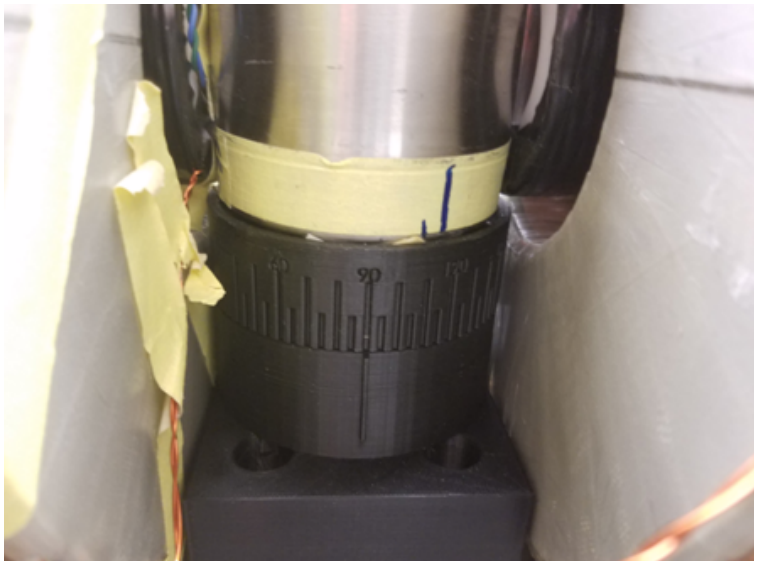

Figure 2.17: Base that the thermos sits on and angular scale.

which is plenty of time for measurements. It is made of a stainless steel alloy that is relatively nonmagnetic and most importantly fits between the pole pieces of the GMW 5403 magnets used. One important thing to keep in mind when using something like this is to make sure it is never sealed or else it could explode. I always have at least two holes in the top for pouring nitrogen in and venting.

To hold the sample, a cap and support structure where made with a 3D printer. A microwave bulkhead is placed on the top of the cap and a microwave cable runs down to the sample. The sample is placed at the bottom so that it is submerged in nitrogen for the longest time. The sample is not completely covered on this design and in a second revision should be. Sometimes when liquid nitrogen is poured in when the thermos is warm the rapid evaporation of nitrogen can cause the wire bonds on a sample to pop off.

The thermos sits on a rotatable base shown on Fig. 2.17 so that angular dependencies can be measured. Generally I secure the thermos to the base with double sided tape. When it is a new sample, I preform a quick resistance vs angle measurement to determine the orientation of the sample. I then reorient the thermos on the base such that an angle of 0 corresponds to an axis of the sample.

When using the thermos, it is necessary to clean out the ice that forms in it over time. The system is not sealed to prevent an explosion and this leads to the accumulation of ice from the vapor in the air. This ice can cause a sample to die if the thermos runs out of nitrogen and it begins to melt. Water can then short the contacts and has been seen to kill samples when this happens.

Chapter 3

Nanofabrication

3.1 E-Beam Lithography

3.1.1 Basics

The process used is heavily dependent of a technique known as e-beam lithography. In it a resist is spun on to the chip and then using a modified scanning electron microscope (FEI Magellan in this case), areas of the resist are exposed to the focused electron beam. This beam is then rastered across the substrate to create a pattern. If a positive resist such as PMMA is used, the area exposed to the electron beam can then be developed to expose the substrate where the beam had been passed over. On the other hand for a negative resist such as MAN-2401, the exposed area remains after development. This process creates the necessary masks that will be used to add and remove material. Details of the resist application procedures are detailed in Appendix A.

The writing process on the Magellan SEM is run by the Nanometer Pattern Generation System (NPGS) software. Many of the advanced options are locked out by default when a

```
9.000


PlayWav 1 2

PlayWav 2 3
not used
focus.bat
not used
Scope2.bat




Reserved
Reserved
Reserved
Reserved
```

Figure 3.1: Configuration of the PgCmnd.sys file to enable automatic current switching and X–Y focus mode.

user creates a new project using this software. Specifically, the ability for NPGS to switch current values on the SEM and the X–Y focus mode need to be enabled. To do so, the PgCmnd.sys file in the user's project folder needs to be edited to match the version of it shown in Fig. 3.1. The line stating "Scope2.bat" enables current switching and "focus.bat" the X–Y focus mode. One should note that the line these inputs are placed on matters.

NPGS is a fairly widespread and older program that while it can get the job done, there are often various communication errors between the separate NPGS computer and the more modern SEM. These errors can be reduced by the resetting of all related computers every time. The whole procedure takes about ten minutes which wastes a small amount of time, but less so than the failure of a three hour write session. To reset everything, first stop the server on the SEM. Once the server is shut down, restart the EBL computer. Before logging into the EBL computer, make sure the server on the SEM computer is started again. Then logging into the EBL computer will initiate some sort of calibration between the SEM hardware and NPGS computer. Once the calibration is completed, log into the NPGS before imaging on the SEM or else occasionally when you log into the NPGS software it resets the SEM settings, which can undo any nice focus it currently had.

3.1.2 Setup

The beginning of the writing procedure using the FEI Magellan SEM requires first the ability to make a decent image with the ETD detector at a working distance of 7 mm. The tricky part is this has to be done with the conditions the EBL writing will use, forcing the beam voltage to be set to 30 kV and the desired write current. The current used will vary depending on the size of the feature, but generally the smaller the feature the lower the current is used. Sadly though the conditions used for writing do not produce good images so getting a good focus can take time on more insulating substrates. For larger features, the focus is not as important and often all that is needed is a rough focus, but for small features where the dimensions and aspect ratio matter proper setup of the SEM is critical. The general rule of thumb used is an image of a feature the size of the write pattern should be in good focus at least. To aid in the focusing process, scratching the side of the chip creates dust particles with jagged edges. The sharper the feature the better since it is easier to observe any problems with the focus, stigmator, and all relevant alignments.

3.1.3 Run Files

Now that the SEM is prepared for the writing session, it is time to turn to the details of the pattern file and the run files. Ideally these would be prepared ahead of time since not only is SEM time hard to get at decent hours due to its popularity, tool use has an hourly fee so being efficient with time is strongly encouraged. The patterns for the runfiles are in dc2 format and are intended to be written in the drawing program included with NPGS, but drawing with this software is not recommended. Instead Layout Editor is much easier to use and the gds files it saves in can be converted to dc2 by NPGS.

After converting the file to dc2 there needs to be the addition of a dump point in the NPGS pattern drawing software. The purpose for this is when the beam is not writing, the software

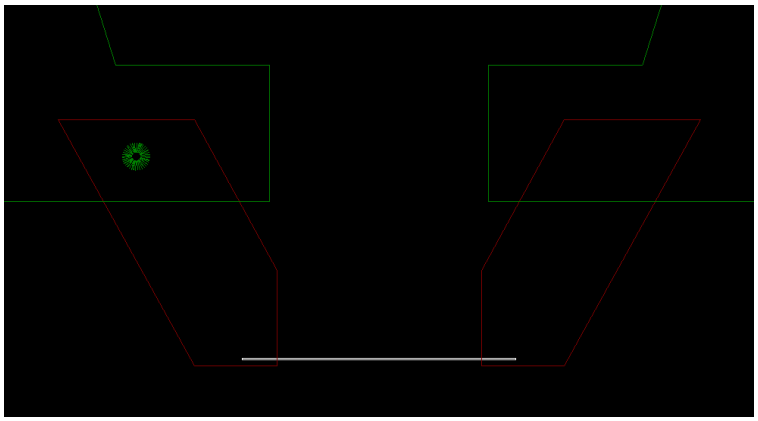

Figure 3.2: Example of a pattern file with the dump point added (green circle)

points the beam at this location. This is mainly intended for SEMs without beam blanking capabilities, but the blanker on the Magellan does not always work properly leaving behind a dot in the center of the pattern. When placing the dump point it is best to place it away from the main pattern or inside a large feature like the pattern in Figure 3.2.

Once the pattern is ready, the runfile as pictured in Figure 3.3 can be created. There are several parameters that can be varied and also changed for different layers in the pattern. Generally the best parameters will need to be tested for each new type of pattern. However, there are a few general trends.

The first parameter of interest is the Magnification. While I actually do not know the exact function of this, the largest value you can input into this field before the software complains gives the best result. The center to center distance and line spacing govern the distance between points where the beam will expose and setting these to the same value works best. The value used here will depend on the size of the feature and the current used.

The beam size is related to the current used so for lower currents, a smaller distance between points is needed. Also for smaller features this helps with their resolution. The write current is selected by the configuration parameter setting. This is an old convention where the number means the current list entry number referenced to one of the list entries. The

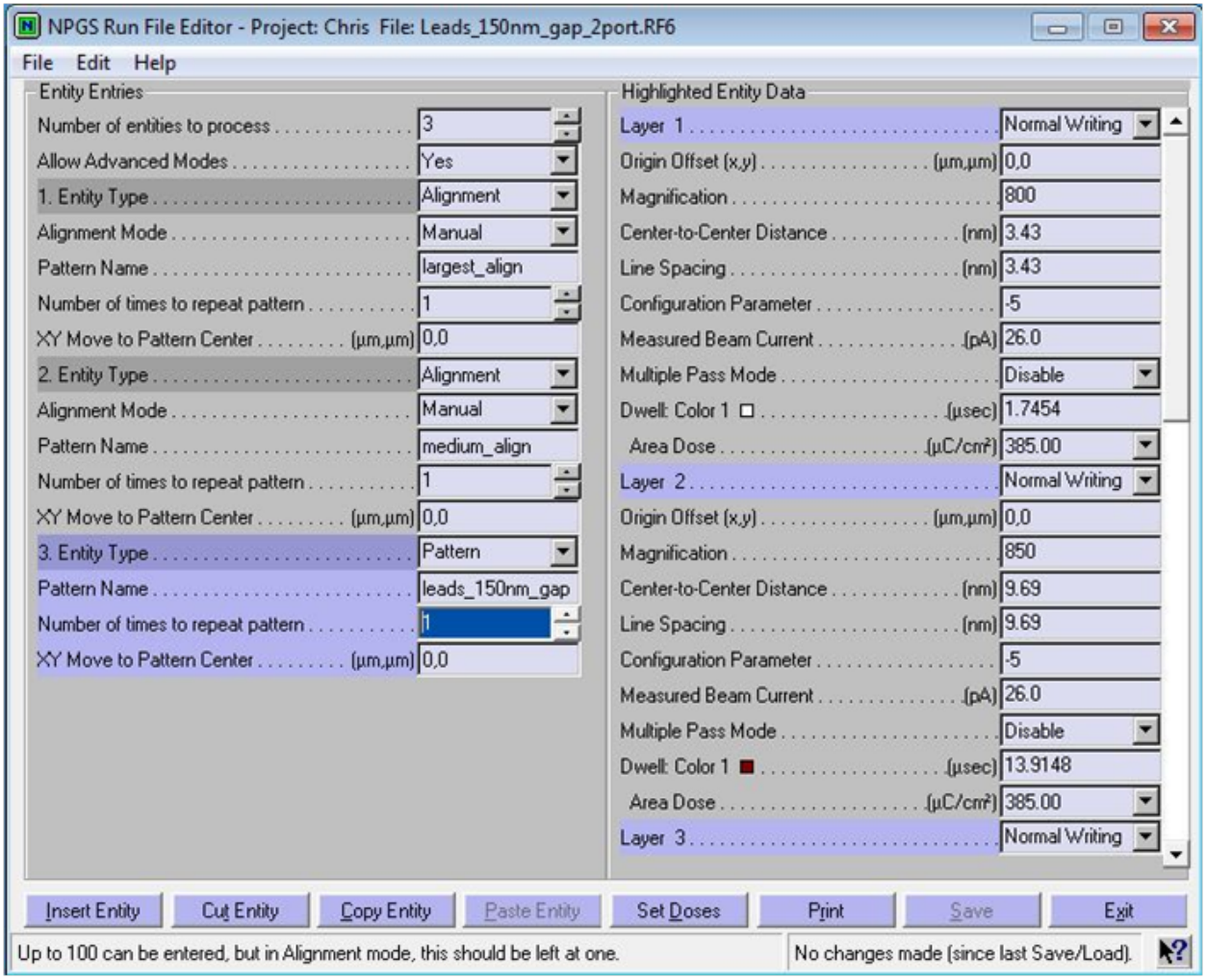

Figure 3.3: Sample runfile for the NPGS software.

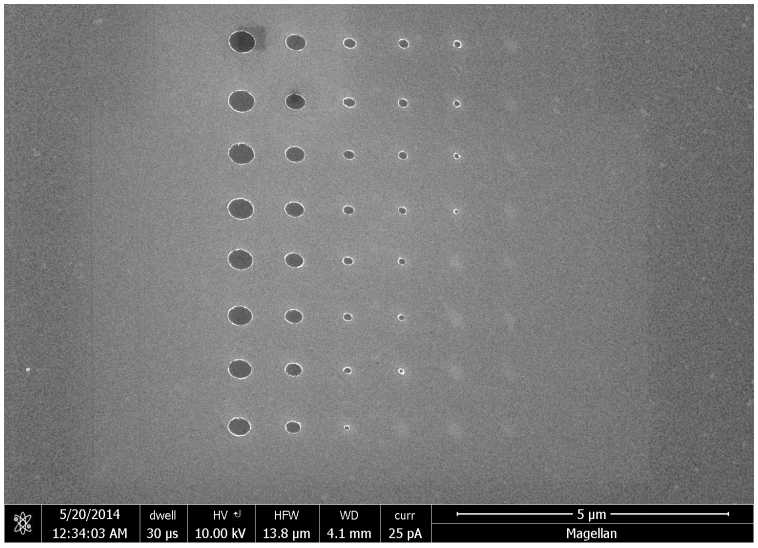

Figure 3.4: Array of ellipses with decreasing size from left to right and increasing dose from bottom to top.

measured current value allows for a correction that takes into account the actual measured current with a Faraday cup. In principle, this can just be set to the selected current and the dosage varied to make the pattern work right. However, the current source on the SEM has been known to go bad time to time. When this occurs, the actual current can be less than a quarter of the selected amount. Using the measured value in this case is imperative when using the SEM in this condition.

The dosage governs the final amount of exposure to the electron beam. There are two different dosage schemes that can be used and throughout this study the "area dose" scheme was chosen and is preferred over "line dose." For PMMA and MAN-2401, a dose around 300 works well for most larger features. For features under 100 nm, especially nanodots, the amount of required dose can be significantly higher. The simplest way to determine the proper dose is by writing an array with varying dose steps. Figure 3.4 shows an array of ellipses created by a lift off procedure. The pattern size used decreases from left to right and the dosage increases from bottom to top. From this test it is possible to determine the appropriate dosage for the desired feature size. For features like leads, it is useful to know how the feature size depends on dose. Say for a row of samples different gaps between the

leads are desired. For achieving a narrow gap between leads a useful trick is to just vary the dose to control feature size, since it is quicker to change the dose than to alter the pattern files during an EBL session.

3.1.4 X–Y Focus Mode

Inevitably, the sample will not sit completely flat on the sample holder on the scale of nanometers. The result of this is when one corner of the chip is in focus, if you move to the other side it will be out of focus since the height is no longer at the focal point it was at earlier. This can lead to distortions in the pattern on small sized features. To prevent this, the X–Y focus mode allows for tilt correction.

The process is started by first getting the stage height to 7 mm and in focus with the stigmator adjusted as best as possible. Then under the "Commands" menu on the main NPGS screen, select "Direct Stage Control." Follow the prompts to acquire new data. Then go to each corner of the sample, adjust the focus and press space. Do not adjust the stigmator during this process since this mode does not control the stigmator. Usually scratching all four corners with a scribe assists in this. Once the data is collected, follow the prompts to see the fit NPGS makes assuming the sample is just a tilted plane. Accept the values then follow the prompts out of the window. This will need to be done for each session since it will vary chip to chip.

Lastly, the runfile needs to have this mode enabled. To do so the changes in Fig. 3.5 need to be made. First make sure "Allow Advanced Modes" is set to yes. Then if the X–Y focus mode is to be used "Disable X–Y Focus mode" needs to be set to no. Otherwise it will just use the last focus setting before entering NPGS mode. Conversely, if "Disable X–Y focus mode" is set to yes the system will ignore any saved focus settings and just use the focus seen on the screen.

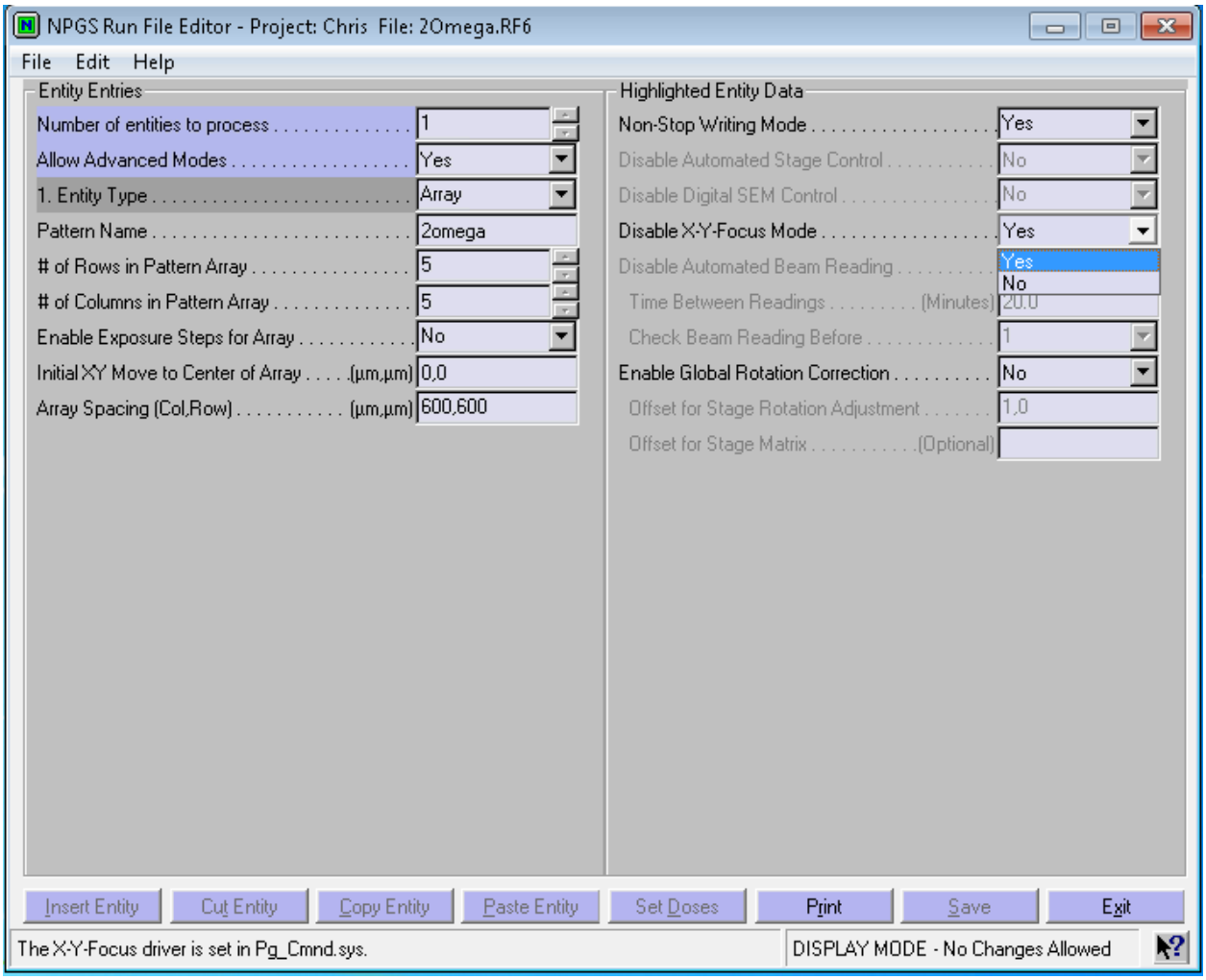

Figure 3.5: Modifications to the runfile to enable X–Y focus mode.

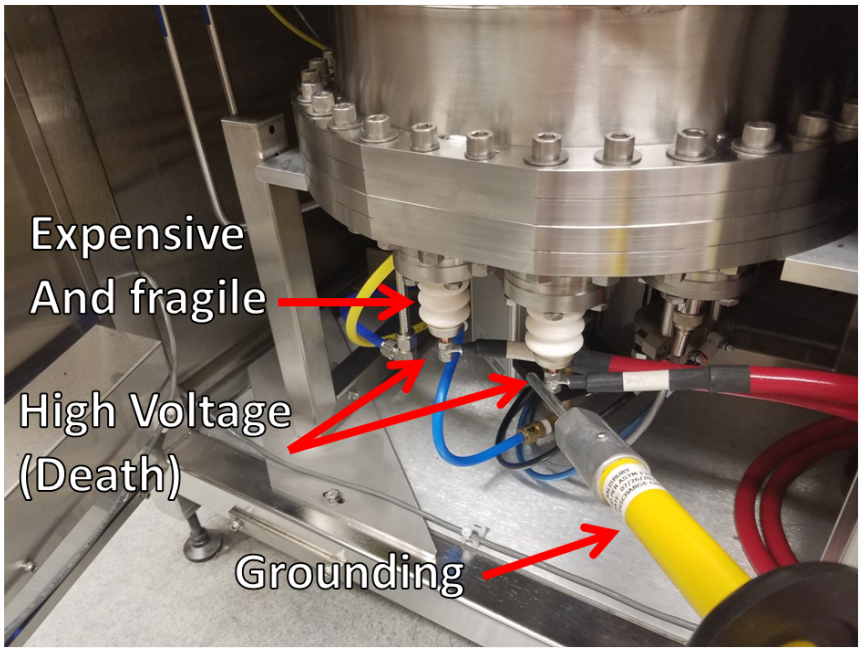

Figure 3.6

3.2 Intlvac E–Beam Evaporator

3.2.1 WARNING!!!!!!

The e–beam evaporator uses a high voltage power supply that can cause death if any of the high voltage contacts are touched. As such, the casing for the system should never be opened during operation. Even after operation, the capacitors in the power supply can hold a voltage. There are two easy to get too connections that carry this voltage shown in Fig. 3.6. If the cabinet for the system is ever opened, these connections must be grounded using the rod shown touching the right connection in Fig. 3.6. Also note the white section of these parts is fragile and easy to break if you tap them with the rod. These are not cheap to replace and will cause the system to become inoperable until repairs are done.

3.2.2 Standard Operation

Operation of the evaporator requires the powering on several of the components. For this section, switches on the panels in Fig. 3.8 will be referred to as "FP" followed by a number and for the panel in Fig. 3.9 "PS." Starting with the chamber fully vented the procedure is as follows.

1. Disassemble the doghouse and check for flakes. (See later section for procedure on how to disassemble) Ensure the crucibles that are to be used are full.
2. Flip on the breaker marked "Control" (PS1) in the Power Supply.
3. Power on the TT Controller (FP9) and the index controller (FP1).
4. The pocket indexer will ask if you are in pocket 1 on FP2. Press ok if the system is in pocket one. If not use the manual find home option on FP2.
5. Vacuum out the area around the evaporator and pockets. Use new gloves after handling.
6. Reassemble the Doghouse.
7. Place sample on stage and secure it with clips as shown in Fig. 3.7
8. Close chamber door and pump down to at least 3×10^{-6} Torr.
9. Power on the stage chiller
10. Flip on the breaker marked "High Voltage" (PS) in the Power Supply
11. Switch the display to filament (FP13) on the TT Controller display. Power on the filament (FP12). This should reach around 17.5 A and be stable.

12. Power on the high voltage (FP11). Periodically the voltage will need to be tuned to keep the electron beam in the center of the pocket as the magnet ages.

13. Check the light labeled "ARC" (FP10). If flashing there is a chip shorting out the source that needs to be cleaned.

14. Set the Pocket Indexer (FP2) to remote.

15. In the ion mill control software "Status" tab shown in Fig. 3.10, set the system into manual mode (red arrow).

16. In the ion mill control software "Chamber" tab shown in Fig. 3.11, set the stage angle to the desired deposition angle

17. Enable the stage rotation.

18. Set the sweep type on the sweep controller (FP14). Circular (Pattern 1) works best for granular materials and no sweep for materials that melt into a slug.

19. Begin the deposition process on the Inficon SQC–310 controller. (see later section for controller configuration)

20. Switch the display to "EMIS" (FP13) to see the emission current and verify the deposition controller has proper control.

21. Once the rate is stabilized, open the shutter using the ion mill software and press zero on the Inficon SQC–310 to zero the thickness measured by the crystal.

22. After deposition, ensure that pocket one is selected.

23. Switch off the high voltage (FP11) and filament (FP12)

24. Power off the High Voltage breaker on the power supply (PS2).

25. Stop the stage rotation and close the stage shutter.

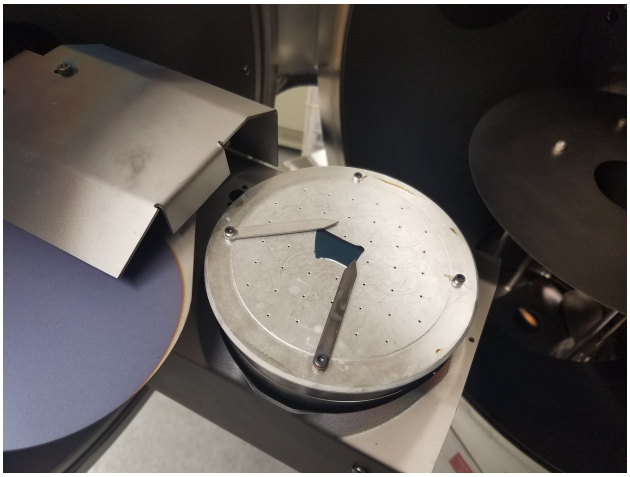

Figure 3.7

Figure 3.8

26. Rotate the stage back to zero degrees in the ion mill software.

27. Return the ion mill back to "Auto," blue arrow in Fig. 3.10.

28. If the system will not be used again in a short period of time, power down the indexer (FP1), Controller (FP9) and power supply control (PS1)

29. Vent the chamber and remove sample.

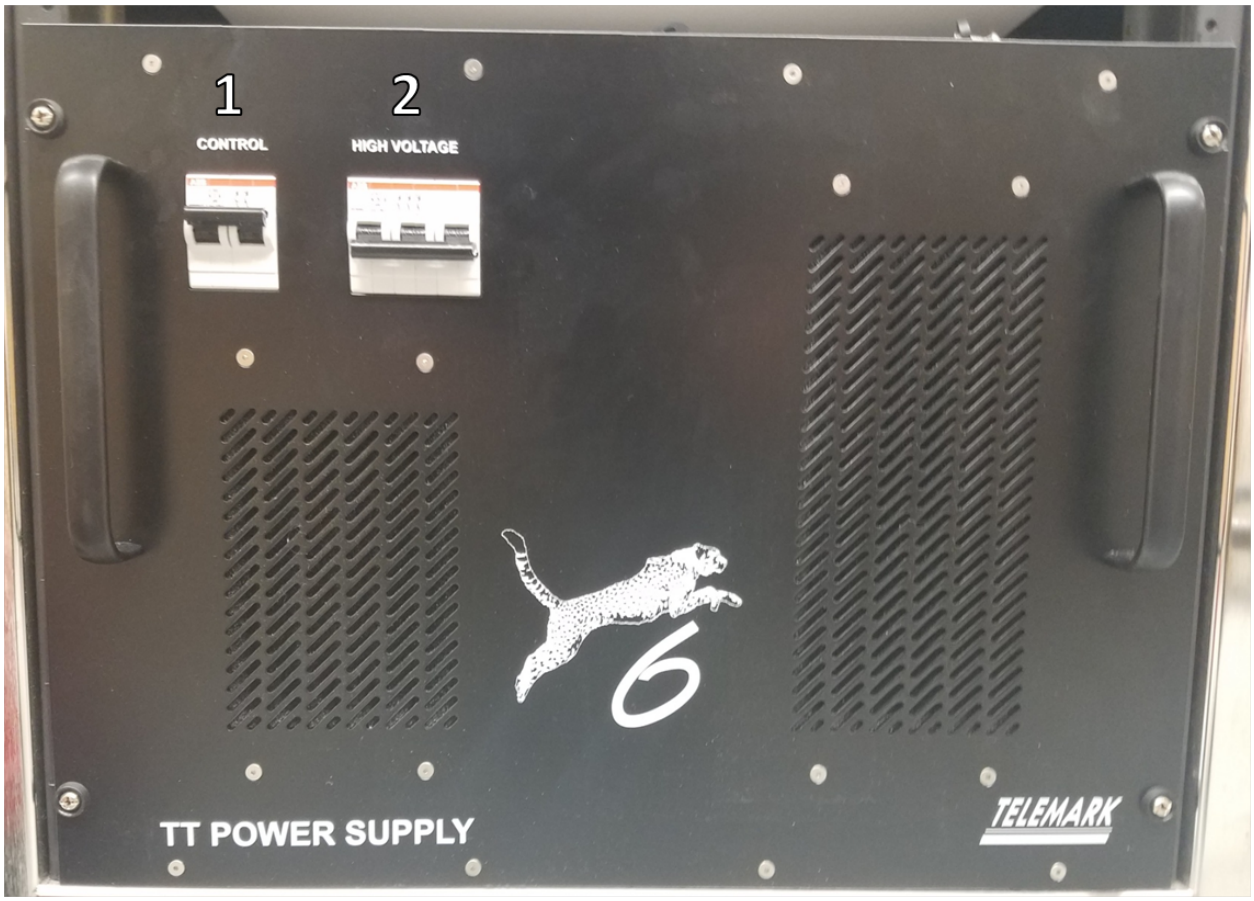

Figure 3.9

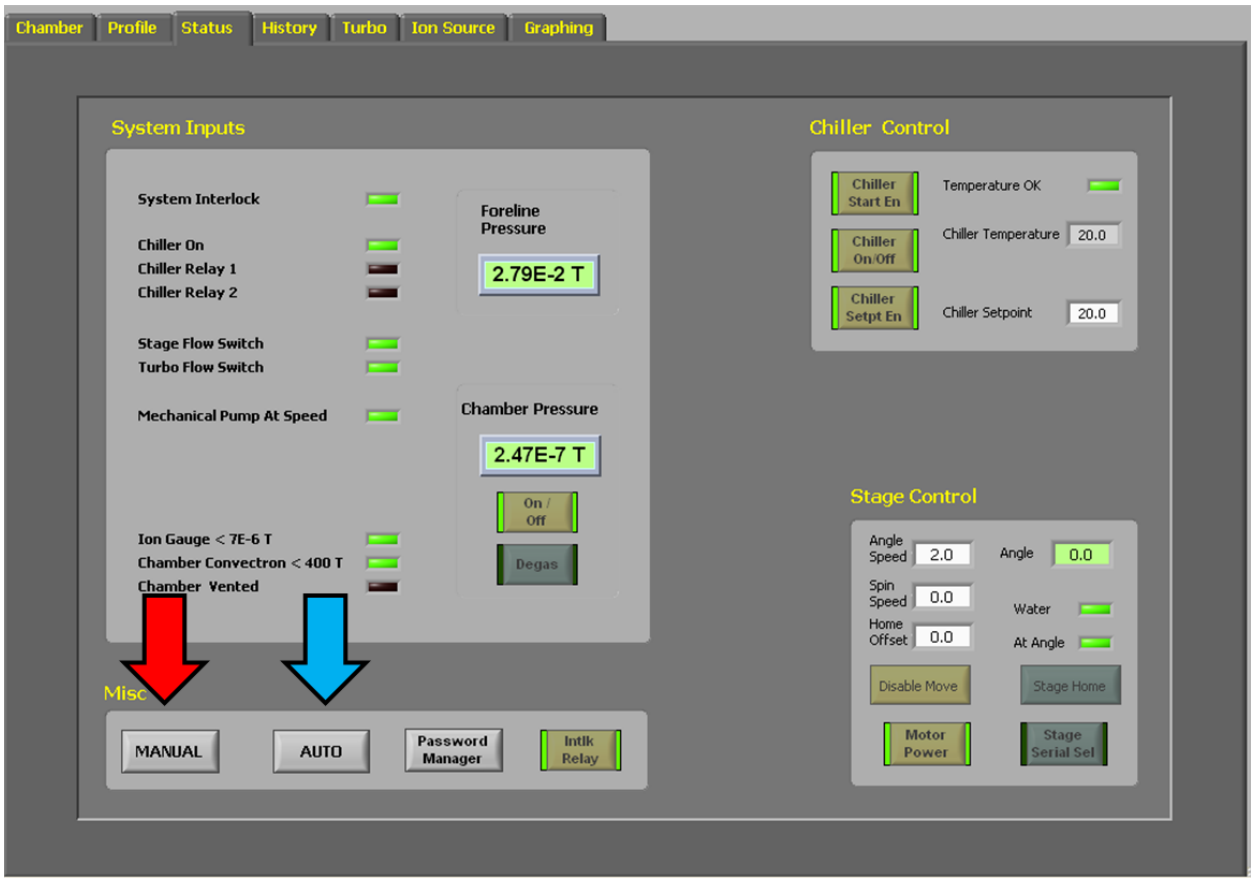
Chamber
Profile
Status
History
Turbo
Ion Source
Graphing
System Inputs
System Interlock
Chiller On
Chiller Relay 1
Chiller Relay 2
Stage Flow Switch
Turbo Flow Switch
Mechanical Pump At Speed
Ion Gauge < 7E-6 T
Chamber Convectron < 400 T
Chamber Vented
Foreline Pressure
2.79E-2 T
Chamber Pressure
2.47E-7 T
On / Off
Degas
Misc
MANUAL
AUTO
Password Manager
Intlk Relay
Chiller Control
Chiller Start En
Temperature OK
Chiller On/Off
Chiller Temperature
20.0
Chiller Setpt En
Chiller Setpoint
20.0
Stage Control
Angle Speed
2.0
Angle
0.0
Spin Speed
0.0
Water
Home Offset
0.0
At Angle
Disable Move
Stage Home
Motor Power
Stage Serial Sel

Figure 3.10

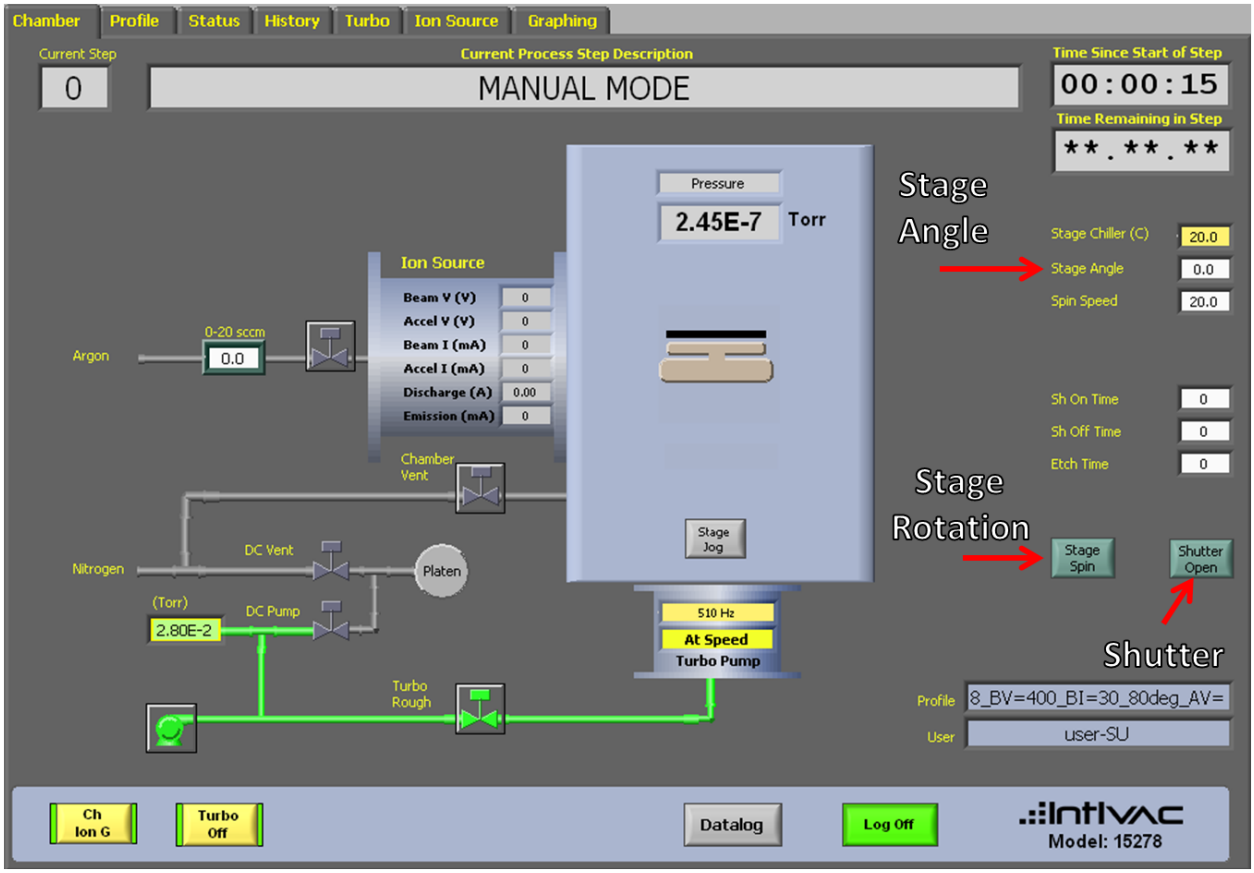
Chamber
Profile
Status
History
Turbo
Ion Source
Graphing
Current Step
0
Current Process Step Description
MANUAL MODE
Time Since Start of Step
00:00:15
Time Remaining in Step
..**
Pressure
2.45E-7
Torr
Stage Angle
Stage Chiller (C)
20.0
Stage Angle
0.0
Spin Speed
20.0
Ion Source
Beam V (V)
Accel V (V)
Beam I (mA)
Accel I (mA)
Discharge (A)
Emission (mA)
0.00
Argon
0-20 sccm
0.0
Chamber Vent
Nitrogen
DC Vent
Platen
(Torr)
2.80E-2
DC Pump
Turbo Rough
510 Hz
At Speed
Turbo Pump
Stage Jog
Sh On Time
Sh Off Time
Etch Time
Stage Rotation
Stage Spin
Shutter Open
Shutter
Profile
8_BV=400_BI=30_80deg_AV=
User
user-SU
Ch Ion G
Turbo Off
Datalog
Log Off
Intlvac
Model: 15278

Figure 3.11

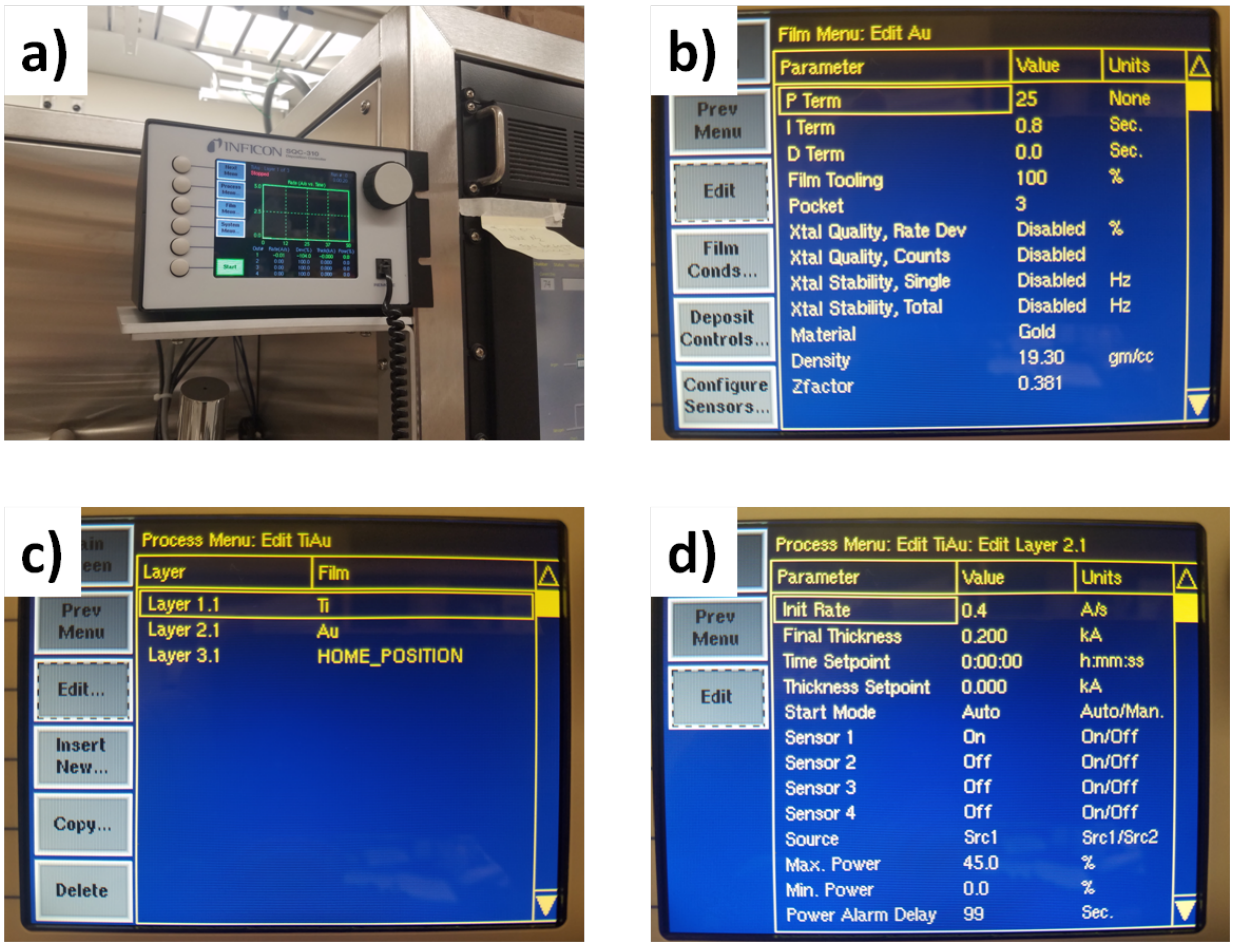

Figure 3.12

3.2.3 Deposition Controller Programming

The evaporator depositions are controlled by a Inficon SQC–310 pictured in Fig. 3.12a. In its current configuration, it can control everything except:

- Sweep type
- Stage angle
- Stage shutter
- Stage rotation

To set up a deposition, the film needs to be defined. Pressing the "Film Menu" option on the main screed brings the user to the list of programmed films. Selecting a film or making a new one brings the user to the screen in Fig. 3.12b. Here the material density and Zfactor are defined. The controller has a built in library of materials and for most materials only the name needs to be set and these fields should auto fill. **NOTE:** The I term of the PID needs to be set for new materials. See section on this for details.

After the films are defined, from the main screen select "Process Menu" to define the full deposition process. Select the desired process or create a new one. Figure 3.12c shows an example of the steps in a process. Multiple layers can be defined. The layer called "HOME POSITION" rotates back to pocket one after the process is done. This is important to add to a process since the indexer is not left on all the time and when power cycled, it forgets its location

To set the characteristics of the deposition, select a layer and the screen shown in Fig. 3.12d is reached. When making a new process the following need to be defined:

- Init Rate
- Final Thickness
- Start Mode set to Auto
- Sensor 1 needs to be set to On
- Max Power
- Slew Rate

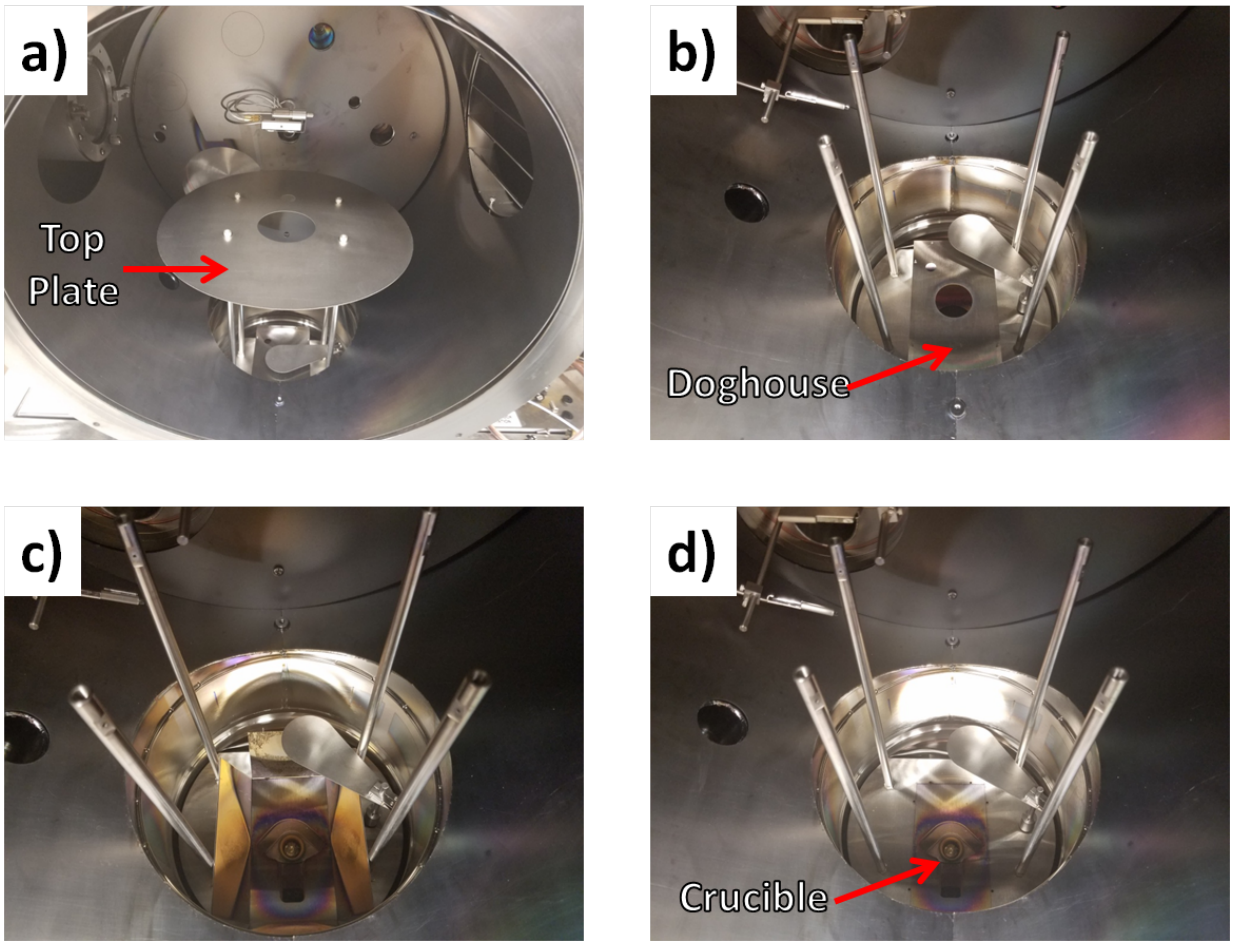

Figure 3.13

3.2.4 The "Doghouse"

The "Doghouse" is a group of shields designed to prevent deposition of material onto the chamber walls. Before each deposition, the parts of this structure need to be inspected for flakes. Figure 3.13 shows the assembly as it is taken apart. To disassemble:

- Remove top plate taking care to note the orientation of the plate. The screws should just be hand tight. Also note that these are special screws with holes drilled down the center to prevent the trapping of air in the screw holes.
- Inspect the top plate for flakes. Use a wipe and Isopropyl Alcohol to remove loose flakes. Sand blast and clean with Acetone/IPA if too much material present.
- Disassemble the doghouse. This is held together with pins. Take careful note of the direction of the holes in the top plate.
- Inspect the parts for flakes. Use a wipe and Isopropyl Alcohol to remove loose flakes. Sand blast and clean with Acetone/IPA if too much material present.

To reassemble the structure repeat these steps in reverse.

3.2.5 Material Loading

The evaporator has four 7 cc pockets that can accept the crucibles shown in Fig. 3.14. For oxide materials it is recommended to keep the crucible as full as possible and if possible stir the material often. To load a crucible, disassemble the doghouse first. **For safety ground the area around the crucible first.** Use tweezers to remove and fill crucible.

New materials will need to be melted. This is easiest done with the doghouse disassembled since it obscures the camera's view of the crucibles.

Figure 3.14

3.2.6 Observing the Melt

The location of the e-beam in the crucible and viewing of the material melt is achieved through the use of a camera. For best observation, the doghouse needs to be disassembled. Time to time this is necessary to check the position of the beam in the crucible and to melt new material.

Figure 3.15 shows the location of the hole for the camera. Two mirrors are used to image the location of the crucible. These mirrors will periodically need to be cleaned of material since they are exposed to the deposition. Use a wipe and IPA to clean off any flakes.

To access the camera, use the "Cam Expert" software. Figure 3.16 shows the main screen for this software with the camera on during a deposition. To acquire video, press the button indicated in Fig. 3.16.

3.2.7 Crystal Replacement

The system has two crystal monitors that can be used to monitor the thickness of deposited material. These crystals have a finite lifespan determined by the amount of material de-

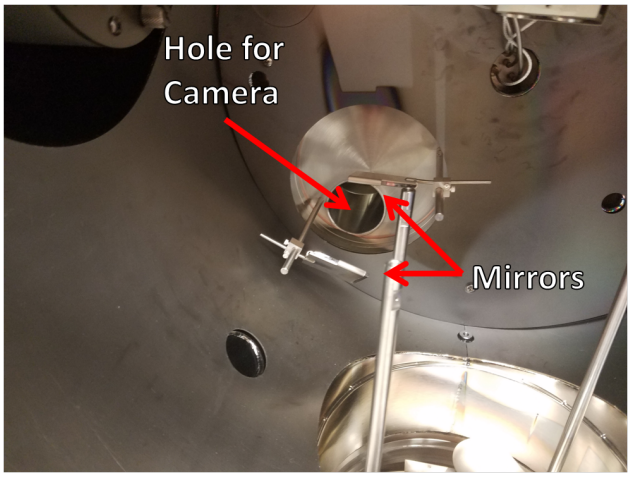

Figure 3.15

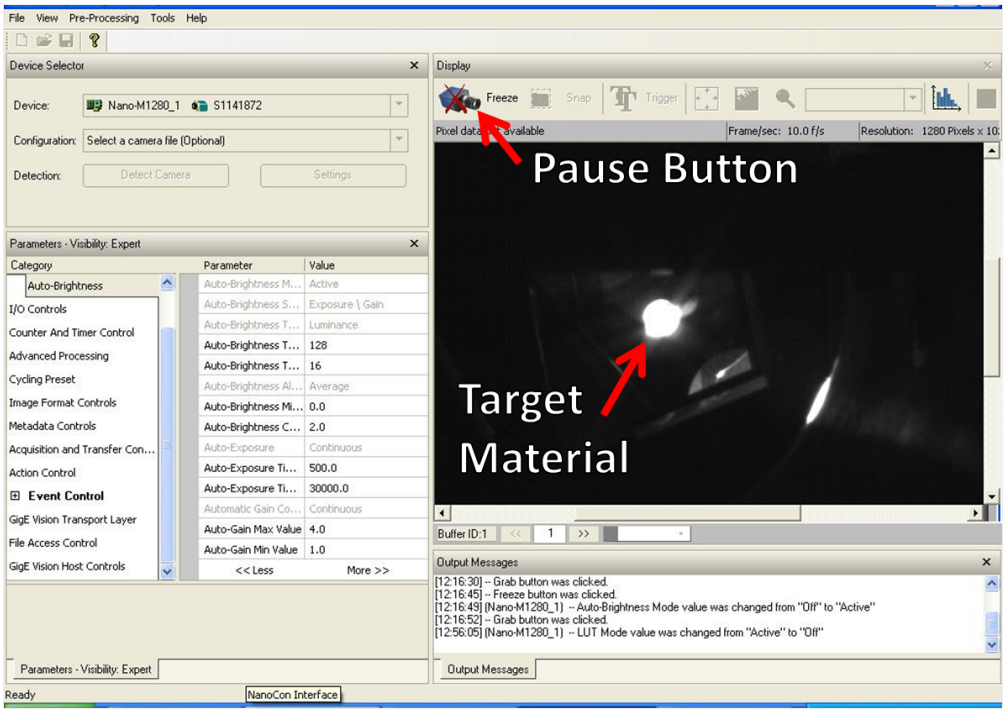

Figure 3.16

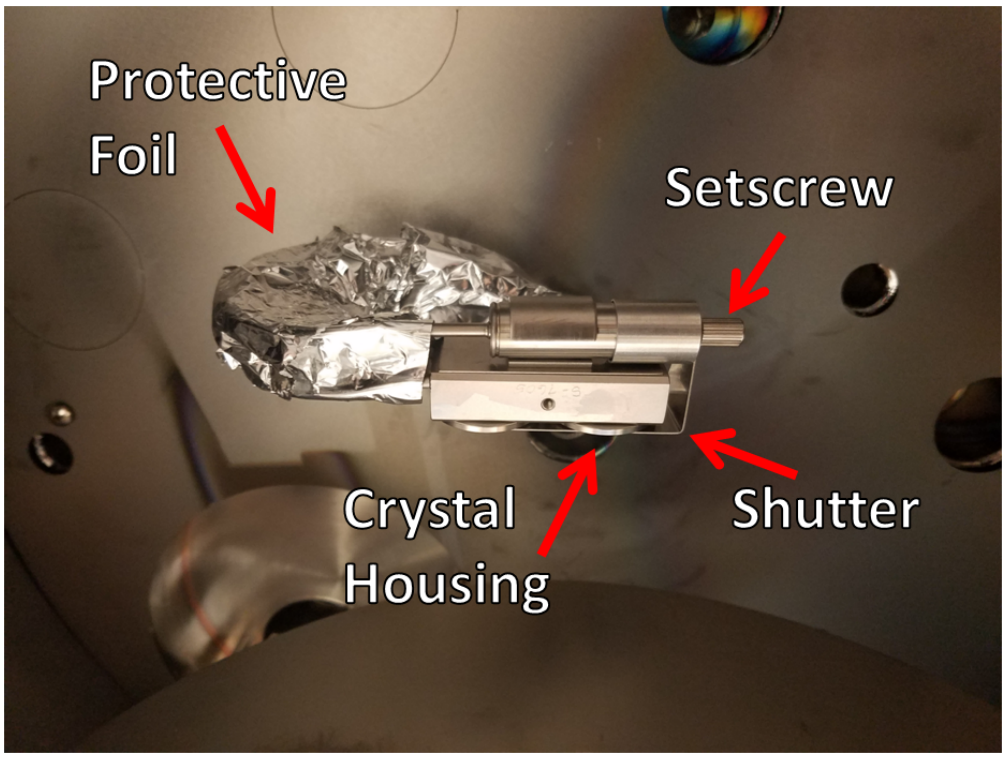

Figure 3.17

posited onto them. The life of the crystal can be read from the Inficon controller. If the life of a crystal is less than 30 percent, it needs replacement. The holder for the crystals is shown in Fig. 3.17. To replace the crystals:

1. Remove setscrew and shutter.
2. Pull down on housing encircling the crystal. This is held in by friction.
3. Remove crystal from housing and replace.
4. Push housing back into the monitor.
5. Verify the Inficon controller sees the crystal.
6. Reattach the shutter for the crystal.

Also note the foil in Fig. 3.17 is important. It protects the cables for the crystal monitors from the ion source beam during ion mill etching. Without it these cables can be damaged and are not cheap to replace.

3.2.8 Setting up the Integration Time

The I term in the PID tuning for a layer's deposition rate needs to be manually configured. To do so:

1. Follow steps 1–11 in the standard operating procedure.
2. On the TT Controller, set the control select (Fig. 3.8 FP6) to handheld.
3. Using the handheld controller, ramp the power up slowly until you reach the desired deposition rate and record the power.
4. Ramp the power down to a third of the power that gives the desired deposition rate.
5. Then set the power back to the power that gives the desired deposition rate.
6. Using a stopwatch, time how long it takes for the deposition rate at this new power to get to two thirds the desired rate.
7. This time multiplied by two is the I term that is entered in the layer menu.

3.2.9 Sandblasting

Eventually enough material will be deposited onto the doghouse, shutters, and stage to warrant a more thorough cleaning. There are spare parts for the doghouse and shutters so that the spares can be cleaned first and swapped in. There is no spare stage however. To

clean these parts, a sandblaster can be used to remove most of the deposited material. After sandblasting, the parts need to be sonicated in acetone for 30 minutes followed by IPA for 30 minutes. Failure to do so will cause damage to the system since the sand particles get into the filaments and cause issues.

3.3 YIG/Pt Nanowires

3.3.1 Process Overview

Before going into details of the procedure which will be discussed in the following sections, the general overview of the process used to make YIG/Pt nanowires is illustrated in Figure 3.18 and an itemized version is available at the end of this section. First staring from YIG/Pt films, alignment marks are patterned by using a lift off procedure. These serve to align the multiple steps in the process and locate the center of where a device should reside and without them, it would not be possible to properly attach the electrical leads to a nanowire. Next using a negative resist MAN-2401, the outline of the wires is defined. Then an ion mill is used to remove material leaving only the YIG/Pt under the remaining resist. In order to make a good electrical contact to the wire, the resist is removed using oxygen plasma etching. Lastly, electrical leads are added using a lift off based procedure.

3.3.2 Film Deposition

The Yttrium Iron Garnet thin films are prepared by collaborators at Colorado State University using sputtering techniques [50]. Gadolinium gallium garnet (GGG) is used as a substrate due to its good lattice match with YIG. Platinum is then deposited at room temperature in the sputtering chamber located in our lab. Just prior to the deposition, the stage

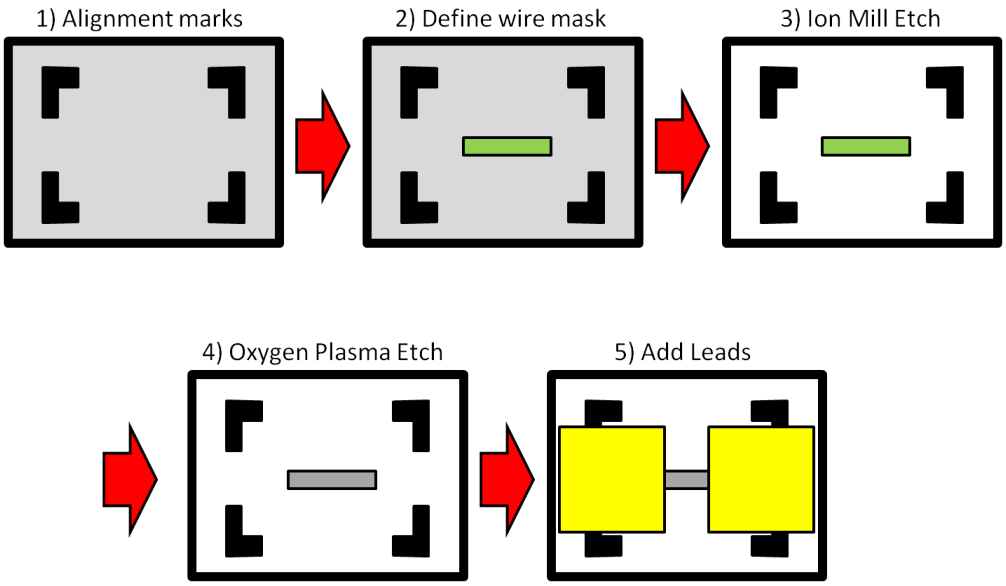

Figure 3.18: General process flow for the fabrication of nanowires used in this study.

bias is used to perform a light argon cleaning of the surface for 60 seconds at 40 percent power.

3.3.3 Alignment Marks

Alignment marks provide the important role of allowing subsequent e-beam lithography steps to be aligned to the same location. The NPGS software used for patterning allows for imaging specific areas before writing a pattern. By creating an outline of the alignment mark in the run file, one can move this outline over the imaged alignment mark. The software then uses this to calculate where the center of your pattern is. A general rule of thumb is the closer to the pattern center the marks are, the more accurate the placement of features can be.

Figure 3.19 shows the typical alignment marks used in this study. The outer, larger marks serve to provide an easy to locate feature for a rough alignment. After the first alignment, the final alignment is done using the middle alignment marks. It is important that when

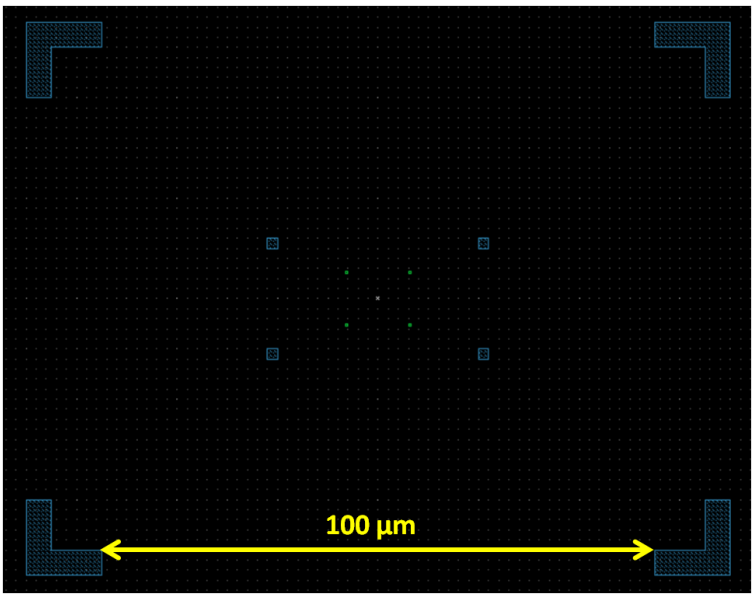

Figure 3.19: Pattern for the alignment marks used

doing the alignment, the current is set to the same one as the write current. Often there is an offset in location for different currents.

On the pattern there are one more level of alignment marks for an even finer alignment and give an accuracy of about 15nm in placement. Figure 3.20 shows an SEM image of a nanodevice made for a different project using the full alignment, where a wire runs over a nanodot of another material at the center of the image. However, for the type of patterns made in this study, this level of accuracy is not required so these marks where not used.

The alignment marks are written in an array into PMMA resist. The details of the resist development are in Appendix A. Then material is deposited onto the chip. In principle the material used is not too important and just about any metal that will adhere to the chip's surface material will suffice. 30 nm of Tantalum seems to work well for alignment marks and has the benefit of being a relatively cheap material.

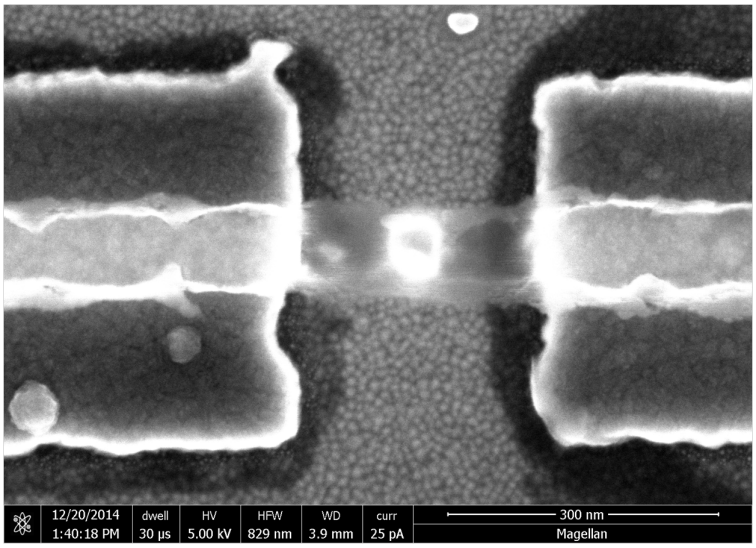

Figure 3.20: SEM image illustrating the level of alignment that can be achieved using the alignment marks, where a wire is written over a nanodot at the center of the image.

3.3.4 Wire Definition

Next the YIG/Pt wires are defined. A subtractive process involving ion milling was used due to the nature of the YIG/Pt thin film growth. Since high temperatures are needed to anneal the YIG layer, a lift of procedure can not be used since the high temperatures would bake the resist and make lift off difficult. Further, lift off procedures tend to make sidewalls made from the same material as the wire, which can be seen as the bright edges in Figure 3.21. These magnetic sidewalls often become oxidized when exposed to air, and in the case of metallic ferromagnets, these oxides are often anti-ferromagnetic at low temperatures. Even just small amounts of oxides can alter material properties [51], so it is not surprising that large sidewalls can result in unpredictable behavior at low temperatures and are best to avoid.

The first step in the subtractive process is to create a mask that will define the wire. Traditionally in our particular lab, this has been made from materials such as chromium or alumina via a lift off EBL procedure. The thickness of these masks is calibrated such that very little to none remains when the ion milling step is completed. However, for these

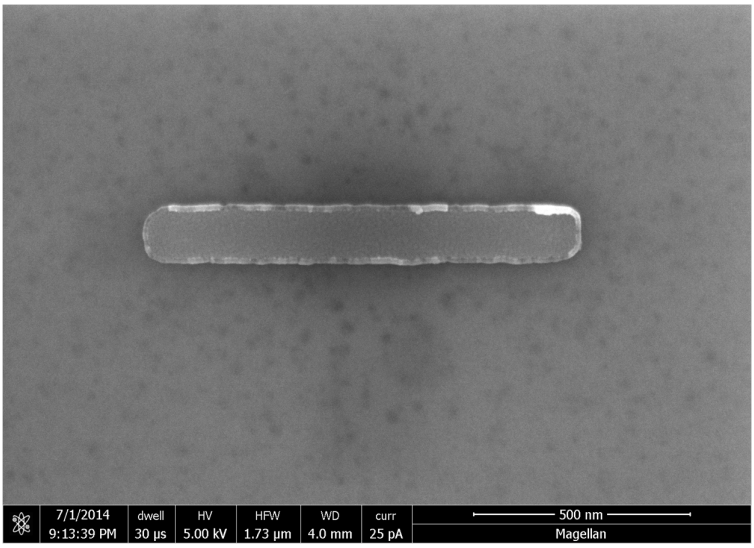

Figure 3.21: SEM image of a lift off defined nanowire showing the sidewalls around the edge of the wire.

YIG/Pt wires there are problems involved with this method. YIG etches relatively slowly and is much thicker than in previous nanowire devices made. This would require then a hard mask that is too thick to be feasible.

The first approach for a hard mask was to use a hybrid of HSQ and PMMA resists[52]. HSQ is a negative resist that when developed, forms a material similar to silicon oxide. Its etching rate is too fast to be used as a hard mask for the creation of YIG/Pt nanowires, so another material needed to be used to increase the etch time. Further, the resultant silicone oxide can not be easily removed. A method was used where first PMMA is spun followed by HSQ using the recipes in appendix A. After writing and developing the HSQ, the pattern can then be transferred to the PMMA with oxygen etching since it does not etch the HSQ, leaving the PMMA intact underneath the HSQ mask. The remaining PMMA is then plenty thick to survive the ion mill etching step. This method however did not give the desired resolution as seen in Figure 3.22. Even though the very top HSQ layer in this 1 micron circle is well formed, the pattern transfer to the PMMA layer is poor. This may not necessarily be a problem with the concept since it has been shown to work [52], but rather the tool used. For the oxygen etch a Harrick O2 cleaner was the only tool available and is primarily meant

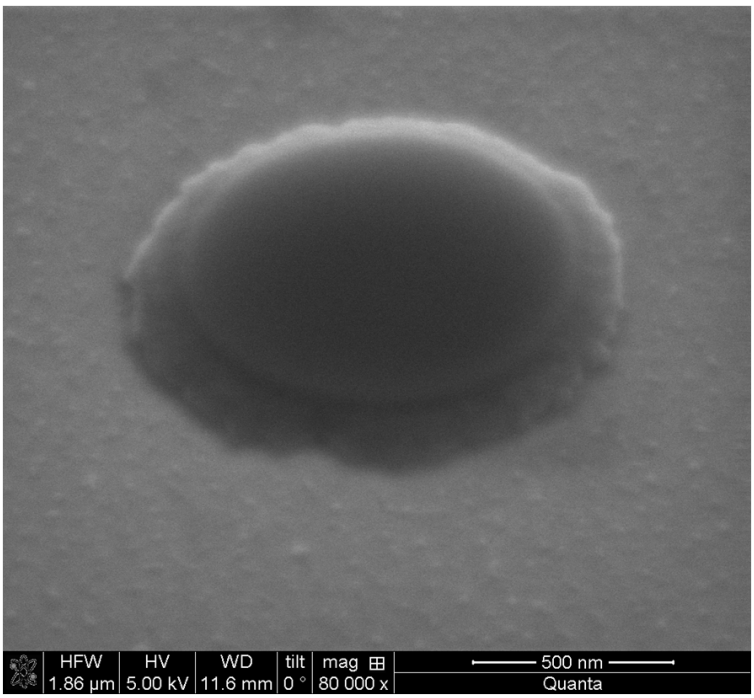

Figure 3.22: SEM image of a one micron circle of PMMA after a HSQ mask was transferred to it.

for cleaning surfaces, not a nanopatterning step.

A procedure using a negative resist MAN-2401 as the hard mask was then attempted. MAN-2401 is spun using the recipe described in Appendix A. One important thing to note is MAN-2401 is UV sensitive so exposing it to ambient light for too long can develop the entire chip. The resist is then patterned into wires using e-beam lithography. The exposure characteristics for this resist are similar to PMMA but requires slightly less dosage. This is convenient for protecting the alignment marks from the etching step since the imaged area during alignment is usually developed. After the exposed areas are developed, we arrive at the completed nanowire in Figure 3.23a.

Often times there is a resist residue present as the edges of the wire seen in Figure 3.23b. During the testing of the negative resist fabrication process this was never seen and only seems to happen on thin Pt layers placed on a fairly insulating substrate. The early testing was done on a thick Pt layer so is not likely to be related to the resist adhesion to the

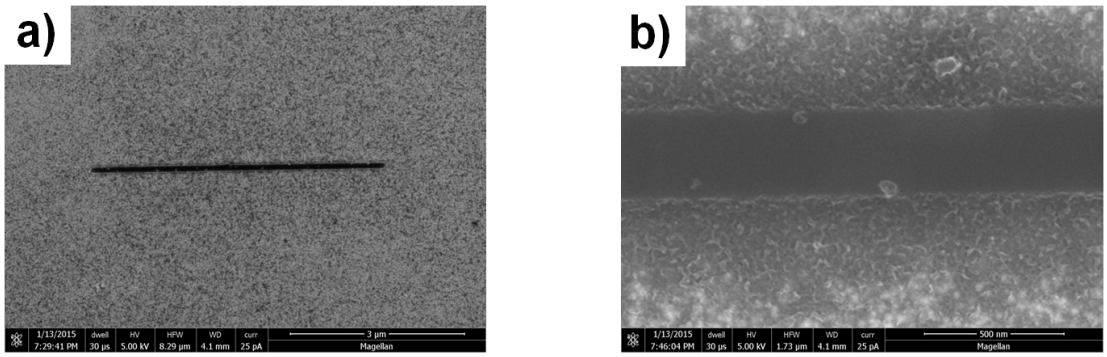

Figure 3.23: **a)** Negative resist mask for a nanowire before etching. **b)** Excess residue next to a bad nanowire.

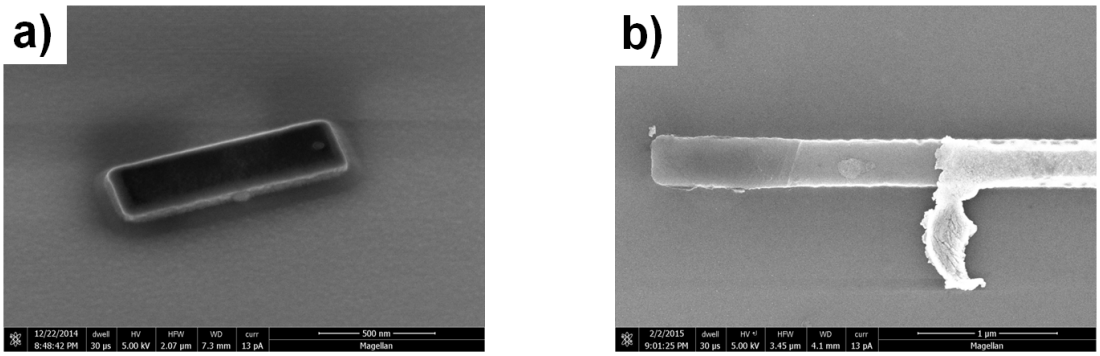

Figure 3.24: **a)** Baked on resist after an ion milling step. **b)** Partially lifted off MAN-2401 resist using acetone.

Pt. Since this only happens with thin Pt, it is probably due to the higher resistance of the thin Pt layer not dissipating the writing beam's charge fast enough. More testing would be needed to verify this. However, the residue at the sides appears to be thin in comparison to the remaining resist mask so by etching for an excessive time, the nanowire shape can be preserved.

Next an ion mill is used to transfer the resist pattern into the film. The MAN-2401 mask is roughly 100 nm tall so in order to reduce shadowing, an etching angle of 65 degrees is used, where the angle is between the ion beam and sample plane. YIG etches slow (3.7 nm/min) and since the layer is relatively thick, a long etching time is required. The etching process creates unwanted heat at the sample and tends to bake on the resist. Figure 3.24a shows an image of baked on resist from the early testing of the MAN resist etching characteristics

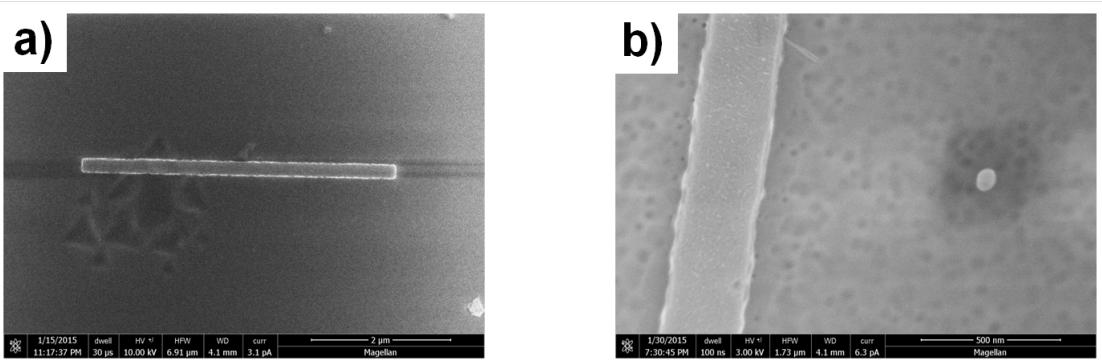

Figure 3.25: **a)** Completed nanowire after etching and with resist removed **b)** Zoomed in image of a completed nanowire showing full resist removal

using Pt on silicone substrates. After the initial testing a duty cycle of 25 percent was used to try and reduce the heating, but still results in baked on resist. The main thing to take away from this image is that there is still resist present after a long enough etch to define a YIG/Pt wire.

After the milling process it is then necessary to remove the negative resist to allow for the electrical leads to make contact to the surface of the wire. According to the datasheet for MAN-2401, this can be done with acetone but the remaining resist is usually too thin and baked on for this to be a possibility. For etching thin metals this can sometimes work. The resist seems to remove in chunks with acetone rather than being dissolved away as shown by a partially lifted off bit of resist in figure 3.24b. In theory it may be possible to lift off a thicker negative resist with acetone. However, this approach was not taken since a thicker resist will create more shadowing. To remove the remaining resist oxygen plasma etching was used with a Harrick O2 cleaner. A nine minute etch with this tool set on "High" was enough to completely expose the Pt layer giving the completed wires in Figure 3.25.

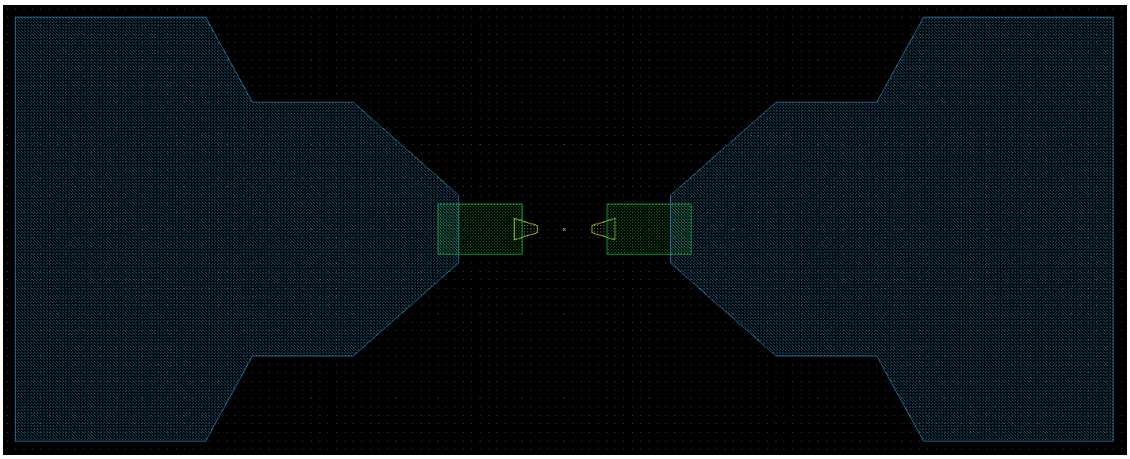

Figure 3.26: Drawing of the typical leads used.

3.3.5 Lead Definition

The last part of the process is the attachment of electrical leads to the nanowire through a lift of process. First, a layer of the positive resist MMA is spun on the sample using the recipe listed in the Appendix, followed by a layer of PMMA. MMA is affected by the electron beam more than PMMA, resulting in an undercut in the resist as illustrated in the side view of Figure 3.27. This aids in lift off of sputter deposited films.

Figure 3.26 shows a typical design for the leads used in this study. Each color represents a different layer in the drawing. Different write currents are used on each layer such that a narrow beam can be used on small features where resolution matters and a larger beam for bigger noncritical objects to decrease write time. It is important to note that the few micron overlap between layers is intentional. Often on the Magellan SEM used the alignment between different current values can be several microns off. This can result in relative shifts of the layers. While the NPGS software can be used to account for this, a simpler approach is to have overlaps on the layers if the location of the layers after the first one is not that critical.

The substrate used, Gadolinium Gallium Garnet, provides some challenges for the e-beam

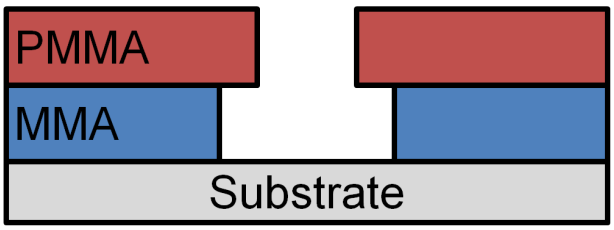

Figure 3.27: Side view of a trench made in a MMA/PMMA bilayer.

lithography process since it is insulating enough to create charging problems during the writing process. Since the writing current can not be dissipated, the charge buildup begins to deflect the writing beam causing the pattern to distort, often enough to where it is not usable. To combat charging, a thin layer (1-2 nm) of Pt is deposited on top of the PMMA layer. This provides a conductive channel to remove excessive charge and is thin enough to not disrupt the development of the underlying resist.

The lead material for the devices was initially based on Ti/Au multilayers. Generally Ti is a good adhesion layer for oxide materials but did not seem to adhere well to the GGG substrate. Near the wire the leads would often be torn and wire bonding to the pads was difficult. Imaging the leads after development reveals part of the problem. Figure 3.28 shows that the Pt layer on top of the PMMA sometimes does not break apart during the development process and falls down to the substrate. This then prevents adhesion of the leads. In initial testing of this process this was not an issue, but the process of Pt breaking up is likely very sensitive to the Pt thickness. Over time deposition rates in a sputtering system will vary slightly and it is likely the Pt layer is thicker than desired.

To try and account for any remaining Pt, the lead structure was changed to Al(4)/Pt(2)/Cu(15)/Pt(2). Aluminum was used for two reasons: First it alloys fairly aggressively with Pt. Second, it can substitute gallium in the GGG structure. The hope was that these properties would allow the Al layer to absorb any Pt on the surface and try then to bond to the GGG layer. The Pt layer adjacent to the Al layer was an attempt to stabilize the Al layer and prevent migration of Al into the Pt nanowire. The worry was that Al

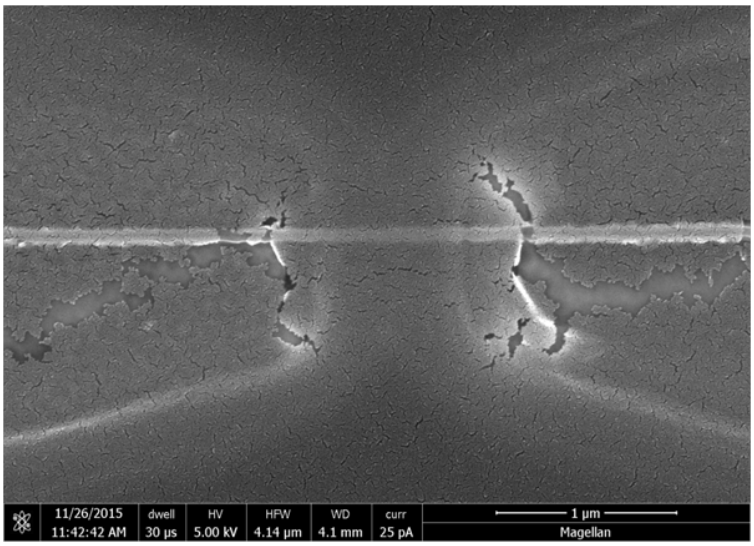

Figure 3.28: SEM image of the lead pattern after development showing a case where the Pt layer on top of the PMMA layer does not break apart.

impurities in the Pt layer could cause problems with the spin Hall angle. However, recently it has been presented that Al impurities in Pt actually can increase the spin hall angle [53].

After depositing the leads, the samples are soaked in acetone heated to 60 C for 45 minutes. This serves to dissolve the resist and in theory, only the regions that had been exposed will have material when the procedure is done. The adhesion of leads to GGG is generally poor, so lift off needs to be done carefully. To complete the leads the beaker containing the sample and acetone needs to be gently swirled. When it looks like the material has been lifted off, the sample can be removed from the acetone. It needs to be sprayed wit isopropyl alcohol immediately after removal from acetone or else residue will be left on the sample. Then before it dries, dry nitrogen should be used to remove any liquid.

Sometimes there can be problems with the lift off procedure where chips are left in the gap between the leads. Figure 3.29a shows an example of this during the testing of lead designs. In this case, the chip in the lead gap could not be removed with sonication. There is a method to remove it that can be risky and treated as a last effort to save a device. It involves submerging the sample in acetone, then carefully dragging a Q–tip across the

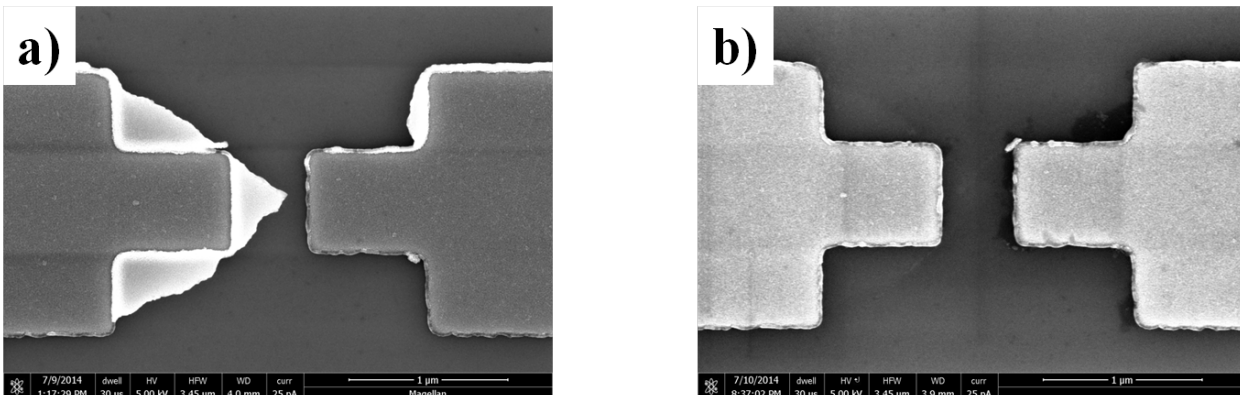

Figure 3.29: Leads before **a)** using a Q–tip and after **b)**.

sample surface. If the right amount of force is used, the chip can be removed as shown in Fig. 3.29b. However, too much force will damage the leads.

3.3.6 Completed Nanowire

After the leads are defined we are left with a completed device. Figure 3.30 shows two examples of completed devices. From the SEM images one would assume that the left wire would have better characteristics than the right one due to the large amount of leftover residue on the wire and slightly torn lead. Surprisingly, the left wire has an almost unintelligible behavior as seen by the ferromagnetic resonance measurement above it. The details of this type of measurement will be explained in the next section, but generally the presence of multiple peaks is bad for spin torque oscillators. In contrast, the ugly wire on the right has a relatively simple spectra and is the fully functioning spin torque oscillator that will be analyzed in the later chapter.

The large difference in behavior is likely due to the design of the nanowires. The left wire in Figure 3.30 was an early version that had a small amount of overlap between the leads and nanowire. This design lead to various problems. The first is the contact resistance from the leads to wire is high. Second, the spin wave spectra for this design is a mess. This

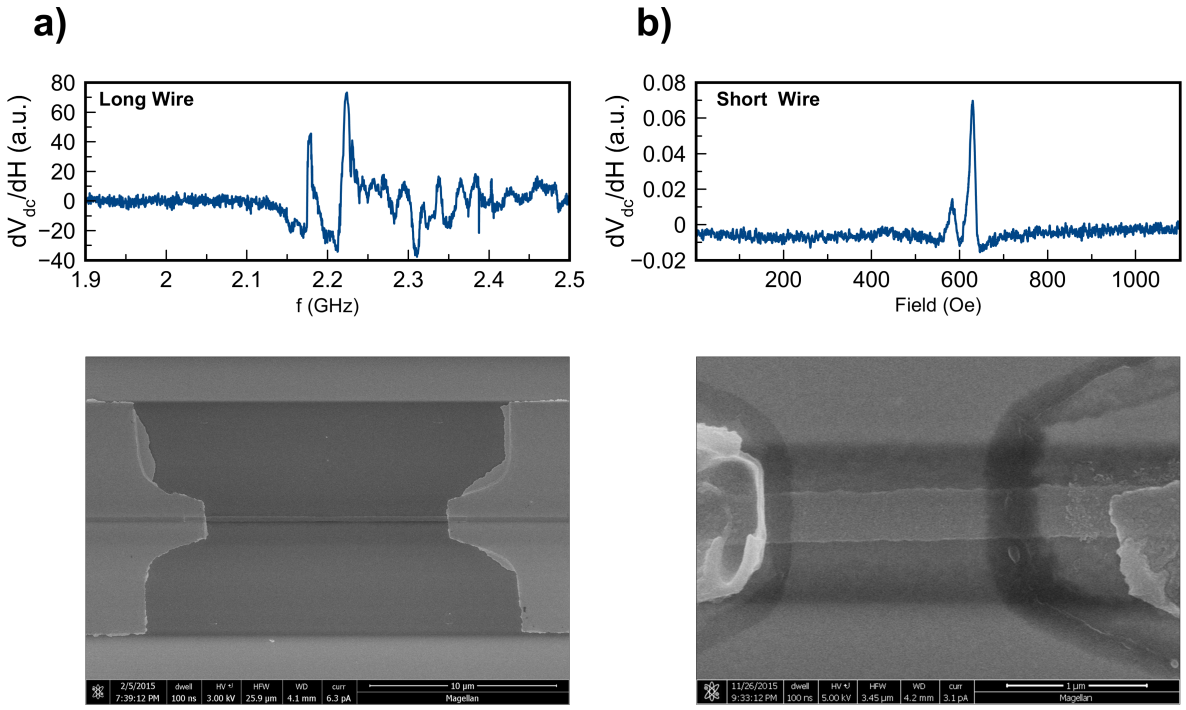

Figure 3.30: **a)** Nanowire with a bad spectra and image of the wire. **b)** Nanowire with a good spectra and image of the wire.

likely is due to the spin waves reflecting at the edges of the wire and returning back to the active region. The simple fix for both these issues is to increase the length of the wire under the leads and decrease the active region. The added overlap helps to decrease the contact resistance and any spin waves leaving the active region decay before hitting a reflection point at the edge of the wire. Also the smaller active region decreases the overall sample resistance and improves the impedance mismatch from 50 ohms.

3.3.7 Itemized Procedure

Film Preparation:

- Deposit Yttrium Iron Garnet on Gadolinium Gallium Garnet [50]

- Load into UCI sputtering chamber
- Argon clean surface at 40 percent power for 60 s
- Deposit Platinum at room temperature

Alignment Marks:

- Spin coat MMA followed by PMMA (see appendix)
- Using e-beam lithography, write array of alignment marks. Typically a write current of 3.2 nA is used with an area dose of 270 $\mu C/m^2$
- Develop for 45 seconds
- Sputter 30 nm of Tantalum
- Soak in acetone heated to 60 C for 45 minutes
- Sonicate briefly

Nanowire Definition:

- Spin coat MAN-2401 (see appendix)
- Using e-beam lithography, align nanowire to previously made alignment marks. Typical write current is 13 pA and area dose of 270 $\mu C/m^2$. Center to center distance and line spacing set to 1 nm
- Develop for 60 seconds in maD-525
- Etch in ion mill at 65 degrees. In our system Pt etches at 9 nm/min and YIG at 3.7 nm/min. Etch angle is typically 65 degrees with a 25% duty cycle.

- Oxygen plasma etch in Harrick O2 cleaner for 9 minutes at high power.

Lead Deposition:

- Spin coat MMA followed by PMMA (see appendix)
- Sputter coat 2 nm of Platinum
- Using e-beam lithography, align to previously made alignment marks. Typical write current for section closest to the wire is 13 pA and area dose of 270 $\mu C/m^2$. Center to center distance and line spacing set to 1 nm. Then for larger features the current is increased in steps to up to 3.2 nA.
- Develop for a minute shaking aggressively
- Sputter deposit lead material: Al(4)/Pt(2)/Cu(15)/Pt(2)
- Soak in acetone heated to 60 C for 45 minutes
- Swirl gently and use spray bottle of acetone for lift off

3.3.8 Alternate Procedure: "Quick and Dirty"

The procedure for STO fabrication described throughout this chapter is the proper way to make samples. Mainly the nonmagnetic leads not only serve to lower the sample resistance, it eliminates any signal from magnetic leads and allows for a simpler boundary condition between the main active region and the rest of the wire. However, this procedure can take a lot of time to complete and can be prone to failure. Sometimes the thin films used are in short supply, so failure is not an option. Other times quick turn around is needed for developing the multilayer stacks.

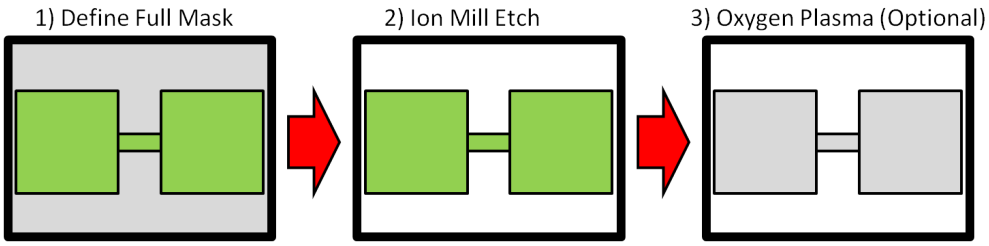

Figure 3.31: Alternate process flow for the fabrication of nanowires used in this study.

Figure 3.31 shows the general flow for this quicker procedure. In this method, the alignment marks are skipped since they are not needed. First, MAN-2401 resist is spun over the entire sample like in the full procedure. Rather than just writing the wire, the leads are written as well. After development the sample is then etched down to the substrate giving a complete device that can be used. The last step in the procedure is optional, and involves removal of any resist with oxygen plasma etching. If optical access to the sample is not needed, then this step is often skipped.

While this procedure is great for a quick turnaround, there are some other issues with it as well. Figure 3.32 shows a SEM image of a completed device. The pattern used is similar to that in Figure 3.31 but the actual device has a taper to it. This is a common issue with e-beam lithography, where the sections can bleed together. To avoid this the pattern must be drawn in a way where this is taken into account. However, this requires extensive testing and was not done for this sample.

So far most of the fab has been directed towards nanodevices built from films of GGG/YIG/Pt, but nanodevices made from GGG/Pt/YIG were studied as well. These reverse stack samples where prepared on substrates that were smaller than what was desirable. Typically for chips smaller than 10 mm by 10 mm the resists tend to not spin well. With any size chip, the resist beads up slightly at the edges. On small chips this causes the resist to be much thicker and the thickness is not uniform across the chip, leading to difficulties in fabrication. Whenever more issues like this are introduced, the probability of a full fabrication procedure

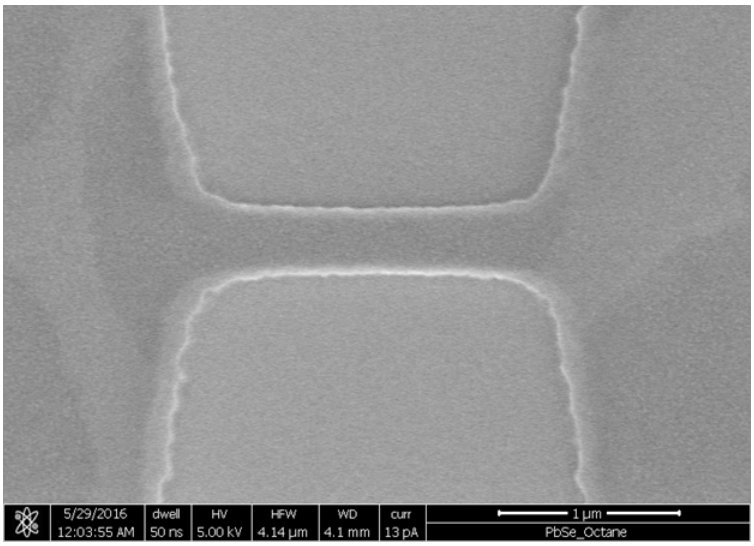

Figure 3.32: SEM image of the lead pattern after development showing a case where the Pt layer on top of the PMMA layer does not break apart.

failing increases quite a bit. This is where the single step method is desirable. If the first lithography step doesn't work right, acetone can be used to remove the MAN-2401 mask, allowing for a redo.

While the devices made from GGG/Pt/YIG films will not be discussed in detail here, Figure 3.33 shows the field dispersion measured by spin torque ferromagnetic resonance for a device made with this quick procedure. It shows that there is still a usable signal and not too many modes that arise from interactions between the leads and the active part of the wire where the current density is highest. Further studies [54] also have shown that these types of devices can enter auto-oscillations like the full procedure samples.

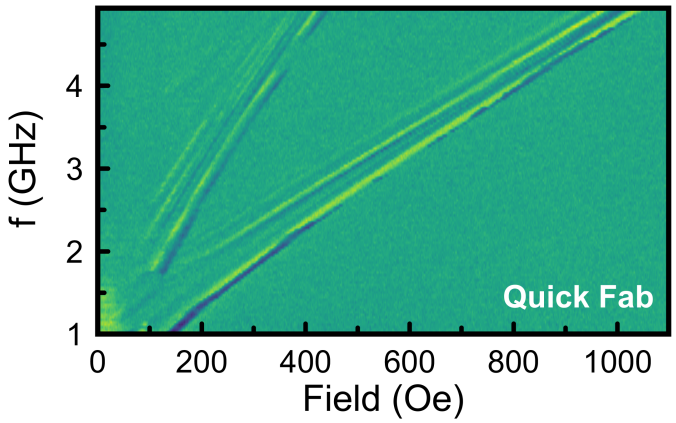

Figure 3.33: Alternate process flow for the fabrication of nanowires used in this study.

3.4 Ni/Co based Nanowires

3.4.1 Process Overview

The nanofabrication process of this chapter differs from the process used to create YIG/Pt based nanowires for a few reasons. One is for the original project goal, the nanowires needed to be made as thin as possible. This requirement made MAN-2401 not usable as a mask because it has relatively poor resolution and can not make well defined features much smaller than than around 100 nm. Instead, a 4% solution of Hydrogen silsesquioxane (HSQ) in MIBK is used, which is known for high resolution. When developed, it becomes similar to silicone oxide and therefore can not be easily removed. This requires a slight modification to the lead procedure.

The general process flow is as illustrated in Figure 3.34, with an itemized list available at the end of this section. After the full multilayer film is deposited, alignment marks are added as discussed earlier. HSQ is spun using the recipe in the Appendix and the wire mask is patterned using EBL. After this the first ion milling step is done. Instead of etching to the substrate, only the top ferromagnetic layers are etched away leaving a film of nonmagnetic

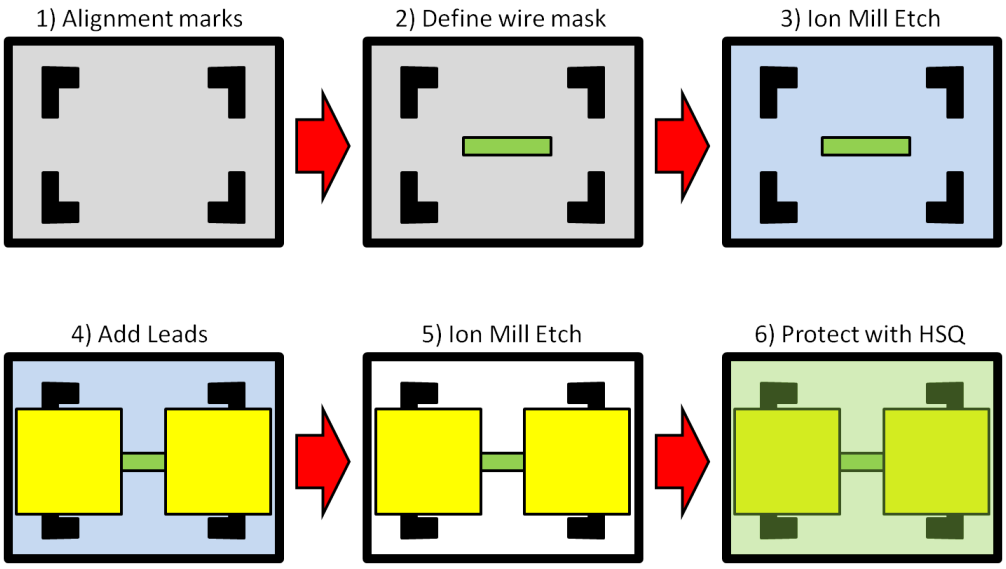

Figure 3.34: General process flow for the fabrication of nanowires used in this chapter.

metal still. The reason for this is to allow for a conductive path for the next EBL step of adding leads through a lift off procedure. Once this is done, a final etch fully defines the nanowire. Lastly, a layer of HSQ is spun over the chip to protect the nanowires from being oxidized by air and dissipate heat from the top of the nanowire when high currents are applied.

3.4.2 Film Deposition

The multilayers are deposited by magnetron sputtering on Al_2O_3 (0001) substrates in 2 mTorr Ar with a base pressure $\leq 3.0 \times 10^{-8}$ Torr. The film stacks consist of ferromagnetic metal (FM) and nonmagnetic metal (NM) layers and generally have either of the following structure types:

1. Al_2O_3 (0001)/Ta(3 nm)/NM/FM/Ta(4 nm)
2. Al_2O_3 (0001)/Ta(3 nm)/NM/FM/NM/Ta(4 nm)

Since the Ta(3 nm) seed layer and Ta(4 nm) capping layer are common to all structures, we refer to type 1 as NM/FM and type 2 as NM/FM/NM structures. The Ta seed layer is employed to promote growth of a smooth multilayer [55] and the Ta capping layer prevents the multilayer oxidation. The composite FM layer is a superlattice of exchange coupled Co and Ni layers: Co(0.85 nm)/Ni(1.28 nm)/Co(0.85 nm)/Ni(1.28 nm)/Co(0.85 nm). We have chosen the Co/Ni superlattice due to its large PHE and AMR [38] as well as its significant perpendicular magnetic anisotropy (PMA) [56, 57]. The thicknesses of the Co and Ni layers in the composite FM are chosen to nearly balance the easy plane magnetic shape anisotropy of the FM film by PMA in order to be able to saturate the FM magnetization in any direction by a small magnetic field. We employ Pt, Pd, and Au as the NM layers. In type 1 multilayers, we use NM = Pt(7.0 nm), Pd(8.0 nm), or Au(3.9 nm), with the NM thickness chosen to keep the NM layer sheet resistance nearly the same. For type 2 multilayer, we employ Au(2.5 nm) as the bottom NM material and Au(1.5 nm) as the top NM layer. The thickness of the top and bottom NM layers are chosen to be different in order to generate a non-zero microwave Oersted field applied to the FM magnetization in ST-FMR measurements, which strongly enhances the amplitude of the magnetic oscillations and the signal-to-noise ratio of the ST-FMR signal.

We employ a conventional broadband ferromagnetic resonance technique (FMR) to measure magnetic damping in the NM/FM and NM/FM/NM multilayer films in order to characterize spin pumping across the NM/FM interfaces and spin sink efficiencies of the NM layers. FMR measurements are carried out at room temperature using a broadband microwave generator, coplanar waveguide, and planar-doped detector diode. The measurements are performed at discrete frequencies in an in-plane field-swept, field-modulated configuration, as detailed in Ref. [58]. The measured FMR data are described by an admixture of the $\chi^{'}$ and $\chi^{''}$ components of the complex transverse magnetic susceptibility, $\chi = \chi^{'} + i\chi^{''}$. The FMR data are fit as described by Ref. [58, 59].

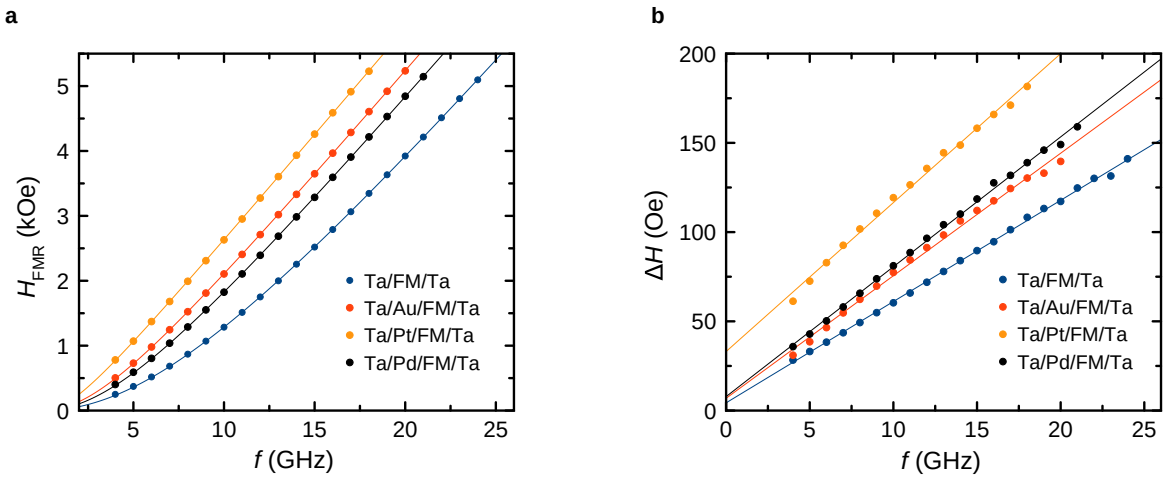

Figure 3.35: **a** Ferromagnetic resonance field as a function of frequency for films measured in the in-plane magnetic field configuration. **b** FMR linewidth ΔH as a function of frequency.

The samples studied are polycrystalline and show negligible in-plane anisotropy. The in-plane resonance condition is

$$\left(\frac{\omega}{\gamma}\right)^2 = (H_{\mathrm{FMR}})\,(H_{\mathrm{FMR}} + 4\pi M_{\mathrm{eff}})\,, \tag{3.1}$$

where $\omega = 2\pi f$ is the microwave angular frequency, H_{FMR} is the resonance field, $4\pi M_{\mathrm{eff}} = 4\pi M_{\mathrm{s}} - 2K_{\mathrm{U}}/M_{\mathrm{s}}$, and K_{U} is the perpendicular-to-film-plane uniaxial anisotropy. Figure 3.35a shows example data of H_{FMR} as a function of frequency. The data are fit using equation 3.1 to extract $4\pi M_{\mathrm{eff}}$ and g, which are tabulated in Table 3.1.

The measured FMR linewidth defined as half-width of the resonance curve is well described by Gilbert-like damping,

$$\Delta H(\omega) = \alpha\frac{\omega}{\gamma} + \Delta H(0), \tag{3.2}$$

where ω is the microwave angular frequency, and $\Delta H(0)$ is the zero-frequency line broadening due to long range magnetic inhomogeneity [60–62]. Figure 3.35b shows example data of ΔH

Table 3.1: Summary of film level magnetic properties determined by broadband ferromagnetic resonance. Numbers in parenthesis are layer thickness in nm. The composite ferromagnet is FM=$[Co(0.85)/Ni(1.28)]_2/Co(0.85)$.

Sample	$4\pi M_{\text{eff}}$ (Oe)	g	α (10^{-3})	$\Delta H(0)$ (Oe)
Ta(3.0)/FM/Ta(3.0)	7160	2.17	17.2	4
Ta(3.0)/Au(3.9)/FM/Ta(3.0)	3010	2.17	20.9	7
Ta(3.0)/Au(2.5)/FM/Au(1.5)/Ta(3.0)	3220	2.14	21.7	4
Ta(3.0)/Pt(7.0)/FM/Ta(3.0)	1480	2.17	25.3	33
Ta(3.0)/Pd(8.0)/FM/Ta(3.0)	4060	2.18	22.2	8

as a function of frequency. The data are fit using equation 3.2 to extract the parameters α and $\Delta H(0)$, which are tabulated in Table 3.1.

The values of α in Table 3.1 show that the Ta/FM/Ta sample has the lowest damping. This means that the spin pumping is smallest at the Ta/FM and FM/Ta interfaces [63–65]. Adding a Au insertion layer at the bottom Ta/FM interface, Ta/FM/Ta $\rightarrow$ Ta/Au/FM/Ta, shows a significant increase in the spin pumping induced damping. It is noteworthy that the thickness of Au(3.9 nm) is much less than the spin diffusion in Au (30-60 nm) suggesting that the Au/Ta bilayer acts as an efficient spin sink. Furthermore, adding another Au layer between the top FM/Ta interface shows further increase in spin pumping induced damping. This shows that the Au layer in the Au/Ta bilayer facilitates efficient spin transfer from the FM layer. The values of α in the Pt/FM and Pd/FM structures are high indicating that the Pt and Pd layers are efficient spin current sinks.

3.4.3 Nanowire Definition

In principle, the patterning of the nanowires using HSQ should have been a simple task, since the previous student working with HSQ had a stable procedure. However, HSQ is not an easy resist to work with and is known to have adhesion issues. Further, once spun there is about a two hour window where it can be used to make good resolution patterns. In the first attempts using the original procedure during the development step, all patterns regardless

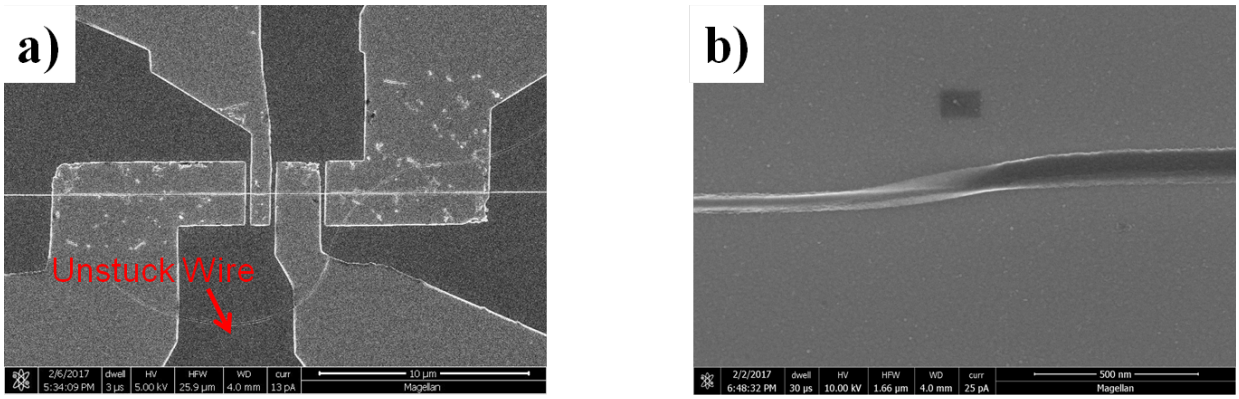

Figure 3.36: **a)** A HSQ nanowire that did not stick to the substrate during the first attempt of nanowire patterning. **b)** HSQ nanowire mask that fell over

of size would be ripped off the surface or shifted from their original location. Figure 3.36a shows a device where a wire that had become unstuck from the surface is still present on a completed device. Adhesion issues was a constant problem in the early stages of this project.

To improve the recipe, several things were tried. One key step that improved adhesion significantly was to perform a 60 s Argon etch in the sputtering system at 40 percent power just prior to spinning the HSQ onto the substrate. For all samples made, the spinning was done immediately after breaking vacuum. It is unclear if the timing is important or not, but since it worked, repeating these steps back to back was done to not waste time on the SEM.

Even with the surface cleaning, there were still some adhesion issues. When spun, the resist is around 100 nm thick and since we were trying to pattern sub 30 nm wires, the patterned resist can be geometrically unstable and would fall over. Figure 3.36b shows an example of this where on the left side the resist is standing up properly and on the right it has fallen over. On top of this, the wires getting ripped off during development was still an issue. At this point in the process development, it was possible to find wires that had just stared to rip off the surface and they revealed that they first came unstuck near the edges. The solution to this was to add anchoring pads at the end of the wires shown in Figure 3.37.

The last development with the process that greatly increased reliability was modifying the

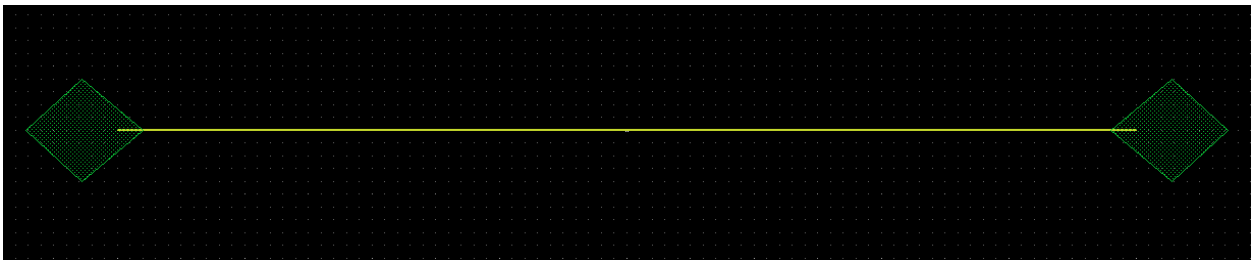

Figure 3.37: Pattern for the nanowire including anchors at the ends.

developer used and development procedure. The exposed HSQ was initially developed with a solution of 1 wt % NaOH and 4 wt % NaCl [66]. When the sample was first exposed to the developer, there was a quick formation of bubbles on the surface. The initial guess was that the development process was occurring too rapidly and aggressively, causing the undeveloped HSQ to pull the pattern off with it. Further diluting this solution with an equal volume of water and just increasing the development time seemed to greatly increase reliability. Also during the development step great care is taken to prevent agitation of the developer. The sample is placed in a beaker before the developer and then the developer is slowly poured in. Once the development time is up, the chip is slowly removed with tweezers and slowly placed in a beaker of HPLC water. Once this is done, the HSQ seems to remain stuck to the surface fairly well. After the chip is pulled from the water beaker, it needs to be sprayed down with HPLC water and immediately dried. I tend to try and keep the water stream from the bottle weak and I spray in a direction along the length to try and prevent knocking the wires off. If the final water spray is not done, there is a large amount of particles from the undeveloped HSQ left on the surface.

Now that the mask is defined, argon ion milling can be used to transfer it into the NM/FM multilayer stack. In this step, the etching time is calibrated such that only the FM layer is etched away. In these stacks the NM layer was always a Nobel metal, which meant oxidation was not an issue. Leaving the film present at this point greatly assists in the next step of adding electrical leads. First, it provides for a conducting layer that prevents charging artifacts in the EBL process. The sapphire substrates used are too insulating for this to not

be done. This approach was chosen over the method of depositing metal on top of the resist used in the previous chapter since it is a more reliable method. The second advantage is the metallic layer helps promote good lead adhesion and contact to the nanowire. Since the top HSQ layer can not be removed easily, this is important since all connections rely on side contact rather than contact to the top of the wire.

The first step in determining the needed etch time to stop in the NM layer is to determine the full stack etch time. Calibration of the etch time was done in a very low tech manner of just "eyeballing it" since the ion mill used was not equipped with a SIMS detector. Luckily, the sapphire substrates used are clear and even a few nanometers of the Ta seed layer can be seen by eye. A test chip is place in the ion mill such that it is placed over one of the clip holes. This seems to aid in visual identification of when the etch is complete. The test chip is then etched for an excessive time and the time until the chip appears clear through the view port is measured. Then using the typical etch rates for the NM layer, the final etching time is estimated.

For the samples made in this chapter, the ion mill duty cycle was set to 100%. The etch times for these samples are typically fairly short and precision for the etching time needs to be achieved. Since the shutter on the ion mill that controls the duty cycle requires a finite time to open and close, this introduces some variation in the actual etching time.

The angle between the ion mill beam and the substrate plane is an important parameter in the definition of the nanowire. Figure 3.38 illustrates the difference in the pattern transfer from the mask to the film for two different beam angles. At a low angle, the thickness of the mask blocks some of the beam resulting in a tapering of the thickness away from the mask. Since we want the wires to be as narrow as possible, this is not desirable to do. Further, we want to stop in the NM layer so the amount of material etched needs to be uniform. A high angle etch is then used since it decreases the amount of shadowing from the mask.

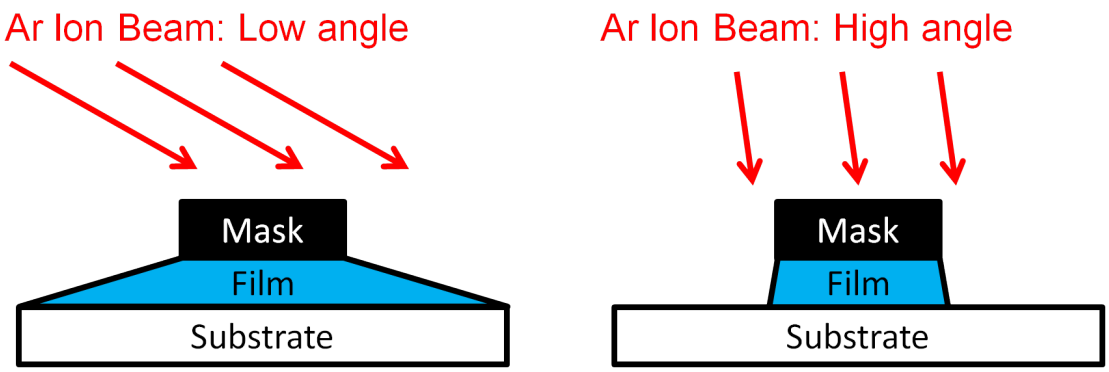

Figure 3.38: The resulting pattern transfer from ion milling at high and low angles.

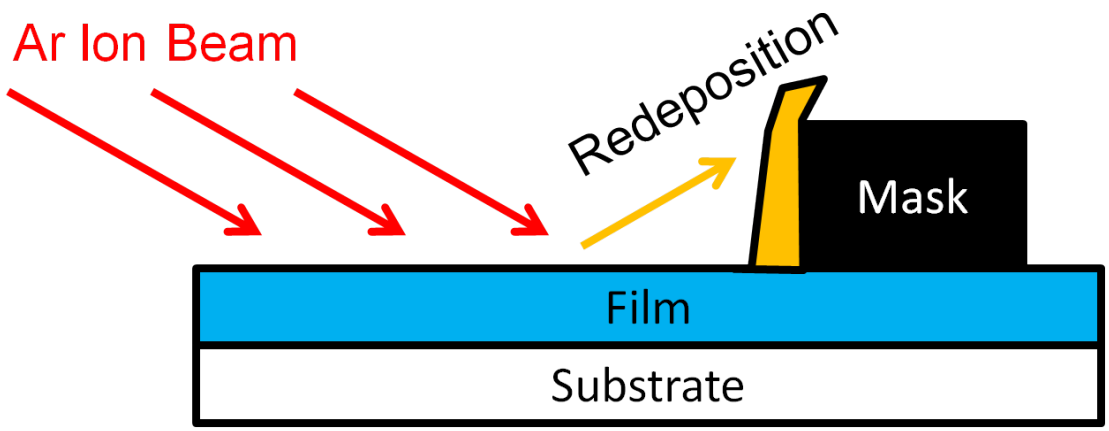

Figure 3.39: Illustration of how ion milling leads to material build up on the edge of the mask.

A high angle etch has some drawbacks. With any angle there is what as known as re-deposition, where material that is removed from the etched film adheres to the side of the mask as illustrated in Figure 3.39. This takes place because ion milling is a purely ballistic process. In the case of low angle etches, some of the ion beam is incident on the side of the mask and effectively cleans some of the re-deposition off as the milling is done. However, since a high angle etch (85 degrees) is done to define the wires, these sidewalls are not cleaned off as shown in Figure 3.40a appearing as the bright spots at the edge of the wire.

There was concern that these sidewalls could cause issues with device performance at low temperatures. They are made from the materials of the FM layer but their structure is

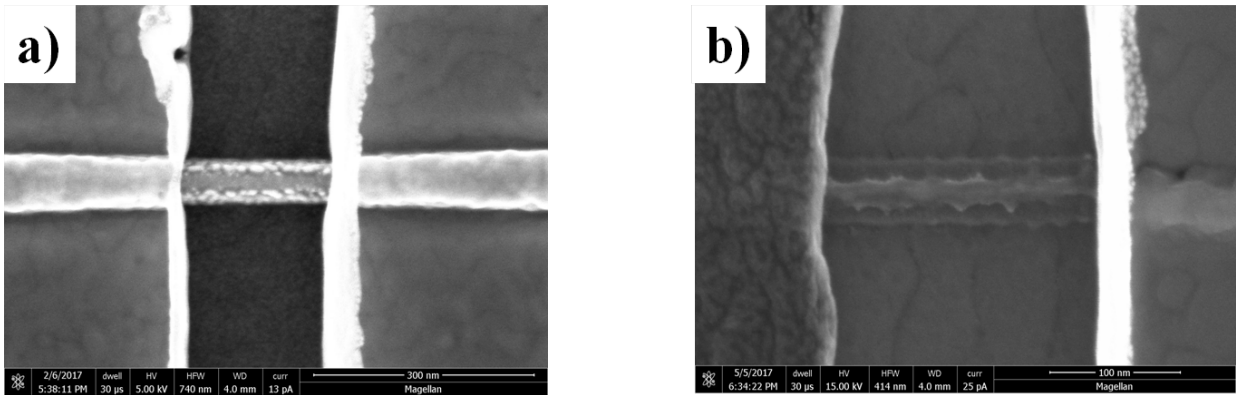

Figure 3.40: **a)** Nanowire with a large amount of re-deposition on the edges. **b)** Nanowire where the low angle etch was too long and damages the HSQ mask.

bound to be different than the main part of the film. Further, they extend up the mask and away form the edge of the nanowire. During the fabrication process it is inevitable that the samples are exposed to air and it is likely that these sidewalls become oxidized. The natural oxides of Ni and Co are both antiferromagnetic and can pin FM layers at low temperatures [67] leading to unpredictable behavior[51]. To remove these edges, a low angle etch (5 degrees) is performed to clean up the sidewalls. Here some care needs to be taken in the etch time. The HSQ mask etches relatively quickly and needs to remain intact for the final clean up etch. Figure 3.40b shows a case where the sidewall cleaning was too aggressive (2 min) and damaged the HSQ mask. Etching the sidewalls for around 45 seconds seemed to give the best results as shown in a completed device in Figure 3.41.

3.4.4 Nanowire Definition: Alternative Procedure

The procedure detailed in the previous section could reliably produce wires down to about 40 nm in width. However, there was a desire to push the nanowires to even narrower dimensions. An additional step in the etching process was introduced to effectively trim down the HSQ mask. In the previous section, a dose of about 7200 μC/cm^2 for a 30 nm wide pattern resulted in a nominally 40 nm wide nanowire. For the new approach, the dosage

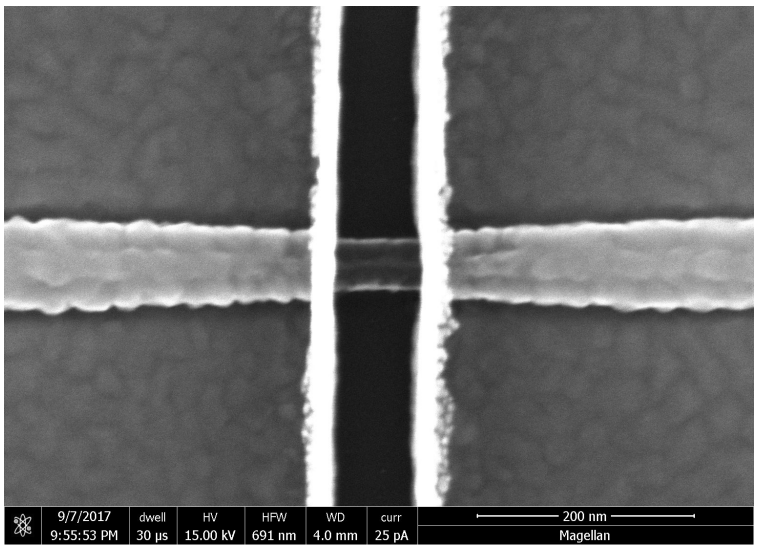

Figure 3.41: A good nanowire device.

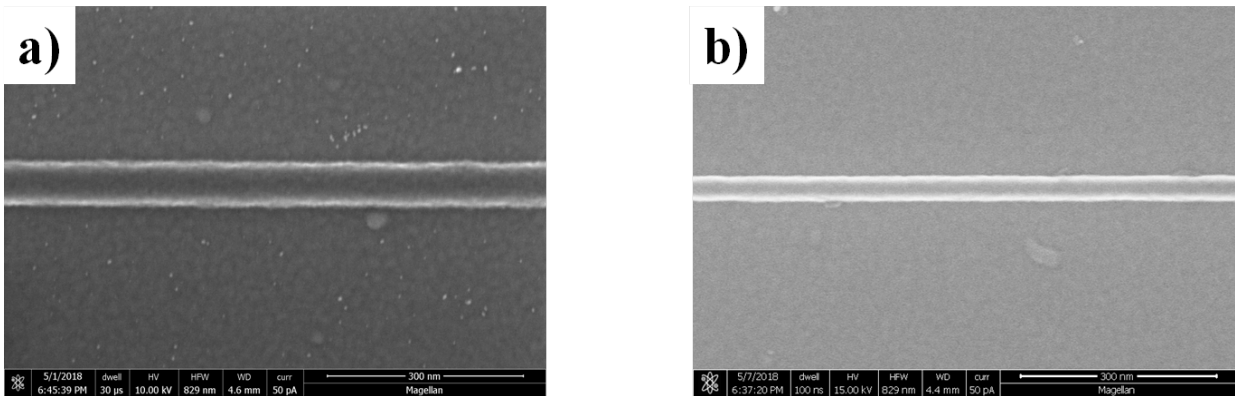

Figure 3.42: **a)** 63 nm wide HSQ mask after development. **b)** Same mask after 40 s etch in the ion mill at 5 degrees now trimmed down to 36 nm.

was increased significantly to 8100 μC/cm^{2}to produce a much wider wire mask with hopes that the increased surface area of the wire would increase adhesion. As seen in Fig 3.42a, the resulting mask is measured to be 63 nm. To achieve the desired dimensions, a low angle (5 degrees) etch is performed in the ion mill. Figure 3.42b shows the same mask after a 40 s etch and measures to 36 nm wide. Surprisingly, the edge roughness of the mask is not significantly increased.

While in the testing of this procedure only the low angle etch was done, in actual device fabrication this method is fairly easy to implement. In the software for the ion mill tool

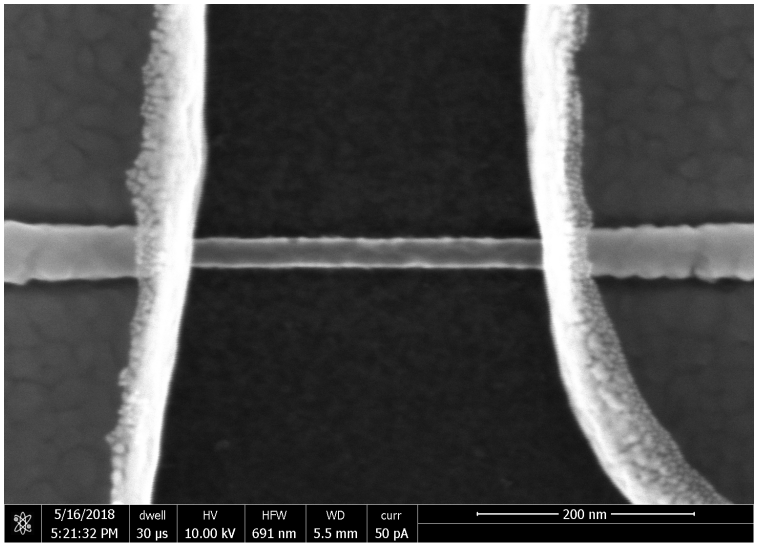

Figure 3.43: A 25 nm nanowire based device.

used, up to three sets of etching can be performed in a row. So in the actual transfer of the mask pattern into the film the low angle etch is performed first to trim the mask down. This is then immediately followed by the same high angle etch and sidewall cleaning described in the previous section. Figure 3.43 shows that with this procedure it is possible to make a 25 nm wide wire with increasing the etching time. Further increasing the etch time may be able to make narrower wires.

3.4.5 Lead Deposition

The lead deposition is done using a lift-off procedure with MMA/PMMA resists and for the various families of samples based on the Ni/Co multilayers, either consist of Nb(5 nm)/Au(nm)/Nb(5 nm) or Ta(5 nm)/Au(nm)/Ta(5 nm) depending what materials were present in the sputtering chamber. The Nb and Ta adhesion layers seem to stick fairly well to the various NM layers tried, in that even with light sonication during lift off they do not tear off. The top capping layers serve to protect the Au leads from the final clean up etch since Au etches rapidly.

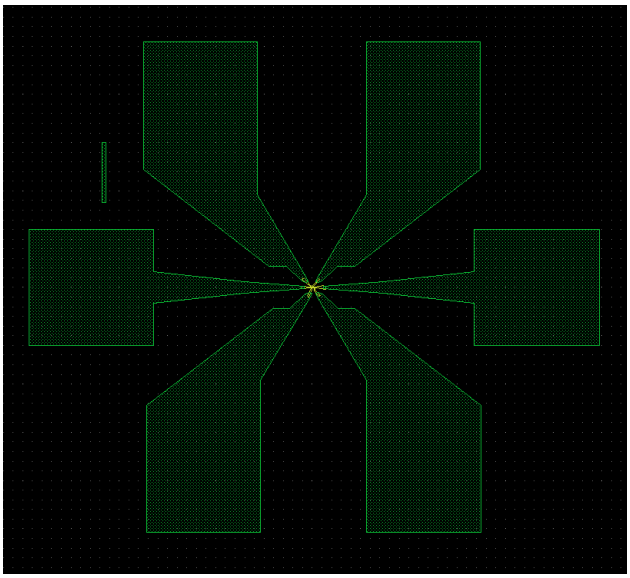

Figure 3.44: **a)** Leads with material left in them after development **b)** Leads without this material.

Figure 3.44 shows the lead design used and Fig. 3.45 shows SEM images of devices. The first thing to take note is there are more than two contacts. This allows for multiple devices to be made on the same wire and greatly increases the amount of samples that can be made. A large amount of time is saved with this design since a good part of the time spent in the EBL process is aligning the leads to an existing nanowire. Also in order to dice a batch of samples so they fit in the sample holders, There needs to be about 2 mm of separation between each device. This greatly increases the density of devices given this restraint.

The rectangle in the top left corner of the pads in Fig. 3.44 serves no functional purpose other than to be able to identify the orientation of the sample. Often in the dicing phase the sample gets flipped over and it is useful to have a visible indicator. Since each sample is imaged, it is important to keep track of what number each sample is.

One minor issue with the leads is the resist sometimes leaves material behind when developed. The bright randomly shaped spots in the leads in Fig. 3.44a are one example of this. It is not exactly clear what this material is, but it is likely undeveloped MMA or PMMA. It does not seem to affect device performance at least. The appearance of this material can be reduced

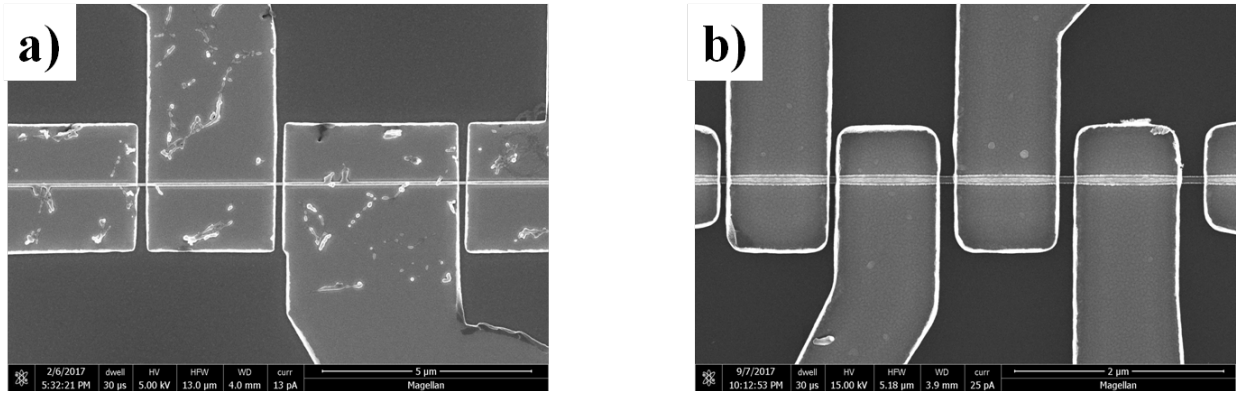

Figure 3.45: **a)** Leads with material left in them after development **b)** Leads without this material.

as shown in Figure 3.44b by increasing the dosage used in the EBL process and developing the resist a little longer for a 60 s. Here I do not give an exact dosage value because it varies depending on the size of the contact pad and is something that needs to be tested for a specific design.

3.4.6 Clean Up Etch

After the leads are deposited a final clean up etch needs to be performed in order to remove the remaining NM layer. This is done in the ion mill with a 80 degree etching angle for about a minute depending on the NM material. Generally there needs to be a bit of over-etching or else the leads shadow the regions of the wire near them. No low angle etch for sidewall cleaning is performed. The worry is that a low angle etch will knock over the sidewalls on the leads into the gap between them.

3.4.7 HSQ Protection

The very last step is to spin coat a layer of HSQ over the chip. This serves to protect the wire from oxidation over time. It also acts as a heat sink and helps with heat management of the

STO. Electrical connection to the leads can still be made when wire bonding the samples. Occasionally the first attempt at a connection will not stick, but usually this scratches off the HSQ allowing for the next connection to stick.

3.4.8 Itemized Procedure

Film Preparation:

- Deposit multilayer stack in sputtering system.

Alignment Marks:

- Spin coat MMA followed by PMMA using program 6 (500 rpm 5 s followed by 4000 rpm 45 s) (see appendix)
- Using e-beam lithography, write array of alignment marks. Typically a write current of 3.2 nA is used with an area dose of 270 $\mu C/m^2$
- Develop for 45 seconds
- Sputter 30 nm of Tantalum
- Soak in acetone heated to 60 C for 45 minutes
- Sonicate briefly

Nanowire Definition:

- RF clean surface in sputtering system at 40 percent power for 60 s
- Spin HSQ using program 5 (3600 rpm 60 s) (see appendix)

- Using e-beam lithography, align nanowire to previously made alignment marks. Typical write current is 13 pA and area dose of 7200 $\mu C/m^2$. Center to center distance and line spacing set to 1 nm
- Develop for 3 minutes in 0.5 wt % NaOH and 2.0 wt % NaCl solution.
- Etch in ion mill at 80 degrees, leaving behind the NM layer. Follow with 45 s etch at 5 degrees.

Lead Deposition:

- Spin coat MMA followed by PMMA using program 6 (500 rpm 5 s followed by 4000 rpm 45 s) (see appendix)
- Using e-beam lithography, align to previously made alignment marks. Typical write current for section closest to the wire is 13 pA and area dose of 270 $\mu C/m^2$. Center to center distance and line spacing set to 1 nm. Then for larger features the current is increased in steps to up to 6.4 nA.
- Develop for a minute shaking aggressively
- Sputter deposit lead material: Nb(5 nm)/Au(40 nm)/Nb(5 nm) or Ta(5 nm)/Au(40 nm)/Ta(5 nm)
- Soak in acetone heated to 60 C for 45 minutes
- Sonicate briefly and use spray bottle of acetone for lift off

Clean Up

- Etch in ion mill at 80 degrees down to substrate.
- Spin HSQ to serve as protection from oxidation.

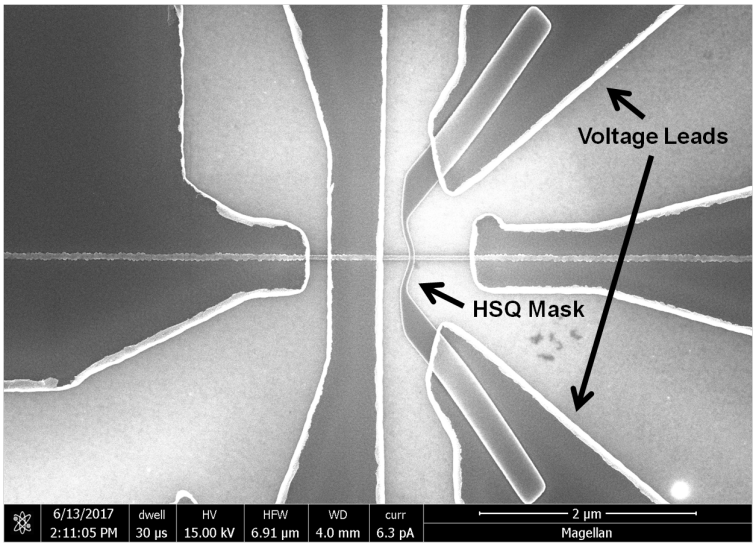

Figure 3.46: Device with additional HSQ mask for voltage leads.

3.4.9 Additional Step for Voltage Sensing

There was also some interest in looking at non–local signals in these devices. To sense them, the anomalous Hall effect was proposed which required the addition of two contacts to the side of the wire for sensing voltage. Since the wires are fairly narrow, gold leads could not be laid directly to the edges of the wire easily. To add these leads, an additional step was added between steps 3 and 4 shown in Fig. 3.34. After the first etching step, a mask of HSQ is deposited with a strip going completely of the wire. This serves to protect that region of Pt from the final etch. Leads are then laid over the HSQ mask. Since the leads are wider than the mask, electrical connection can be established through the remaining Pt. This procedure gives the completed device shown in Fig. 3.46.

3.4.10 Over-etched Samples

Stopping the first etching step in the NM layer can sometimes be difficult in the case where the NM is gold since the gold etching rate is relatively fast. If the sample is etched to the sapphire substrate, the EBL step for writing the leads can not be done since the substrate is

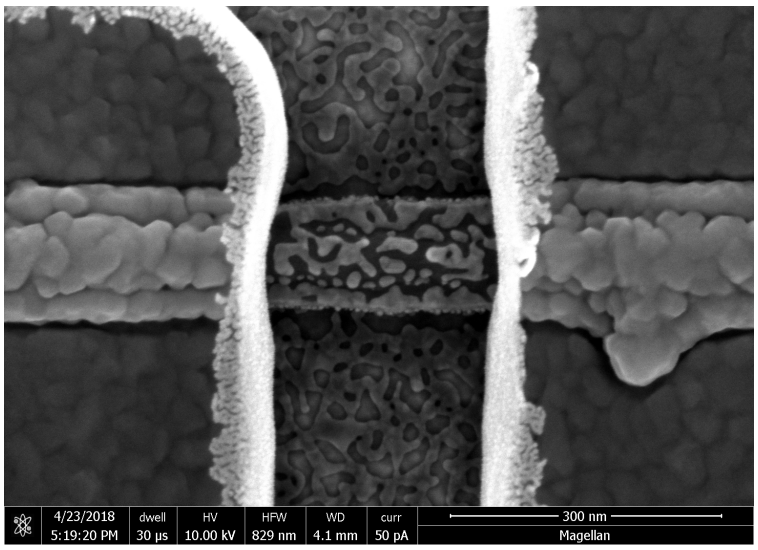

Figure 3.47: Device with gold deposited to prevent charging.

too insulating and charging effects distort the write pattern. However, there is a way to save the samples and not waste the time invested. To do so, 3 nm of gold is sputter deposited onto the substrate. This is sufficient to prevent charging and complete the EBL writing.

Before deposition of the leads, the gold layer needs to be removed since gold does not adhere well to the sapphire substrate without an adhesion layer. Any leads deposited on top of this layer will likely rip off during the lift off step. The gold layer was removed just before deposition using the stage bias in the sputtering system. Etching for 60 s at 90 % seemed to be enough to ensure good lead adhesion. Figure 3.47 shows a sample just after the leads are deposited demonstrating this. Since the etch in the sputtering system only removes gold where the leads are going to be, there is still gold over the rest of the sample as seen in Fig. 3.47 as the non-continuous brighter spots. To remove this, a clean up etch is performed in the ion mill.

3.5 Passivated Ni/Com Nanowires

One of the big issues with the fabrication procedure used in the previous section is that the etched ferromagnetic layer gets exposed to atmosphere. Although care is taken to keep the samples in vacuum as much as possible, this is inevitable. Exposure to oxygen results in the formation of magnetic oxide materials at the edge of the nanowire. Many of these oxides become anti-ferromagnetic at low temperatures and can result in altering the properties of the ferromagnetic layer[51]. This is undesirable for device performance.

To prevent edge oxidation, an e-beam evaporator inside the ion mill chamber is used. This section will outline a procedure based off of the previous section for making samples that never see oxygen. However, at the time of writing this there has not been sufficient time to perform a proper optimization of the procedure. The samples made here work, but there is room for improvement. Figure 3.48 shows the general procedure with an itemized list available at the end of this section. Since the procedure is similar to that of the previous section, only the additional steps will be discussed here.

The first major new step takes place after the nanowire definition in Fig. 3.48 step 3. Immediately after etching, the e-beam evaporator inside the ion mill chamber is used to deposit 10 nm of silicone oxide. The deposition is performed at 45 degrees to the sample normal to ensure that the edge of the nanowire is coated.

Next, using e-beam lithography the mask for the electrical leads is defined. After development, the sample is placed into the ion mill. Since the chip is coated with silicon oxide, it is not possible to make electrical contact to the nanowire at this point. A etch at 80 degrees is performed to remove silicon oxide in the exposed region where the leads will be placed. The angle used here is likely not optimal and will need some testing. Reason being an etch too close to the sample normal will not remove the silicon oxide from the edge of the nanowire. If the etch is too shallow, the ion beam can be shadowed by the resist mask. Further, excessive

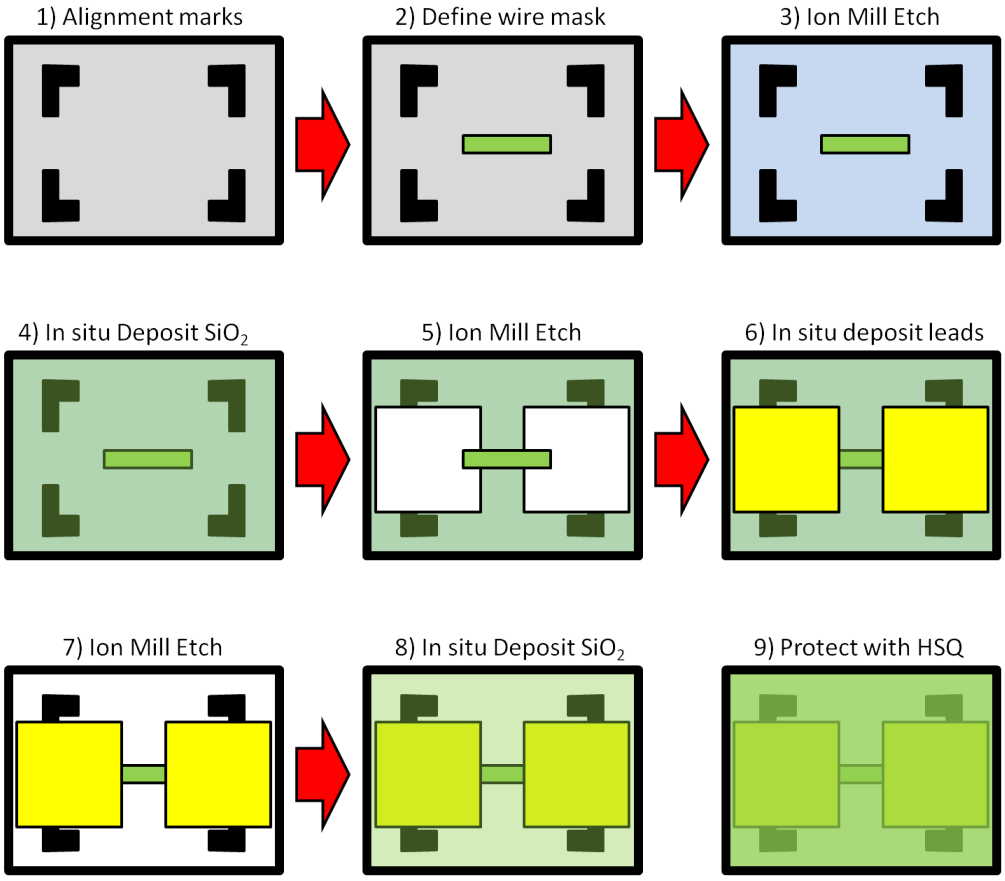

Figure 3.48: General process flow for the fabrication of passivated nanowires used in this chapter.

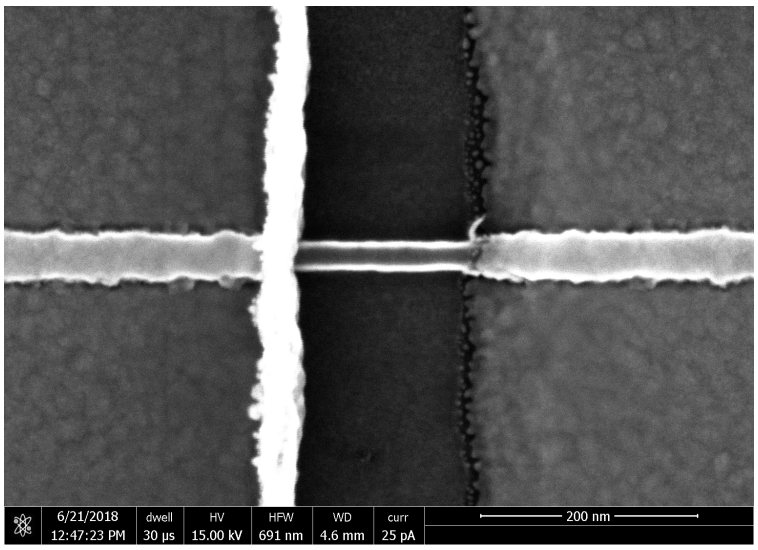

Figure 3.49: Passivated nanowire device.

etching of the edge of the nanowire may damage the ferromagnetic materials.

Once the etch is completed, Ti/Au/AlOx leads are deposited in situ. The material deposited should protect the wire from oxygen. The AlOx layer serves to protect the gold leads from the final etch. In future versions of the devices, this layer will likely be replaced with chromium since chromium conducts electricity.

The final modification to the procedure takes place in Fig. 3.48 step 8. After the final clean up etch, 10 nm of silicon oxide is deposited at 45 degrees to protect the nanowire edges. After that, HSQ is spun again to further protect the sample.

Figure 3.49 shows a sample made using this procedure imaged after step 6. The nanowire in the center measures to 28 nm in width from the widest part of the wire. The edges of the nanowire show the presence of some material indicated by the bright spots which in theory, should be silicon oxide. However, it is difficult to say for sure without further development of the fabrication procedure. If this is silicon oxide, the wire in reality is much narrower at about 16 nm.

3.5.1 Itemized Procedure

Film Preparation:

- Deposit multilayer stack in sputtering system.

Alignment Marks:

- Spin coat MMA followed by PMMA using program 6 (500 rpm 5 s followed by 4000 rpm 45 s) (see appendix)
- Using e-beam lithography, write array of alignment marks. Typically a write current of 3.2 nA is used with an area dose of 270 $\mu C/m^2$
- Develop for 45 seconds
- Sputter 30 nm of Tantalum
- Soak in acetone heated to 60 C for 45 minutes
- Sonicate briefly

Nanowire Definition:

- RF clean surface in sputtering system at 40 percent power for 60 s
- Spin HSQ using program 5 (3600 rpm 60 s) (see appendix)
- Using e-beam lithography, align nanowire to previously made alignment marks. Typical write current is 13 pA and area dose of 7200 $\mu C/m^2$. Center to center distance and line spacing set to 1 nm

- Develop for 3 minutes in 0.5 wt % NaOH and 2.0 wt % NaCl solution.
- Etch in ion mill at 80 degrees, leaving behind the NM layer. Follow with 45 s etch at 5 degrees.
- In situ deposit 10 nm of silicon oxide at 45 degrees to normal

Lead Deposition:

- Spin coat MMA followed by PMMA using program 6 (500 rpm 5 s followed by 4000 rpm 45 s) (see appendix)
- Using e-beam lithography, align to previously made alignment marks. Typical write current for section closest to the wire is 13 pA and area dose of 270 $\mu C/m^2$. Center to center distance and line spacing set to 1 nm. Then for larger features the current is increased in steps to up to 6.4 nA.
- Develop for a minute shaking aggressively
- Ion mll etch at 80 degrees for sufficient time to remove silicon oxide.
- In situ deposit lead material with e-beam evaporator: Ti(3 nm)/Au(30 nm)/ AlOx(14 nm)
- Soak in acetone heated to 60 C for 45 minutes
- Sonicate briefly and use spray bottle of acetone for lift off

Clean Up

- Etch in ion mill at 80 degrees down to substrate.
- In situ deposit 10 nm of silicon oxide at 45 degrees to normal
- Spin HSQ to serve as protection from oxidation.

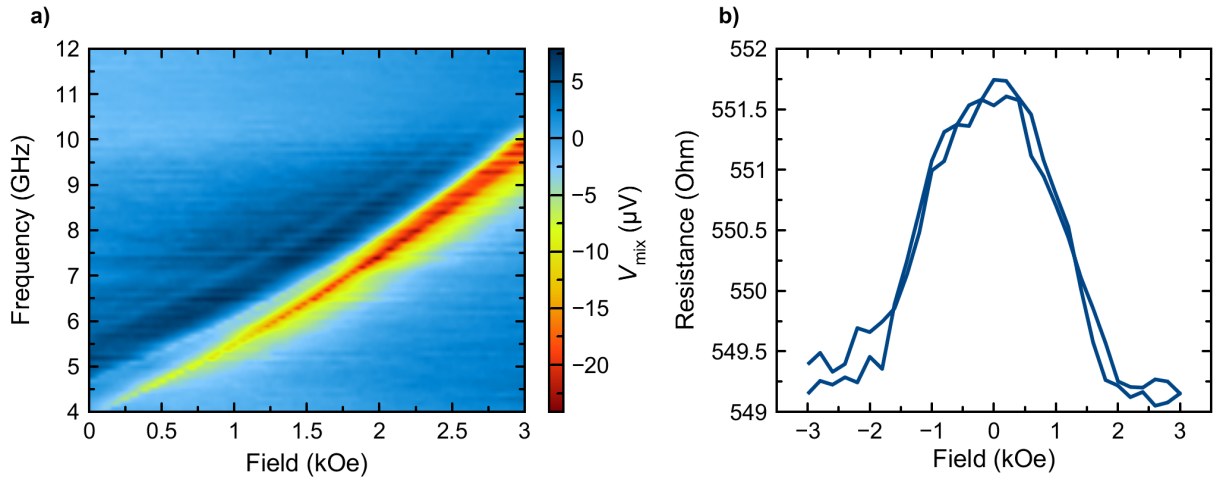

Figure 3.50: **a)** ST-FMR field dispersion for the passivated nanowire. **b)** Magnetoresistance for the passivated nanowire.

3.5.2 Sample Characteristics

Figure 3.50 shows some measurements on the nanowire pictured in Fig. 3.49. The nanowire is based of a Pt/NiCo multilayer stact similar to that discussed in the chapter "Planar Hall Torque." Figure 3.50a shows the ST-FMR measured field dispersion with magnetic field applied 60 degrees from the wire axis in the substrate plane. Compared to the samples described later in the chapter entitled "Role of Disorder in Ni/Co Nanowires," there are few modes seen in the plot. This indicates that the combination of the narrower dimensions and edge protection brings the samples closer to the theoretical behavior described in that chapter.

The fabrication on these samples was not completely successful though. Figure 3.50b shows the magnetoresistance for the wire measured with field applied perpendicular to the wire in the sample plane. The resistance saturates around 2 kOe which is consistent with the shape anisotropy induced by the narrow nanowire dimensions. However, the magnetoresistance percentage is low for these types of samples and the resistance measurements are noisier than normal. Further, when the sample is cooled the resistance of the sample increased which is not typical for these devices or metals in general. It is likely that there is a thin

layer of silicon oxide between the leads and the nanowire leading to a high contact resistance. More testing of the etching angles will be needed to determine if this is the issue or not and how to fix the problem. However, the ability to create samples with this procedure with almost no time spent in process development shows that this procedure holds promise for the fabrication of high quality nanowire devices.

Chapter 4

Spin Calortronic Nano-oscillator

Energy loss from Ohmic heating is a bottleneck limiting the speed and scale down of electronics. There is potential to harvest this heat and convert it into spin currents using the spin Seebeck effect. In this chapter, a spin torque oscillator based on platinum and yttrium iron garnet (YIG) is discussed. YIG is an insulating ferrimagnet with relatively low damping. Due to its poor thermal conductivity, a large thermal gradient can be sustained across the thickness of the material. This produces a spin current through the spin Seebeck effect[30–33] that exerts a torque on the YIG layer[34]. When a high enough thermal gradient is reached, auto-oscillations of the magnetization begin leading to coherent microwave emission.

4.1 DC Measurements

The first measurement to consider is the resistance as a function of external applied field. Since the emission of microwave power depends on the combination of the applied DC current and the microwave frequency resistance oscillations, it is important to verify a measurable resistance change. Figure 4.1a shows the resistance as a function of applied field perpen-

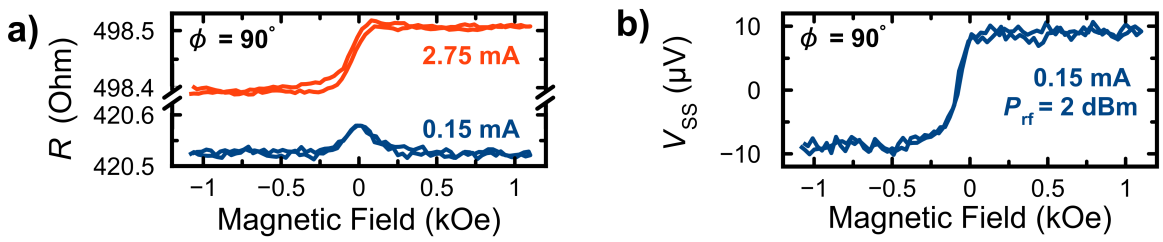

Figure 4.1: **a)** Magnetoresistance R of the YIG/Pt nanowire measured at low ($I_{\mathrm{dc}} = 0.15\,\mathrm{mA}$) and high ($I_{\mathrm{dc}} = 2.75\,\mathrm{mA}$) direct current bias for a magnetic field applied in the sample plane at the field angle $\phi = 90°$ with respect to the wire axis. **b)** Spin Seebeck voltage V_{SS} induced in the nanowire by a large microwave current (microwave power $P_{\mathrm{rf}} = 2\,\mathrm{dBm}$) as a function of magnetic field.

dicular the nanowire. Due to the shape anisotropy introduced by the nanowire geometry, a hard axis is created perpendicular to the wire and easy along it. The magnetoresistance curves reflect this in that the hard axis requires a larger field to saturate. The sign of the magnetoresistance is consistent with spin Hall magnetoresistance [20] and gives a MR of about .01 percent. Its presence is the first indicator that spin current can be injected into the YIG layer.

The next set of measurements deal with the magnetoresistance measured when a high DC bias is applied. The current required to create a spin torque oscillator is on the order of $10^{11}\,\mathrm{A/m^2}$, which in a nanoscale structure can cause a large amount of Ohmic heating. When the resistance is measured perpendicular to the wire at high bias, the data seen in Fig. 4.1a is quite different than the low bias case. We see a large offset voltage that depends on the direction of the magnetization. This offset is a direct result of the Ohmic heating present in the Pt layer of the nanowire. Since YIG is an insulator, it can not dissipate the heat produced, leading to a thermal gradient along the thickness of the YIG. When such a gradient is present, a spin current will be generated due to the spin Seebeck effect [16, 30, 68]. The polarization of this spin current is always collinear with the magnetization and when injected into the Pt layer, creates a electric field perpendicular to the polarization direction through the inverse spin Hall effect. The projection of this field on to the leads results in

the step seen.

The signal at high bias is not an artifact of the spin Hall current. If we again use a low direct bias but add microwave current at a high power, we again see this offset in Fig. 4.1b. In this case the sample is heated by the applied microwave and shows that this is thermal in nature.

4.2 Heating Simulation

In order to estimate the magnitude of thermal gradients arising from Ohmic heating, we carry out finite element simulations of coupled electrical and thermal transport in the YIG/Pt nanowire devices using COMSOL Multiphysics package [69]. We employ a fully realistic three-dimensional nanowire device geometry in these simulations. The device consists of a 350 nm wide 15 μm long YIG(23 nm)/Pt(8 nm) nanowire with two Al(4 nm)/Pt(2 nm)/Cu(15 nm)/Pt(2 nm) electrical leads attached to the wire ends. The leads are separated by a 2.5 μm gap that defines the active region of the nanowire STO device.

Once the geometry is defined, a mesh around all of the simulated regions needs to be created as shown in Figure 4.2. The size of this mesh is important since it determines the resolution of the solution. Further, if the mesh is much larger than the spatial variations of a solution, the solver will struggle to find a solution. The drawback of just always using a fine mesh is that as the number of mesh elements increases the amount of memory and processing power needed increases as well. One potential compromise that can be made is defining different meshes in different regions of the simulation. Also playing with the aspect ratio of the mesh can help with cases like that of a thin film where the thickness is much less than the width.

In these simulations, we used the temperature-dependent heat conductivities and heat ca-

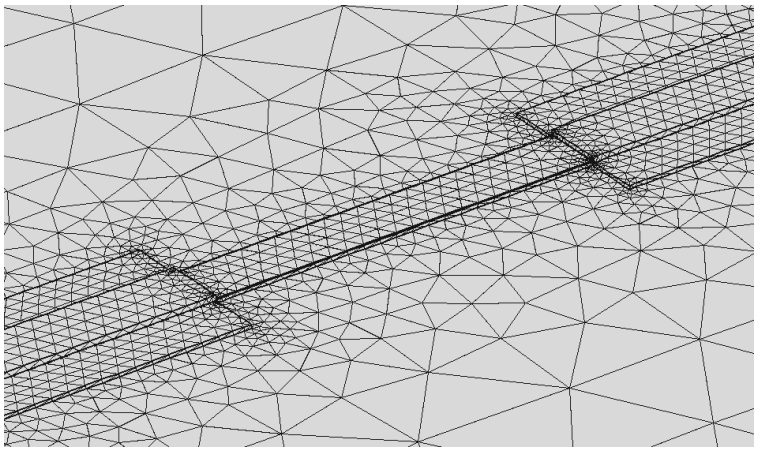

Figure 4.2: Example of the meshing done by Comsol in the heating simulations.

pacities of YIG and GGG as reported in Ref. [70]. The Pt layer resistivity in our YIG(23 nm)/Pt(8 nm) nanowire devices was measured in the temperature range from 140 K to 300 K and found to be linear as expected: $\rho(T) = \rho_0(1 + \alpha T)$ with $\rho_0 = 3.35 \times 10^{-7}\Omega\cdot$m and $\alpha = 1.59 \times 10^{-3}\mathrm{K}^{-1}$, which is similar to previously reported values in thin Pt films [71, 72]. The temperature-dependent heat capacity of Pt reported in Ref. [73] was employed in the simulations, and the thermal conductivity of the Pt layer was calculated from its electrical conductivity via the Wiedemann-Franz law. Literature values of the thermal and electrical conductivity and heat capacity of the lead materials were employed [69].

To perform the simulation, COMSOL needs to be told what physics package to use. The "Joule Heating" package works well for the simulation of Ohmic heating. Electric terminals can be defined at the ends of the simulated structures and the program calculates the current distribution based off of the defined resistivities. It then takes the material properties defined earlier and calculates the flow of heat from the nanowire. The result is a calculation of the full spatial distribution of temperature.

Figure 4.3a shows the calculated spatial distribution of temperature in the YIG/Pt nanowire device studied in this work at the bath temperature of 140 K and direct current bias $I_{\mathrm{dc}} =$ 2.5 mA that is similar to the critical current. Figures 4.4a and 4.4b show the depth profiles

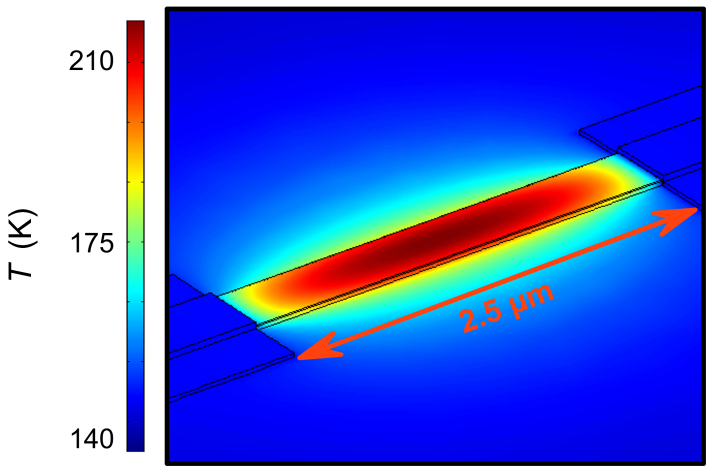

Figure 4.3: Temperature of the Pt/YIG nanowire determined from Comsol.

of the temperature in the center of the YIG/Pt wire. These figures reveal that the Pt layer temperature rises to 220 K. The temperature in the YIG layer rapidly decreases with depth resulting in a large temperature gradient $\nabla T = 0.26\,\mathrm{K\,nm^{-1}}$ across the YIG layer thickness. This high degree of Ohmic heating and the large value of ∇T result from the high resistivity of the Pt layer and efficient heat channeling into the YIG underlayer in the nanowire geometry employed in our experiment. In this geometry, the metallic leads do not function as efficient heat sinks because their overlap area with the nanowire is relatively small, which results in a high degree of Ohmic heating of the Pt nanowire and dissipation of this heat is mainly through the GGG/YIG underlayers. The quasi-one-dimensional nature of the Pt nanowire heat source and the three-dimensional character of the heat flow in the GGG substrate further enhance ∇T across the thickness of the YIG layer.

The validity of these COMSOL simulations can be directly checked against the experiment because the temperature of the Pt wire can be determined by measuring its resistance. Figure 4.5 shows the resistance of the Pt nanowire measured as a function of direct current bias. These data and the linear relation between the Pt nanowire resistance and temperature reveal that the Pt nanowire temperature at the bath temperature of 140 K and $I_{\mathrm{dc}} = 2.5\,\mathrm{mA}$

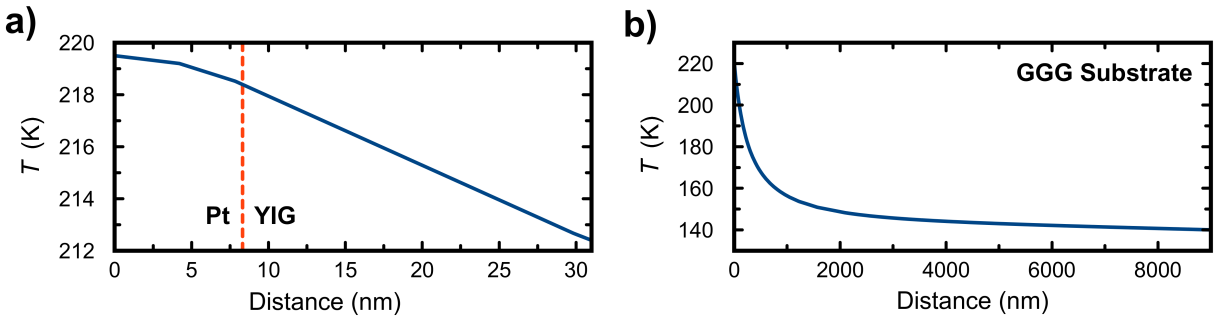

Figure 4.4: **a)** Temperature depth profile in the center of the nanowire. **b)** Temperature depth profile within the GGG substrate under the nanowire center.

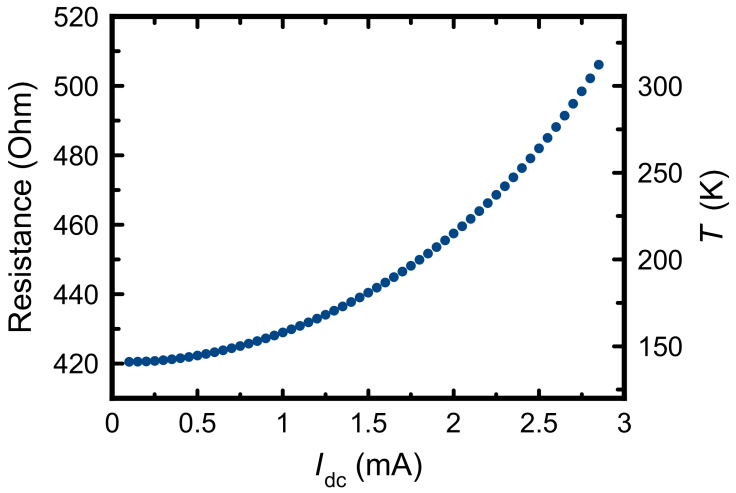

Figure 4.5: Pt nanowire resistance as a function of direct current bias. The right ordinate axis shows the corresponding wire temperature that was obtained from measurements of the wire resistance as a function of bath temperature at small bias current.

is 260 K. We therefore conclude that the COMSOL simulations underestimate the degree of Ohmic heating of the Pt wire and that the actual temperature gradient across the YIG film thickness is likely to exceed that predicted by the simulations.

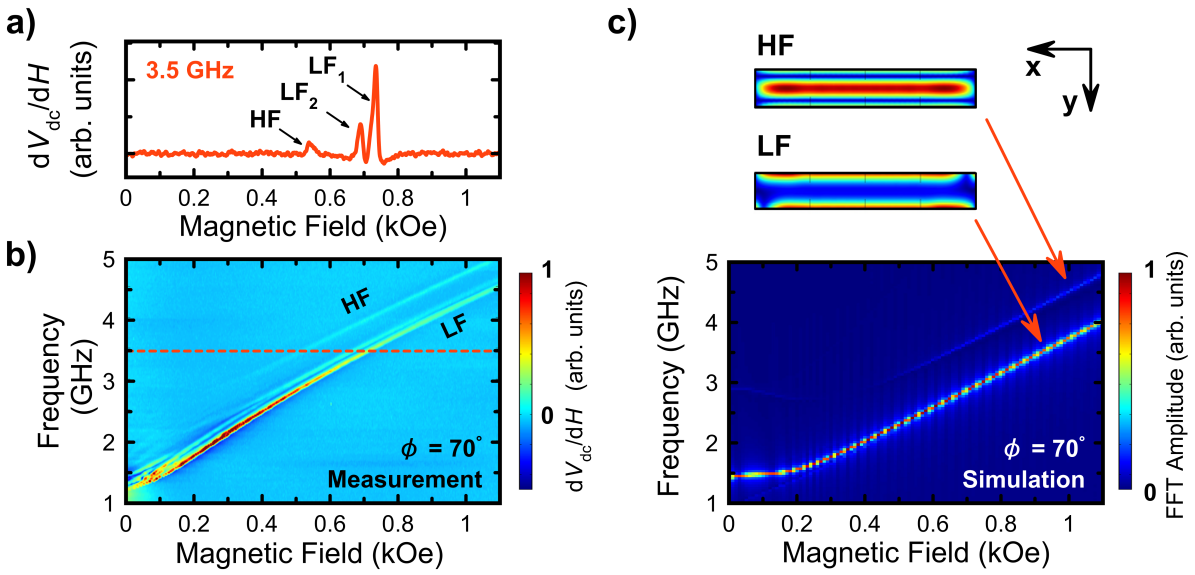

Figure 4.6: **a)** A single spin-torque ferromagnetic resonance spectrum measured at a microwave frequency $f = 3.5\,\mathrm{GHz}$ and magnetic field angle $\phi = 70°$. Low frequency (LF) and high frequency (HF) modes are observed. **b)** ST-FMR spectra of the YIG/Pt nanowire measured as a function of magnetic field and drive frequency at the field angle $\phi = 70°$. **c)** Micromagnetic simulation of the spin wave eigenmode spectra in the YIG/Pt nanowire with a top view of the spatial dependence of the LF and HF mode amplitudes.

4.3 Spin Torque Ferromagnetic Resonance

Figure 4.6a shows a single ST-FMR trace taken with the full field dispersion seen in Fig. 4.6b. There are two main branches of modes which are typical for this geometry due to the effective field at the edges of a nanowire being less than the bulk [74]. This leads to two main types of oscillatory modes, one localized at the edges of the wire and another at the center[75]. To confirm this, we perform micromagnetic simulations in MuMax3 to obtain the field dispersion in Fig. 4.6c with the simulated mode profiles. We see good qualitative agreement between the measurement and simulation.

In Figure 4.7a, the behavior of the main mode at $\phi = 65°$ as a function of applied DC current is shown. The resonance field increases as $I_{\mathrm{dc}}^{\sim 2}$ indicating Ohmic heating and the corresponding magnetization decrease. The amplitude of the FMR signal increases with

increasing DC current, but abruptly drops at 1.8 mA. The signal reappears at 2.2 mA with a much stronger amplitude.

In a typical NM/FM bilayer, one would expect the linewidth of the main mode to vary linearly current if the sole source of spin current is the spin Hall effect. In Fig. 4.7b, we see that for positive currents at this applied field angle a linear decrease in linewidth. However, for negative currents we see very little change in linewidth.

Further deviations from the expected behavior for a FM modified by spin current can be seen when we rotate the magnetic field closer to the axis of the wire. In this configuration the effect of the spin current from the spin Hall effect should be minimal and result in little change to the measured linewidth. However, what we observe in Fig. 4.7c is a decrease in linewidth for both polarity of bias.

This finding cannot be explained by solely spin Hall effect and requires consideration of the thermal spin current seen in the magnetoresistance measurements. Since these thermal currents are produced by Ohmic heating, they do not depend on the polarity of the applied bias. Further, only the Pt layer is heated and for this direction of thermal gradient, the thermal spin current exerts an anti-damping torque on the magnetization [35, 36], This explains the linewidth data described earlier. When the magnetic field is along the wire, only thermal currents can tune the damping, resulting in a symmetric decrease in linewidth with bias. On the other hand when field is perpendicular to the wire, both spin Hall and spin Seebeck currents contribute causing a deviation from the expected linear behavior.

We can further test the effect of Ohmic heating by varying the microwave drive power to heat the sample. In Fig. 4.7d we see that the linewidth decreases with increasing power, consistent with the expected result of increased Ohmic heating. While the linewidth is known to vary with microwave drive power, it tends to broaden with increased power [42].

The linewidth can be temperature dependent due to variations in material properties. To

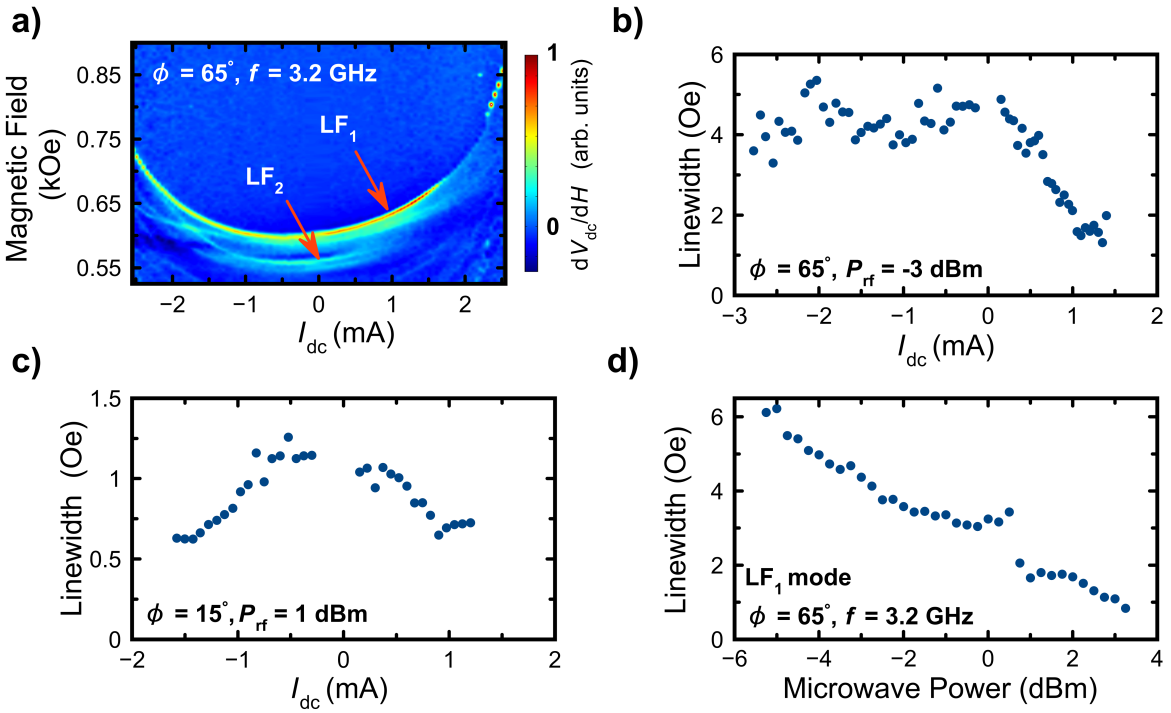

Figure 4.7: **a)** ST-FMR spectra measured as a function of magnetic field and direct current bias current I_{dc} for microwave power $P_{\mathrm{rf}} = -3\,\mathrm{dBm}$. **b)** Linewidth of the LF_1 measured as a function of the microwave drive power P_{rf}. **c)** Linewidth of the LF_1 mode as a function of direct current I_{dc} for $\phi = 65°$ and $P_{\mathrm{rf}} = -3\,\mathrm{dBm}$. **d)** Linewidth of the LF_1 mode as a function of direct current for $\phi = 15°$ and $P_{\mathrm{rf}} = 1\,\mathrm{dBm}$.

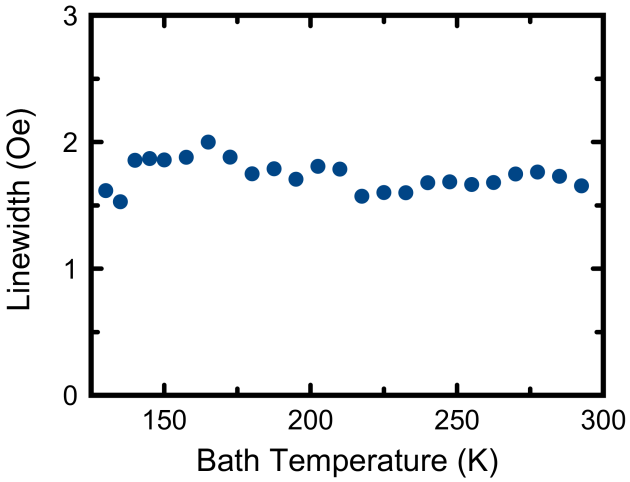

Figure 4.8: ST-FMR linewidth of the LF_1 mode as a function of bath temperature measured at the field angle $\phi = 15°$, drive frequency of 3.2 GHz and drive power $P_{rf} = 1$ dBm.

make sure this does not explain the observed behavior with bias, we perform measurements at various bath temperatures. Figure. 4.8 shows little variation in linewidth with temperature. This indicates that the symmetric decrease in linewidth with bias is due to the spin Seebeck effect.

For both angles measured here, the linewidth extracts down to zero. This indicates that the magnetic damping can be fully compensated by both of these spin current sources. We would then expect an auto-oscillatory state to be reached.

4.4 Microwave Emission

To observe microwave emission from the sample, we employ the field modulated spectrum analyzer method discussed in a previous chapter. This method is critical since the the MR is low at about roughly .01 percent. This is five orders of magnitude lower than a typical MTJ. The power from a device like this will lie in the femptowatt level and on top of low power, impedance mismatches will decrease the fraction of this power that can be detected.

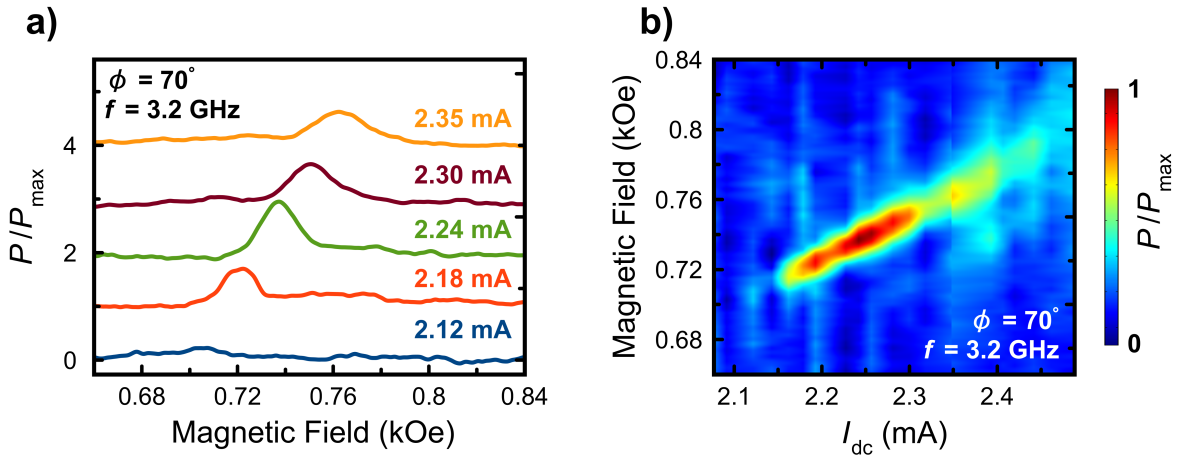

Figure 4.9: **a** Spectra of normalized microwave power P/P_{max} generated by the nanowire at the frequency $f = 3.2\,\mathrm{GHz}$ and magnetic field angle $\phi = 70°$ as a function of magnetic field at several direct current biases (vertically offset for clarity). **b** Color plot of microwave power generated by the nanowire at 3.2 GHz as a function of magnetic field and direct current bias.

In Figure 4.9a, a few traces of the field dependent microwave power detected at 3.2 GHz is shown. At around 2.12 mA, little microwave power is seen. Increasing the bias past this point results in the observation of peaks in microwave power, corresponding to the field and frequency of the lowest order spin wave mode (edge-mode) seen in ST-FMR measurements. We assemble these traces into the color plot in Fig. 4.9 to show the full range of emission.

The main contribution to driving the auto-oscillatory state can be determined by considering the angular dependence of the critical current (I_{c}) where microwave emission begins. In the case of a STO driven by the spin Hall effect, one would expect the critical current to be proportional to $1/\sin\phi$ due to the strength of the damping-like torque from spin hall depending on the projection of the polarization onto the magnetization. In contrast, the damping-like torque from the spin Seebeck effect should be angle independent since the polarization of the spin current follows the magnetization direction.

Figure 4.10 shows the measured critical current as a function of positive bias. For the angles measured, the critical current ranges from roughly 2–3 mA. If the spin Hall effect were the main source of spin current, we would expect a behavior closer to the red dotted line.

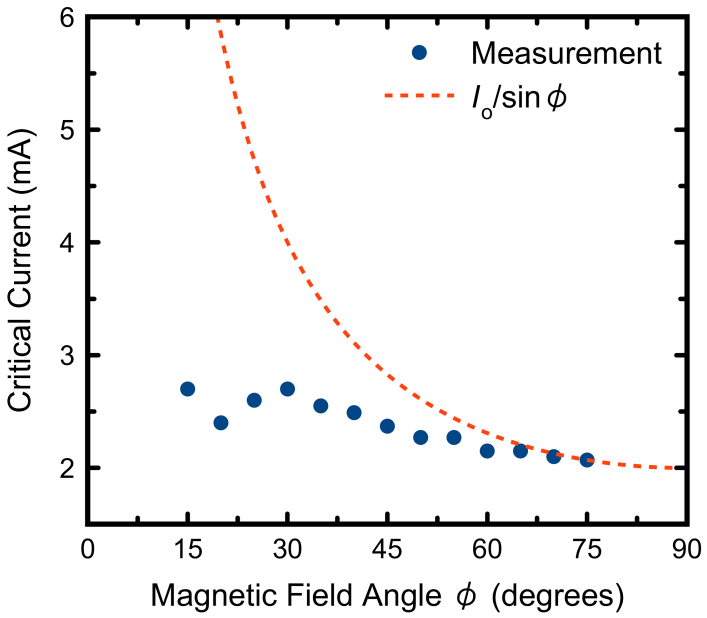

Figure 4.10: Critical current for the onset of auto-oscillations as a function of in-plane magnetic field direction ϕ. The line shows the expected behavior due to only a spin Hall current (with a fitting parameter I_0) in the absence of a spin Seebeck current.

However, at angles near the wire axis there is a large variation from $1/\sin\phi$. This indicates that the spin Seebeck effect plays a large role, since it is nearly angle independent.

The precession cone angle of the auto-oscillatory YIG magnetization can be estimated from the output microwave power of the YIG/Pt nanowire STO. The integrated microwave power P_{int} generated by an STO is proportional to the square of the direct current bias I_{dc} and the amplitude of resistance auto-oscillations δR_{ac} [9, 14]:

$$P_{\text{int}} = \frac{1}{2R_{50}} \left(I_{dc} \delta R_{ac} \frac{R_{50}}{R + R_{50}} \right)^2 \tag{4.1}$$

where R is the sample resistance and R_{50} is the $50\,\Omega$ microwave transmission line impedance. Assuming the angular dependence of the YIG/Pt nanowire resistance is $R = R_0 + \frac{\Delta R}{2}\cos 2\phi$ as expected for SMR, the small-amplitude dynamic resistance oscillations δR_{ac} are related

to the in-plane precession cone angle ϕ_c in the macrospin approximation as:

$$\delta R_{ac} = \phi_c \Delta R \sin 2\phi_0 \tag{4.2}$$

where ϕ_0 is the equilibrium direction of the YIG magnetization. The maximum value of ϕ_c achieved by the YIG magnetization in the 350 nm wide nanowire device can be calculated from Equations 1 and 2 by using the generated integrated power $P_{\text{int}} = 6\,\text{fW}$ and $\Delta R = 0.05\,\Omega$ extracted from Fig. 1b. This calculation gives the precession cone angle in the macrospin approximation $\phi_c \approx 6^\circ$. Taking into account that the excited LF mode has the edge character as shown in Fig. 4c, and that the edge mode occupies approximately one third of the nanowire volume as predicted by our micromagnetic simulations, the amplitude of the YIG magnetization oscillations at the nanowire edge is estimated to be approximately 20°. However, this is merely an estimate because contributions to the generated microwave signal beyond SMR such as inductive signal generated by precessing magnetization [15] can be non-negligible in our nanowire devices.

Chapter 5

Role of Disorder in Ni/Co Nanowires

Nanodevices based on the manipulation of magnetic materials via spin torques are the cornerstone of spintronics research. Discoveries in this field are likely to be employed in the next generation of magnetic memories and spin torque oscillators (STO). These applications require careful understanding of the material properties since they determine the threshold energy for operation and the nature of high frequency dynamics. Not only do the bulk properties matter, the structure of thin film materials has been known to lead to inhomogeneous broadening and localization of ferromagnetic resonance [61, 76]. Recently, spatial mapping of micron sized structures during ferromagnetic resonance has shown that varying material parameters alter the mode profile [77]. In this chapter we investigate the effect disorder has on nano–patterned films, specifically patterned for STO devices.

STOs rely on the injection of spin current into a ferromagnetic (FM) layer, which manipulates the magnetic damping. When the damping is fully compensated, the FM magnetization enters an auto-oscillatory state. The persistent resistance oscillations, combined with the applied direct current, make for a nanoscale source of microwave power. Typically, STO are driven by either spin polarized electric currents [9] or pure spin currents [12, 14, 15]. Here

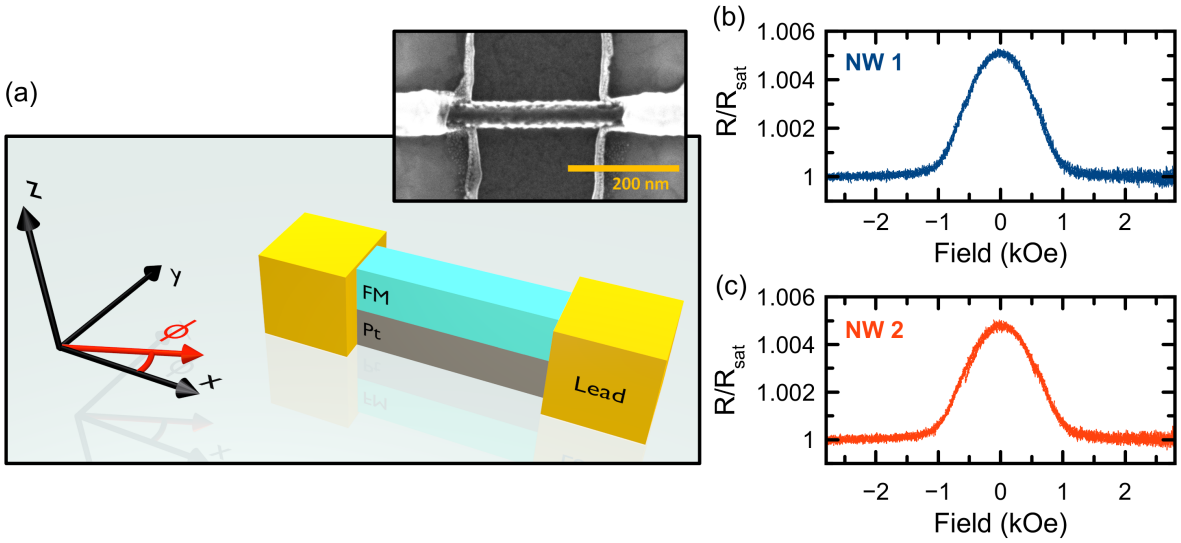

Figure 5.1: **(a)** Schematic and SEM image of typical nanowire STO along with the coordinate system used. Resistance vs applied field at $\phi = 90°$ for **(a)** NW1 and **(b)** NW2.

we investigate bilayer STO nanowires based on the spin Hall effect found in nonmagnetic materials (NM). The nanowire geometry allows for auto-oscillations by suppressing non-linear scattering channels such as four magnon scattering[14]. Further, the by decreasing the dimensions of the nanowire the mode separation can be increased[75]. We pattern nanowire STO such that one would expect a large separation in frequency for the modes, since it is known that the interactions between simultaneously excited self-oscillatory modes can substantially increase the linewidths of the generated modes. However, we measure more modes than expected and demonstrate that the FM microstructure can play a significant role in creating additional modes.

5.1 Microwave Emission

We investigate nanowire STO based on Pt(7 nm)/Co(1.7 nm)/Ni(3.4 nm)/Ta(2.5 nm) multilayers. The Ni/Co system is used to promote perpendicular magnetic anisotropy[56, 57], which allows for larger angle precession in the auto-oscillatory state[78]. We pattern the

film into 42 nm wide nanowires using e-beam lithography and ion mill techniques. Leads consisting of Nb(5)/Au(40)/Nb(5) are then attached to the wire with a gap separation of 230 nm, defining the active region of the STO. Figure 5.1a shows a SEM image of a typical device along with the coordinate system used.

We limit discussion to two devices, referred to as NW1 and NW2, but find their behavior described to be present over multiple samples. Both STO devices have similar dimensions and overall resistance. The resistance as a function of field applied at $\phi = 90°$ for the two STO discussed is shown in Fig. 5.1b,c. The ratio of resistance over the saturated resistance ($R/R_{\rm sat}$) and saturation fields for both STO are found to be very similar. However, these measurements only probe the total properties of the nanowire STO.

Application of direct current $I_{\rm dc}$ to the sample leads to cancellation of the magnetic damping and the creation of a stable auto-oscillatory state. The subsequent resistance oscillations and applied current give way to an ac voltage generated at the precession frequency. We measure traces of the frequency dependent microwave power spectral density for the two STO at multiple direct biases, and assemble them into the log-scale color plots in Figs. 5.2a,b. For both STO, a magnetic field of 1.4 kOe is applied at $\phi = 60°$. The emission characteristics at this field reveal drastically different behavior for the two devices. While in the frequency range measured both STO exhibit three modes, labeled M_1 to M_3 in order of frequency, their resonance frequencies and intensities vary significantly.

The nature of the microwave emission power for the two STO is quite different. For NW1, most of the detected power is generated by M_1, with a much lower amount generated by the other modes. In contrast, the largest output mode for NW2 is M_2. Figures 5.2c,d show the integrated power for the largest output mode in each STO. While NW2 has a larger output power, the onset of microwave emission occurs at a higher current. The critical current ($I_{\rm c}$) for this onset can be estimated from a linear fit to the inverse of the integrated power in the sub-critical regime as shown in Fig. 5.2e. Following this line to zero provides an estimate of

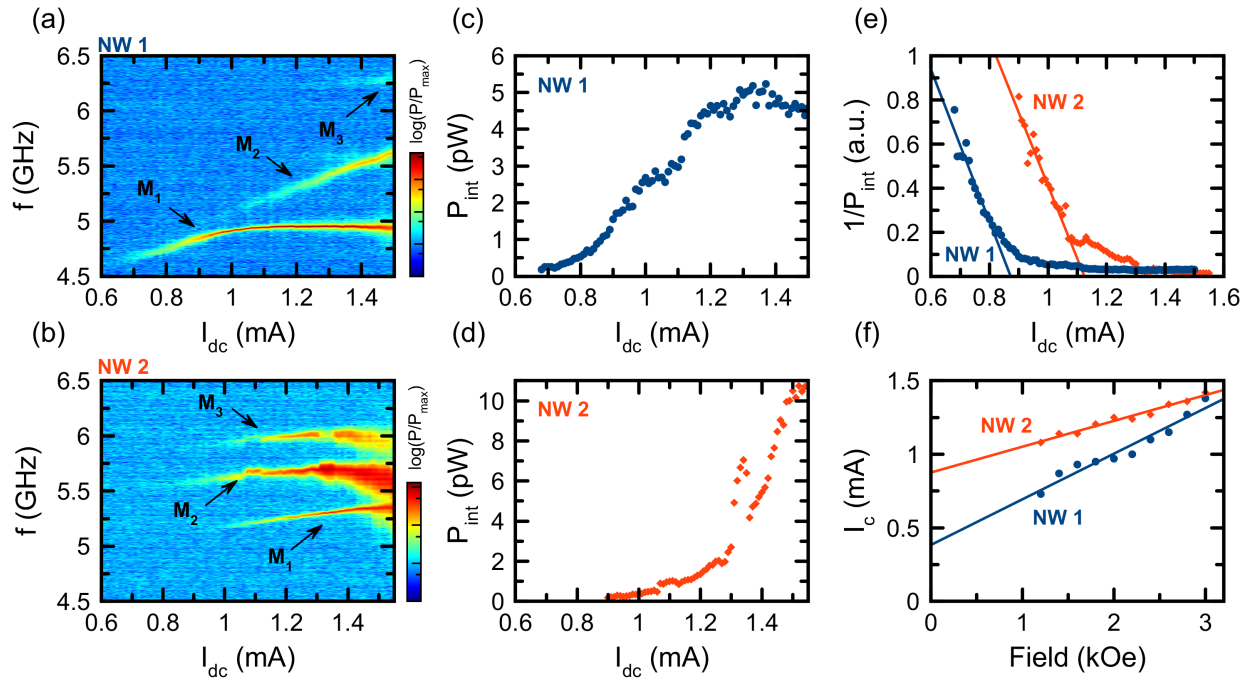

Figure 5.2: Color plots of the microwave power spectral density as a function of $I_{\rm dc}$ and frequency for **(a)** NW1 and **(b)** NW2 with 1.4 kOe applied at $\phi = 60°$. Integrated power ($P_{\rm int}$) vs $I_{\rm dc}$ for **(a)** NW1 and **(b)** NW2. **(e)** Inverse integrated power as a function of $I_{\rm dc}$ with linear fit in the sub-critical regime. Critical current as a function of applied field at $\phi = 60°$.

$I_{\rm c}$[79].

Figure 5.2f shows the critical current as a function of applied field at $\phi = 60°$. Both STO show a linear dependence for $I_{\rm c}$ as expected for a STO with low anisotropy[79]. However, the slope and intercept are different for the two. Typically, for STO the critical current is proportional to the Gilbert damping and assuming the fabrication procedure does not alter this significantly, the slope should be the same. Further, the critical current should go to nearly zero at low fields. Recent studies[15] have shown though that the inhomogeneous contribution to the linewidth can increase the linewidth.

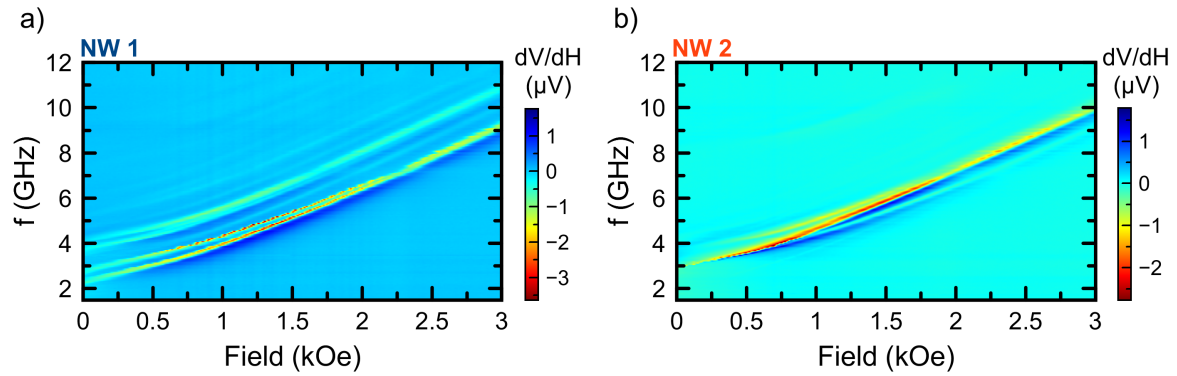

Figure 5.3: Measured ST-FMR signal as a function of frequency and applied field at $\phi = 60°$ for **(a)** NW1 and **(b)** NW2.

5.2 Spin Torque Ferromagnetic Resonance

To gain insight on the possible reasons for the different STO behavior, we assess the high frequency dynamics using field modulated spin torque resonance (ST-FMR) techniques. In this method, a rectified voltage V_{dc} during resonance is generated by the sample in response to the applied microwave current. Peaks in V_{dc} are observed at the frequency and field values corresponding to spin wave eigenmodes of the system. Figures 5.3a,b show the field dispersions for the two nanowire STO. Measurements are performed by sweeping the magnetic field at $\phi = 60°$ at discrete frequencies. For NW1 we observe a large number of modes spanning a large area of the color plot. Conversely, for NW2 we observe mostly a single grouping of modes.

In nanoscale magnetic elements, the confinement produced by the edges leads the presence of standing spin wave modes[75]. The various spin wave modes have frequency separations not only determined from material properties such as exchange and saturation magnetization, the element dimensions play an important role[49, 80]. Generally, as the dimensions are decreased, the separation between modes increases. For STO of the size used in this study, one would expect a much larger mode separation of a few GHz rather than the observed separations. While length confined modes can have a lower frequency separation, it is unlikely

that the large number of modes seen for NW1 could be from these as higher order modes require more energy to excite.

5.3 Micromagnetic Simulations

To identify the expected frequencies for the spin wave modes, we perform micromagnetic simulations in Mumax3 using realistic material parameters determined from BLS and VSM measurements. The Co/Ni bilayer is modeled as a single magnetic layer with a saturation magnetization of 798 emu/cm^3, Ku of 1.58 J/m^3 and an exchange stiffness of 7 J/m. The nanowire is modeled as being 40 nm by 6 μm in dimension with a cell grid of 10 by 1600. Simulations are performed by exciting a 200 nm region with a sinc pulse and recording the magnetization relaxation in time. A FFT of this ring down yields the eigenmodes. This is repeated for multiple applied field values to obtain the expected field dispersion.

Figure 5.4a shows a color plot generated where we consider the case of a nanowire with uniform material parameters. In the frequency range that was used in experiment, the simulated field shows only a single mode and it's harmonics. This is in contrast to the experimental results where there are a large number of modes.

In realistic materials, the material parameters are not always completely uniform. From broadband ferromagnetic resonance measurements on the film level, the film the STOs were made from had an inhomogeneous broadening of the FMR linewidth of 100 Oe. This inhomogeneity is typically associated with variations of anisotropy and is an indicator that the film is not completely uniform.

To take into account inhomogeneities, we divide the nanowire into multiple regions to simulate a granular wire. The simulated grain size is 30 nm determined from SEM imagery on the film level. These grains are then assigned a random distribution of perpendicular anisotropy

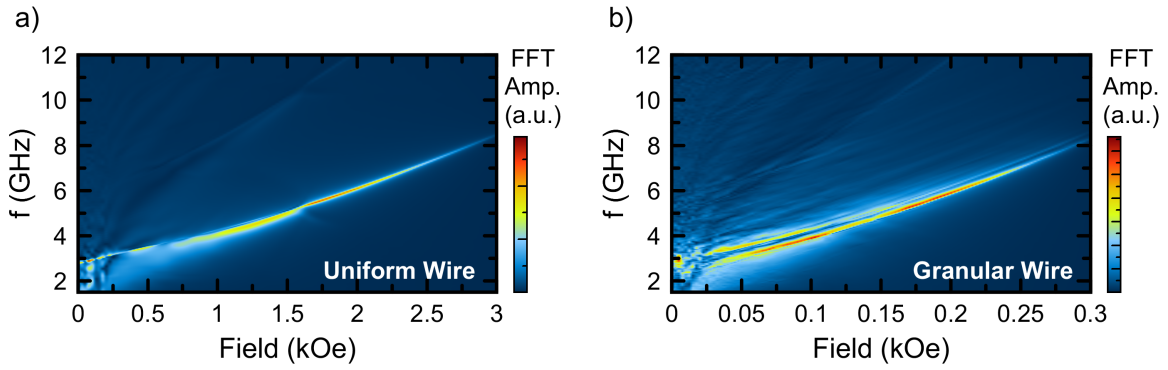

Figure 5.4: FFT amplitude from micromagnetics as a function of frequency and applied field at $\phi = 60°$ for **(a)** a uniform wire and **(b)** a granular wire.

varying 3% as determined from the film level inhomogeneous broadening. We assume that the inter-grain exchange is reduced to 40% of the bulk value.

Figure 5.4b shows the field dispersion for this granular wire. We see the addition of multiple modes that were not previously present in the uniform wire simulation. These modes are relatively closely spaced and range over a large frequency span. This is in qualitative agreement with the experimental field dispersions.

Next we consider the spatial mode profile for both cases of the uniform and granular wire. Figure 5.5 shows the amplitude of oscillations at a given resonance frequency when a 2 kOe field is applied. For the case of the uniform wire, the mode amplitude is largest (indicated by red) inside of the active region and near the edges of the nanowire. This edge-mode arises from the demagnetization field of the nanowire[74].

The spatial mode profiles for the granular wire's three lowest frequency modes shows the changes brought on by the granular structure. The lowest frequency mode retains some of the character of the edge-mode, but is more localized to the center of the nanowire. This can be understood by comparing the mode location to the anisotropy distribution pictured at the bottom of Fig. 5.5, in which darker grains represent higher perpendicular anisotropy. The mode becomes more confined due to two larger grains with higher anisotropy sitting in that

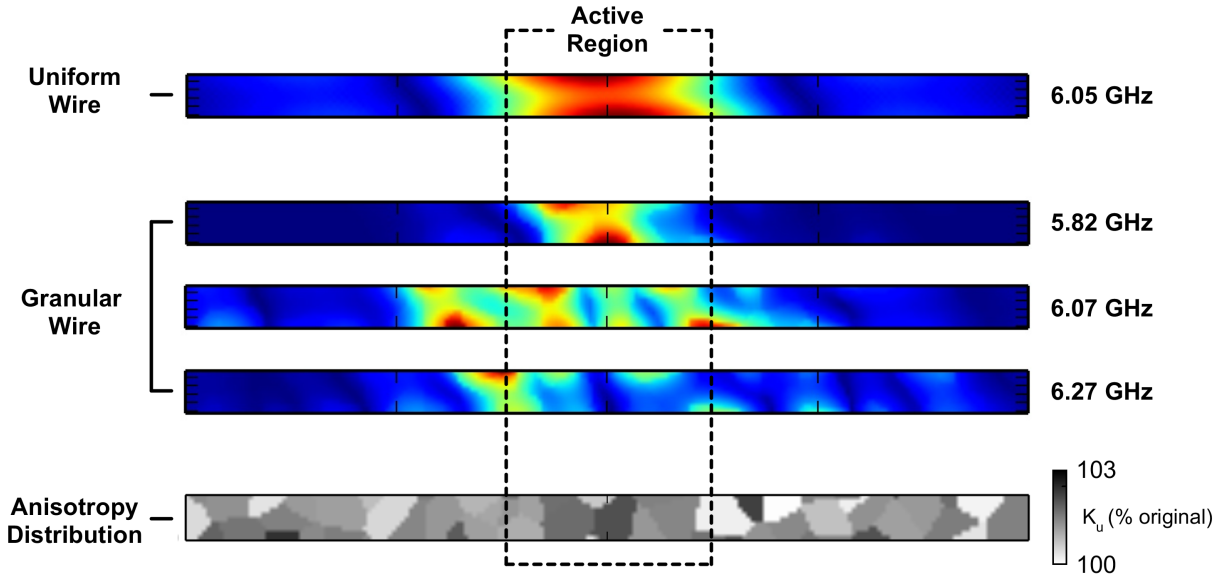

Figure 5.5: Mode profiles for the excited mode in a uniform nanowire and the three lowest frequency modes in a granular wire with the anisotropy distribution shown at the bottom.

location. For higher frequency modes, we observe mode profiles that follow the structure changes as well.

In conclusion, we observe an effect on nanowire STO performance brought on from disorder on the film level. Not only is the critical current for auto–oscillations affected, the number of available modes is as well.

Chapter 6

Planar Hall Torque

In this chapter, a spin orbit torque arising from the spin current generated by the planar Hall effect is discussed. This torque arises when the planar Hall spin current is injected into an adjacent nonmagnetic material that can serve as a spin reservoir. The strength of this torque is found to be the same order as torques generated by the spin Hall effect. Moreover, this torque exhibits a unique angular symmetry when the applied magnetic field is rotated with respect to the current flow direction.

6.1 Samples

To observe this torque, we study nanowires with a ferromagnetic layer (FM) consisting of $[\mathrm{Co}(0.85\,\mathrm{nm})/\mathrm{Ni}(1.275\,\mathrm{nm})]_{\mathrm{x2}}/\mathrm{Co}(0.85\,\mathrm{nm})$ and various nonmagnetic sink layers (NM) schematically represented in Fig. 6.1a. The Co/Ni multilayers are chosen because the have large AMR as well as large perpendicular magnetic anisotropy (PMA) [56, 57], which is used to nearly compensate the demagnetization field and allow saturation of the wire along all three principle axis as shown by the magnetoresistance measurements in Fig. 6.1b. Using

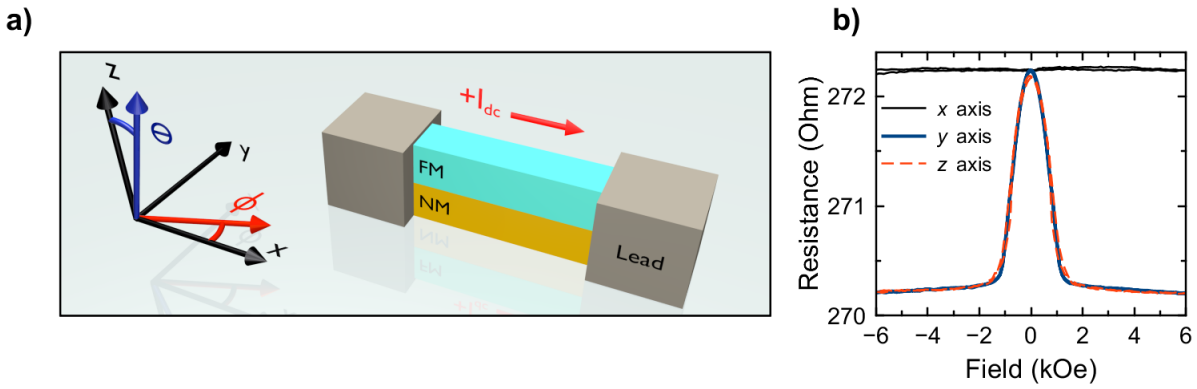

Figure 6.1: **a)** Schematic of a NM/FM nanowire device. **b)** Magnetoresistance of the Ta/Au/FM/Ta device.

conventional e-beam lithography and ion milling techniques, nanowires with widths ranging from 40–50 nm are patterned from the sputter deposited multilayer stacks (see Supplemental). Leads consisting of Ta(5 nm)/Au(40 nm)/Ta(5 nm) are sputter deposited allowing electrical current to be applied over a 100–250 nm length of the nanowire.

6.2 Spin Torque Ferromagnetic Resonance

Measurements are performed using field modulated spin torque ferromagnetic resonance techniques (ST-FMR)[44], where a microwave drive is applied to the sample and a rectified voltage is measured during resonance[41, 42]. Figure 6.2a shows the eigenmode spectra of a Ta/Au nanowire consisting of Ta(3 nm)/Au(3.9 nm)/FM/Ta(4 nm) with the magnetic field applied in the xz plane at $\theta = 225°$. We observe multiple modes in the nanowire, but we will focus on the behavior of the leading order mode labeled M1, which we show later is capable of entering an auto-oscillatory regime.

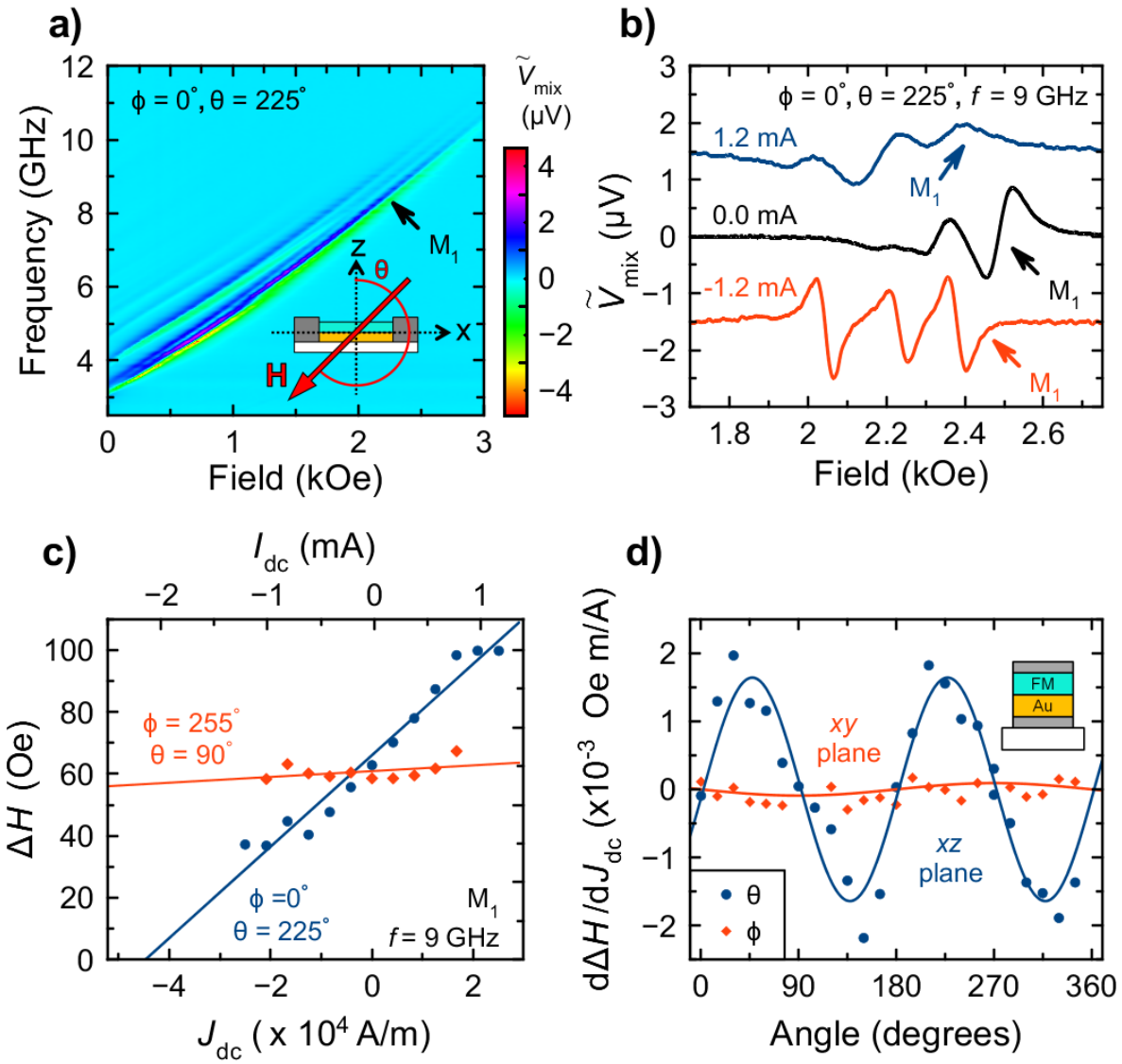

Figure 6.2: **a)** ST-FMR signal as a function of frequency and magnetic field applied in the xz plane at $\theta = 225°$. **b)** Effect of current bias I_{dc} on ST-FMR spectra at $\theta = 225°$. **c)** Linewidth ΔH of mode M_1 as a function of sheet current density J_{dc} for magnetization in the xy (red) and xz (blue) planes. **d)** Angular dependence of $d\Delta H/dJ_{dc}$ in the xy and xz planes for the Ta/Au/FM/Ta device.

6.2.1 Bias Dependence Gold Based Samples

Figure 6.2b shows several spectra taken with a constant microwave drive of 9 GHz and field applied at $\theta = 225°$ in the xz plane For a positive current inside the ferromagnetic layer of 1.2 mA we see a decrease in the mode amplitude and a broadening of the linewidth compared to zero applied bias. Application of negative current results in a narrowing of the modes seen.

The linewidth of the leading order mode (M1) as a function of J_{dc}, where J_{dc} is I_{dc} divided by the nanowire width, is shown in Fig 6.2c. It shows a linear dependence when measured in the XZ plane where PHT is maximal. In contrast, in the xy plane where torques from the spin Hall and Rashba effects are maximal, little variation of the linewidth is observed. The magnetic field is then rotated in the xz plane and measurements of ΔH vs J_{FM} are performed. The slope of ΔH vs J_{dc} is shown to vary as $\sin\theta\cos\theta$ in Fig. 6.2d. This is a unexpected result compared to well studied spin torques resulting from the spin Hall[81] and Rashba[82] effects, where no damping–like torques would be expected in the xz plane. Further, in the xy plane where these torques should be strong, we observe no significant variation in linewidth indicating that the spin Hall effect present in the Ta layers provides no significant spin torques.

6.2.2 Changing the NM Layer

Aside from the Au based nanowire, the NM layer is swapped out for Pt(7.0 nm) and Pd(8.0 nm) to determine the role of spin Hall angle on PHT. The layer thickness is chosen to keep the current distribution the same between the layers. Figure 6.3a shows the angular dependence of $d\Delta H/dJ_{\mathrm{dc}}$ measured in the xy plane. As expected from torques produced by the spin Hall effect[81], we observe a 360°-periodic anti–damping torque that is largest in Pt followed by Pd which corresponds to their relative spin Hall angles. However, in the xz plane as

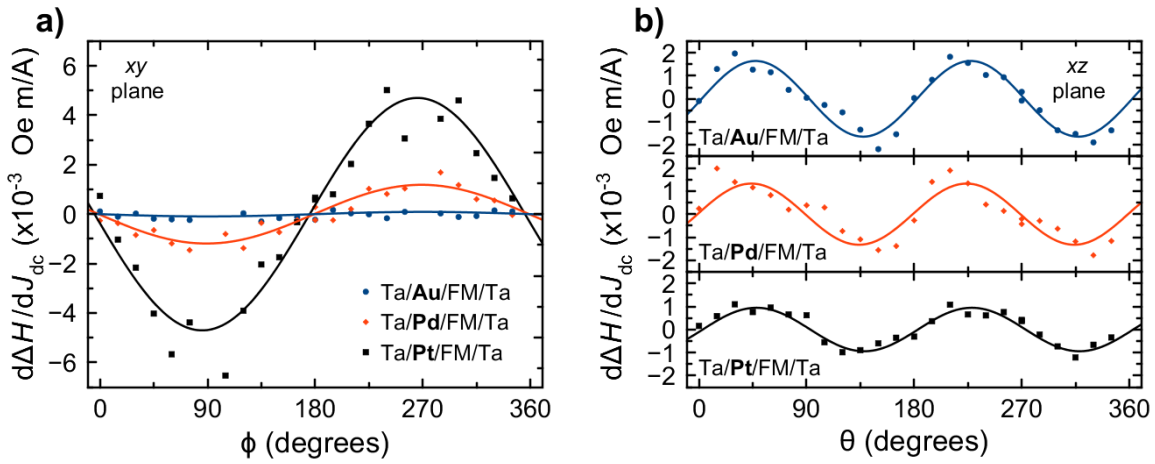

Figure 6.3: $d\Delta H/dJ_{\mathrm{dc}}$ measured at $T = 295\,\mathrm{K}$ for different NM layers characterizing the strength of **a)** antidamping SHT in the xy plane and **b)** antidamping PHT in the xz plane .

shown in Fig 6.3b, $d\Delta H/dJ_{\mathrm{dc}}$ observes a 180°-periodic anti–damping torque that shows little variation with spin Hall angle. This indicates that the origin of this torque is in the FM layer and that the NM is only required to serve as a spin reservoir.

6.2.3 Au Based Sample at 77 K

Measurements of ST-FMR can be used to determine which mode enters the auto-oscillatory regime and estimate the critical current J_{c} required. J_{c} is taken to be the current that the linewidth reaches zero indicating a full cancellation of damping. Figure 6.4a shows this measurement taken where PHT is maximal at both room temperature and in a liquid nitrogen bath. The critical current at room temperature is too high to reach without damaging the device from Ohmic heating, so the high bias regime needs to be investigated with cooling. Further, the critical current is less at lower temperature due to AMR increasing at lower temperatures[38].

Figure 6.4b shows a color plot assembled from spectra taken at multiple DC biases and 6 GHz drive in a 77 K bath. At roughly -0.75 mA the leading order mode (M1) shows a large

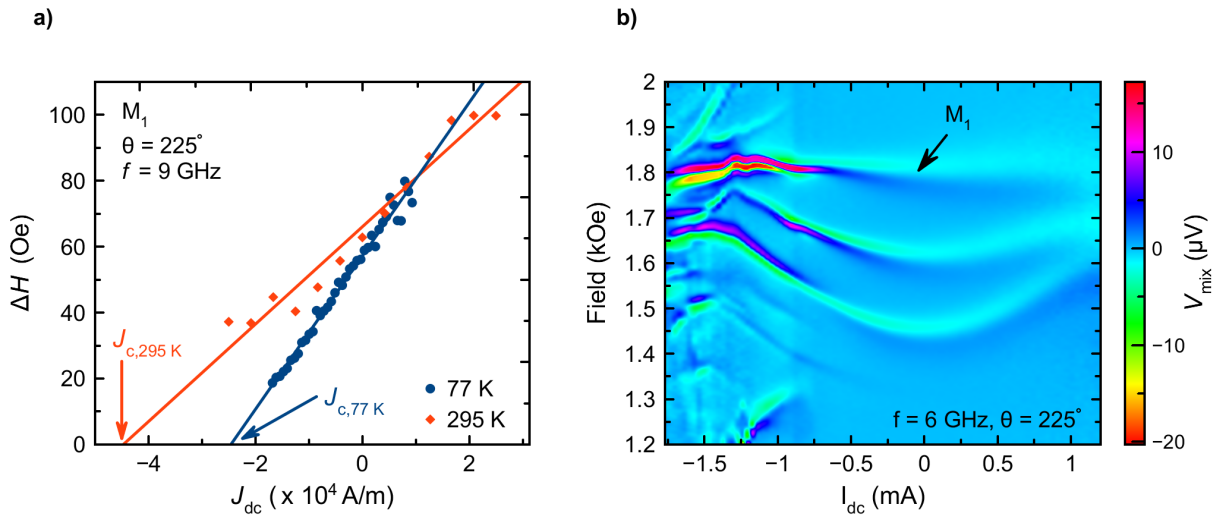

Figure 6.4: **a)** ST-FMR linewidth of the M_1 mode as a function of direct sheet current density J_{dc} applied to the Ta(3 nm)/Au(3.9 nm)/FM/Ta(4 nm) nanowire device at $T = 77$ K (blue symbols) and $T = 295$ K (red symbols). **b)** Color plot of ST-FMR signal as a function of applied field and bias with a 6 GHz microwave drive.

increase in amplitude coinciding with the FMR linewidth of this mode approaching near zero. Along with this there is a large number of additional modes excited and a deviation in resonance position from the parabolic dependence expected from Ohmic heating[10]. In contrast, positive currents for this angle show no excitation. This indicates that at large negative currents the M1 mode can enter the auto–oscillatory regime.

6.3 Microwave Emission

The linewidth vs bias data suggests that if a sufficiently high bias is applied, the linewidth can reach near zero. In this regime auto-oscillations of the magnetization would be expected, where the lowest order mode begins to precess. The applied bias current rectifies against the GHz frequency resistance changes causing a microwave voltage to be produced giving the basic operation of a spin toque oscillator[9, 14]. Since a significantly high bias needs to be applied to the sample, the joule heating at room temperature prevents the realization of this

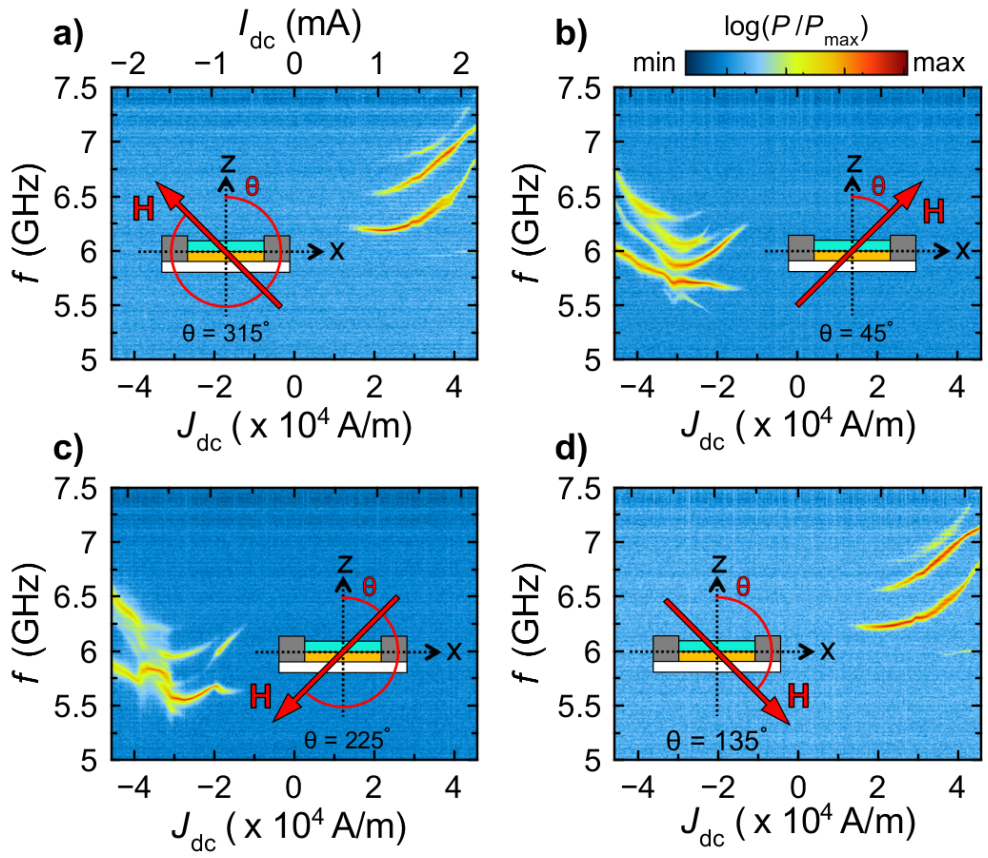

Figure 6.5: Normalized power spectral density of microwave signal generated by the Ta/Au/FM/Ta device in a 1.7 kOe magnetic field applied in the xz plane at four angles **a**, $\theta = 315°$, **b**, $\theta = 45°$, **c**, $\theta = 135°$, and **d**, $\theta = 225°$.

state. To circumvent this issue, we submerge the sample in a liquid nitrogen bath (77 K).

Figure 6.5 shows the microwave power detected by a spectrum analyzer as a function of J_{dc}. Field is applied in xz plane ($\phi = 0°$) at angles $\theta = 45°, 135°, 225°, 315°$ where PHT is largest in magnitude, At each of these angles, we observe a sharp onset in microwave power when high enough anti–damping spin current is injected into the FM layer. The lack of signal when using the opposite polarity indicates that this is not just detection of thermal magnoise. Further, the polarity required for microwave emission matches the symmetry seen in ST-FMR measurements. This demonstrates that the auto-oscillatory state driven purely by the PHT.

The integrated power P_{int} (blue symbols) emitted by mode M_1 in the nanowire device is

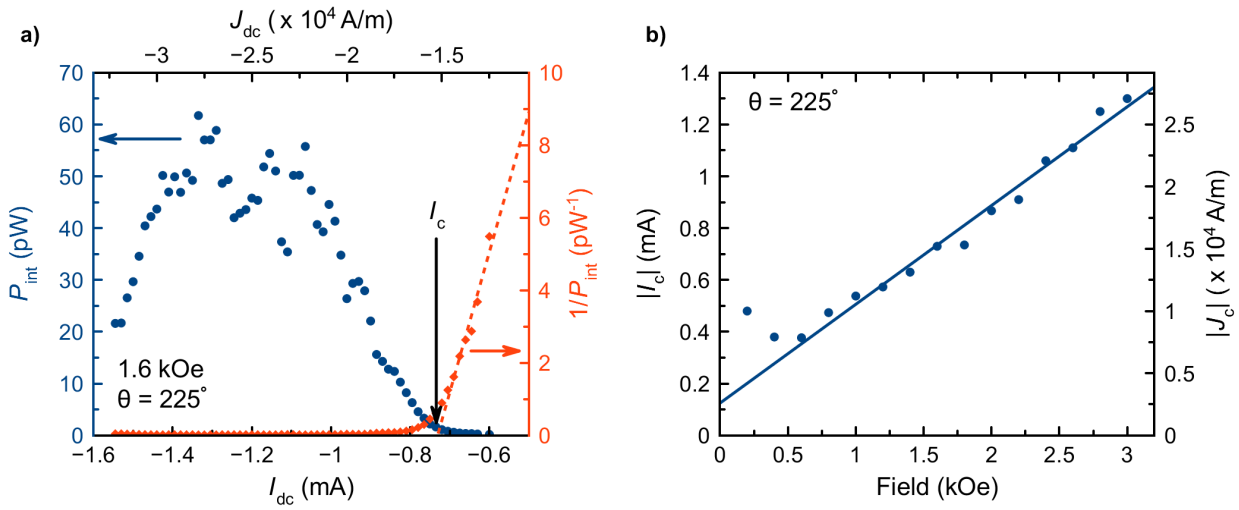

Figure 6.6: **a)** Integrated power P_{int} emitted by the Ta(3 nm)/Au(3.9 nm)/FM/Ta(4 nm) nanowire device in its lowest spin wave mode M_1 at $T = 77$ K (blue symbols) as a function of current bias measured in a 1.6 kOe magnetic field applied at $\theta = 225°$. The inverse power $1/P_{\text{int}}$ is shown by red symbols. **b)** Absolute value of the critical current for the onset of the auto-oscillations $|I_c|$ as a function of magnetic field applied at $\theta = 225°$.

shown in Fig. 6.6a. The power is expressed as power delivered to a 50 Ω load and is corrected for frequency dependent attenuation and amplification in the microwave measurement circuit. The data in Fig. 6.6a is collected in a 1.6 kOe magnetic field applied at $\theta = 225°$ in the xz plane. We observe a large increase in the emitted microwave power above the background level for $I_{\text{dc}} < -0.7$ mA. A more precise evaluation of I_c can be obtained by fitting the inverse of the integrated power (red symbols in Fig. 6.6a) to a straight line for sub-critical values of I_{dc} [79]. The critical current obtained via such a procedure from the data in Fig. 6.6a is $I_c = -0.73$ mA.

Figure 6.6b shows the dependence of I_c on magnetic field H applied at $\theta = 225°$ in the xz plane. Apart from the low field regime, this dependence is well fit by a straight line. This linear dependence of I_c on H is expected for our devices because magnetic anisotropy of the nanowire is relatively small [79, 83]. In the low field regime, magnetization of the nanowire starts to deviate from the applied field direction that maximizes the PHT efficiency ($\theta = 225°$), which leads to an increase of I_c.

6.4 Planar Hall Torque

The planar Hall effect leads to a current $\mathbf{J}_{\mathrm{PHE}} = \Delta\sigma_{\mathrm{AMR}}(\hat{\mathbf{m}} \cdot \mathbf{E})\hat{\mathbf{m}}$ flowing parallel to the FM magnetization where $\mathbf{E}$ is the electric field applied to the FM ($\mathbf{E} \approx E\hat{\mathbf{x}}$). Assuming the anti–damping SOT originates from exchange of angular momentum between the FM and NM layers via spin currents, only the component of $\mathbf{J}_{\mathrm{PHE}}$ normal to the NM/FM interface can contribute to the SOT. Figure 6.7a shows the case of positive currents for the given orientation of magnetization. The planar Hall effect leads to a polarized electron flow injected into the NM layer. In this layer they loose their polarization, representing a transfer of momentum. For this case this acts as an anti–damping torque. Since the net flow of current in the z direction must be zero, there must be a backflow current from the NM layer that caries no net polarization. Reversing the current flow, as shown in Fig 6.7b, then results in an increase in damping.

In the mechanism proposed for PHT, it only relies on the z projection of $\mathbf{J}_{\mathrm{PHE}}$. Taking this projection results in:

$$J^z_{\mathrm{PHE}} = \Delta\sigma_{\mathrm{AMR}} E(\hat{\mathbf{m}} \cdot \hat{\mathbf{x}})(\hat{\mathbf{m}} \cdot \hat{\mathbf{z}}). \tag{6.1}$$

Figure 6.7d shows a polar plot of the strength of PHT from this symmetry where red represents antidamping and blue damping for the giver current polarity. This angular dependence matches the observed dependence on PHT $\cos(\theta)\sin(\theta)\cos(\phi) = (\hat{\mathbf{m}} \cdot \hat{\mathbf{x}})(\hat{\mathbf{m}} \cdot \hat{\mathbf{z}})$ seen in ST-FMR measurements. The biaxial nature of this torque is a defining feature of PHT and is clearly different than the symmetry of spin Hall torques as illustrated in Fig. 6.7d,

If the PHT arises from the z component of $\mathbf{J}_{\mathrm{PHE}}$, then splitting the gold reservoir should result in the situation shown in Fig. 6.7c. One reservoir provides an antidamping current and the other a damping current, resulting in no net torque. We create a nanowire with

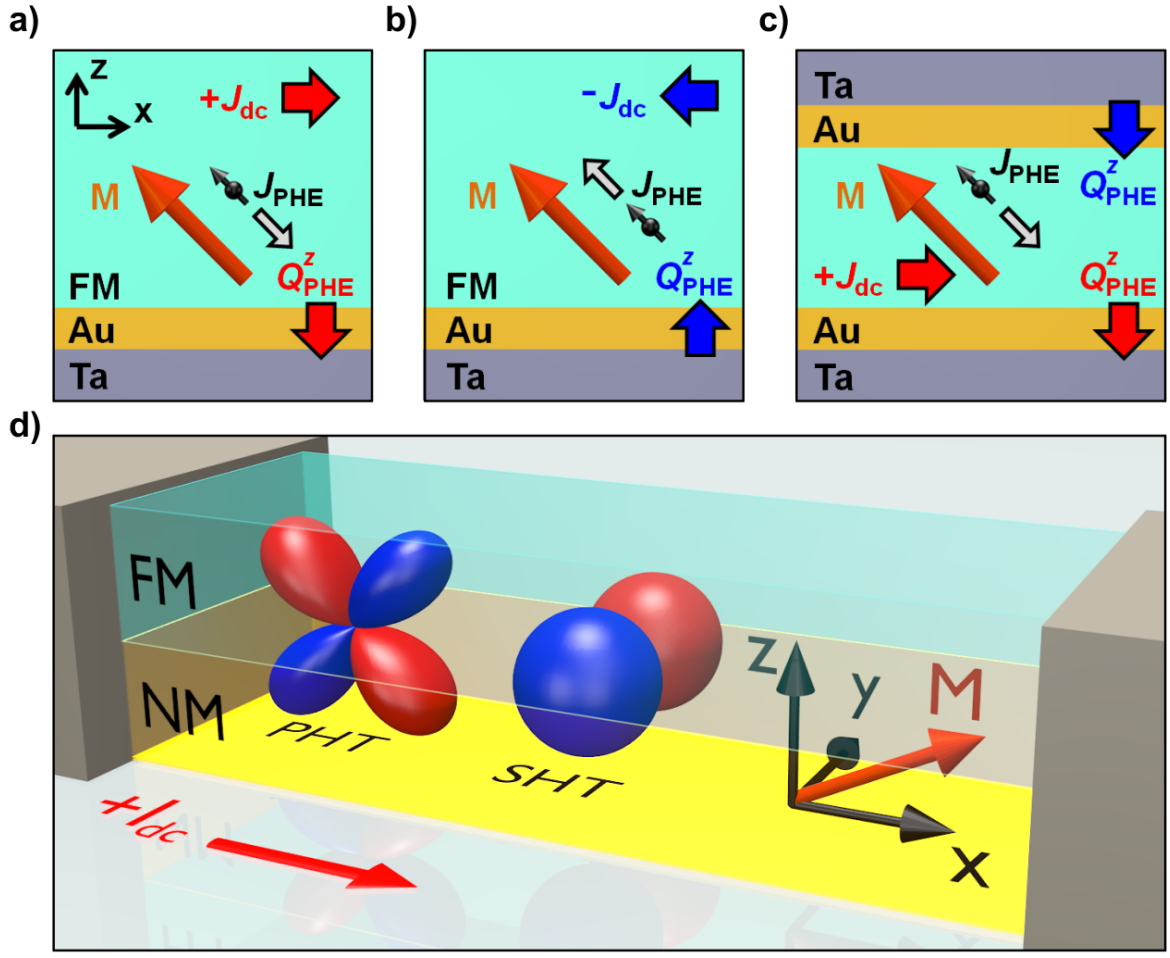

Figure 6.7: Schematics illustrating the flow of pure spin current $Q^z_{\rm PHE}$ driven across the NM/FM interface by spin-polarized planar Hall current $\mathbf{J}_{\rm PHE}$ in the FM layer for **a**, $J_{\rm dc} > 0$ and **b**, $J_{\rm dc} < 0$ in the Ta/Au/FM/Ta device and **c**, $J_{\rm dc} > 0$ in the Ta/Au/FM/Au/Ta device. **d**, Schematic illustrating the angular dependence of anti–damping SOTs in NM/FM bilayers: biaxial PHT and uniaxial SHT (red corresponds to negative damping while blue corresponds to positive damping when $J_{\rm dc} > 0$).

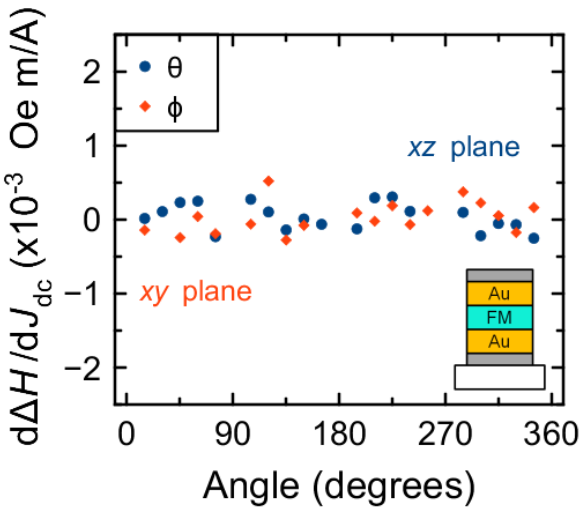

Figure 6.8: Angular dependence of $d\Delta H/dJ_{\rm dc}$ in the xy and xz planes for the Ta/Au/FM/Au/Ta device.

layers consisting of Ta(3 nm)/Au(2.5 nm)/FM/Au(1.5)/Ta(4 nm). With roughly balanced spin reservoirs placed on both sides of the FM layer, we observe a suppression of PHT as shown in Fig 6.8. This indicates that the source and sink effects cancel out resulting in no net spin current flow. Further, this suggests the origin of the PHT is not related to the Co/Ni multilayers by themselves, but rather the interface between them and another material.

6.5 Planar Hall Strength with Temperature

Both PHT and AMR arise from the planar Hall current in the FM layer, and thus PHT is expected to increase with increasing AMR. Since AMR in our NM/FM systems strongly depends on temperature, we can test the relation between PHT and AMR by measuring their temperature dependence.

The angular dependence of normalized resistance of a Ta(3 nm)/Au(3.9 nm)/FM/Ta(4 nm) multilayer as a function of the direction of a 4 kOe saturating magnetic field applied in the plane of the sample is shown in Fig. 6.9. The data reveal that the AMR ratio $\Delta\rho_{\rm AMR}/\rho$

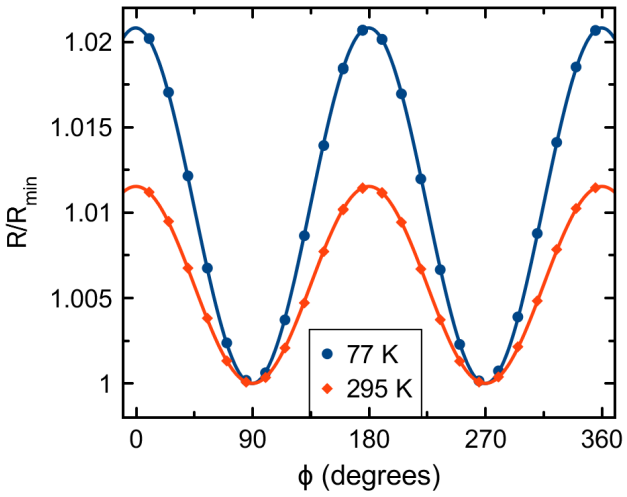

Figure 6.9: Normalized resistance of the Ta(3 nm)/Au(3.9 nm)/FM/Ta(4 nm) film as a function of 4 kOe magnetic field angle applied in the xy plane at 77 K (blue symbols) and 295 K (red symbols).

of the multilayer increases by 80% at $T = 77\,\mathrm{K}$ compared to its room temperature value: $(\Delta\rho_{\mathrm{AMR}}/\rho)_{295\,\mathrm{K}} = 0.0116$; $(\Delta\rho_{\mathrm{AMR}}/\rho)_{77\,\mathrm{K}} = 0.0209$:

$$\frac{(\Delta\rho_{\mathrm{AMR}}/\rho)_{77\,\mathrm{K}}}{(\Delta\rho_{\mathrm{AMR}}/\rho)_{295\,\mathrm{K}}} = 1.8. \tag{6.2}$$

Fig. 6.4a shows the critical sheet current density for the onset of auto-oscillations J_{c} measured by ST-FMR in the Ta(3 nm)/Au(3.9 nm)/FM/Ta(4 nm) nanowire device at $T = 295\,\mathrm{K}$ and $T = 77\,\mathrm{K}$. This J_{c} measured at 9 GHz decreases from $J_{\mathrm{c},295\,\mathrm{K}} = -4.4 \times 10^4\,\mathrm{A/m}$ at room temperature to $J_{\mathrm{c},77\,\mathrm{K}} = -2.5 \times 10^4\,\mathrm{A/m}$ at 77 K. The value of $J_{\mathrm{c},77\,\mathrm{K}}$ measured by ST-FMR (at 9 GHz corresponding to $H = 2.83\,\mathrm{kOe}$) is in agreement with the value of J_{c} obtained from the microwave emission measurements at this magnetic field value, as shown in Fig. 6.6b. The observed temperature-induced variation of J_{c} is consistent with the expected increase of the PHT efficiency due to the low-temperature increase of the planar Hall current and AMR.

The critical sheet current density can be approximated by [83]:

$$J_{\mathrm{c}} \approx \frac{2e}{\hbar}\frac{\alpha}{\eta}dM_s\frac{\omega}{\gamma} \tag{6.3}$$

where e is the electron charge, $\hbar$ is the reduced Planck's constant, d is the FM layer thickness, ω is the oscillation angular frequency, γ is the gyromagnetic ratio, and η is a PHT efficiency parameter characterizing conversion of the sheet current density J_{dc} into the spin current density Q^z_{PHE}.

The ratio of the PHT efficiencies at $T = 77\,\mathrm{K}$ and $T = 295\,\mathrm{K}$ can be determined from Eq. (6.3):

$$\frac{\eta_{77\,\mathrm{K}}}{\eta_{295\,\mathrm{K}}} = \frac{J_{\mathrm{c},295\,\mathrm{K}}}{J_{\mathrm{c},77\,\mathrm{K}}}\frac{\alpha_{77\,\mathrm{K}}}{\alpha_{295\,\mathrm{K}}}, \tag{6.4}$$

where we neglect the temperature dependence of M_{s} since it was shown to change by less than 4% between 295 K and 4 K [57, 84, 85]. We employ broadband ferromagnetic resonance to measure the Gilbert damping parameter α at $T = 295\,\mathrm{K}$ and $T = 77\,\mathrm{K}$ and find $\alpha_{295\,\mathrm{K}} = 20.9 \times 10^{-3}$ while $\alpha_{77\,\mathrm{K}} = 22.2 \times 10^{-3}$. Substituting the measured values of J_{c} and α into Eq. (6.4), we obtain:

$$\frac{\eta_{77\,\mathrm{K}}}{\eta_{295\,\mathrm{K}}} = 1.9 \pm 0.1. \tag{6.5}$$

This however, ignores the change in current distribution between the two layers arising from the different temperature dependencies of each layers conductivity. A more rigorous calculation can be done using the sheet resistances. The total resistance measured (R_{TOT}) includes the measurement of the NM layer (R_{NM}), which shunts some of the applied current. Assuming the resistance of the FM layer R_{FM} is a base resistance R_{oFM} plus a contribution from AMR (ΔR_{oFM}), a parallel resistor model can be used to calculate the actual strength

of the AMR in the FM layer.

$$\begin{aligned} R_{\mathrm{FM}} &= R_{\mathrm{oFM}} + \Delta R_{\mathrm{FM}} \\ R_{\mathrm{TOT}} &= R_{\mathrm{oTOT}} + \Delta R_{\mathrm{TOT}} \end{aligned} \tag{6.6}$$

$$\frac{1}{R_{\mathrm{TOT}}} = \frac{1}{R_{\mathrm{FM}}} + \frac{1}{R_{\mathrm{NM}}} \tag{6.7}$$

We calculate at room temperature $(\Delta R_{\mathrm{FM}}/R_{\mathrm{oFM}})_{295\,\mathrm{K}} = 0.039$ and at low temperature $(\Delta R_{\mathrm{FM}}/R_{\mathrm{oFM}})_{77\,\mathrm{K}} = 0.058$. The spin current produced in the FM layer not only depends on the strength of the planar Hall effect, but also the fraction of current passing through the FM layer (J_{FM}). Using a parallel resistor model again:

$$J_{\mathrm{FM}} = \frac{R_{\mathrm{NM}}}{R_{\mathrm{NM}} + R_{\mathrm{oFM}}} J \tag{6.8}$$

Then computing the following ratio yields:

$$\frac{(J_{\mathrm{FM}}\Delta R_{\mathrm{FM}}/R_{\mathrm{oFM}})_{77\,\mathrm{K}}}{(J_{\mathrm{FM}}\Delta R_{\mathrm{FM}}/R_{\mathrm{oFM}})_{295\,\mathrm{K}}} = 1.9. \tag{6.9}$$

Comparison of Eq. (6.3) and Eq. (6.5)/(6.9) shows that the PHT efficiency scales with the AMR ratio, which supports the planar Hall current origin of PHT.

6.6 Aluminum Capping Layer

For all the samples discussed in the main text the ferromagnetic layer was capped with 3 nm of tantalum. As shown from damping measurements on the film level, the transport of spin current from the FM to Ta is less efficient without a gold layer inbetween. To verify the top

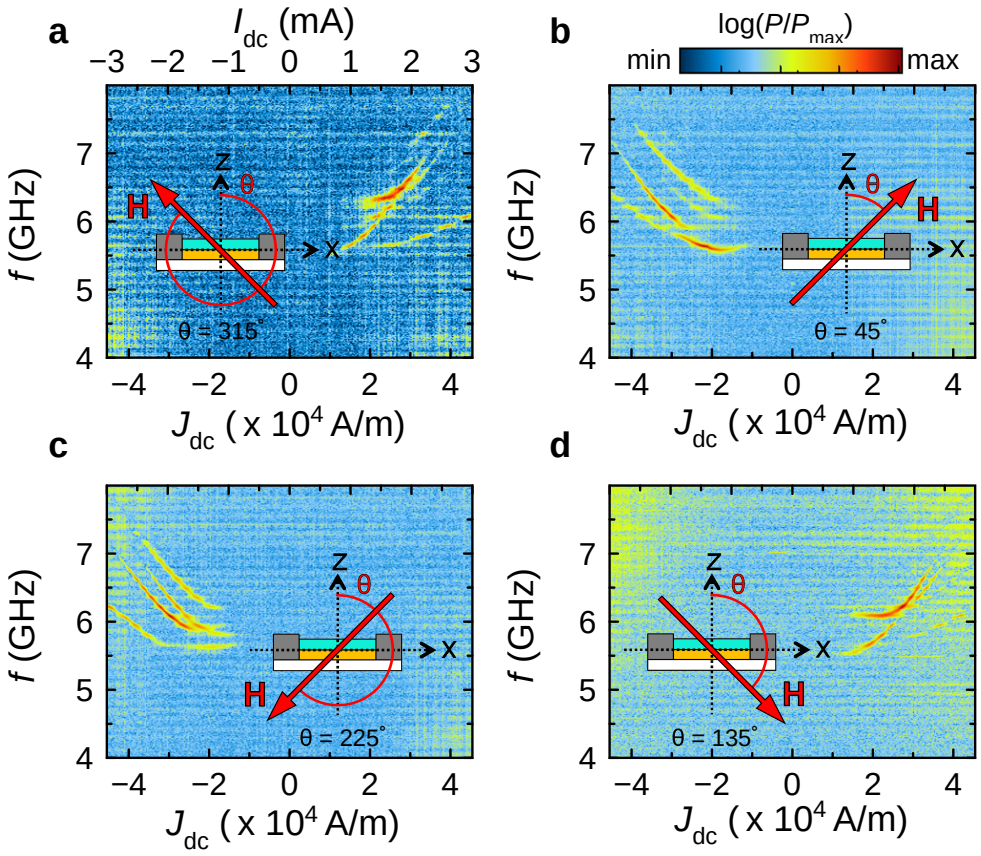

Figure 6.10: **Microwave generation at $T = 77$ K.** Normalized power spectral density of microwave signal generated by the Ta/Au/FM/Au/Al device in a 1.7 kOe magnetic field applied in the xz plane at four angles **a**, $\theta = 315°$, **b**, $\theta = 45°$, **c**, $\theta = 135°$, and **d**, $\theta = 225°$.

Ta cap has little influence on the strength of the planar Hall torque, we replace the Ta cap with Au(1 nm)/Al(2 nm) and pattern the film into a 66 nm wide 220 nm long nanowire.

We submerge the nanowire in a liquid nitrogen bath and apply a 1.7 kOe field at the angles where PHT is maximal. We observe an onset of microwave emission in Fig. 6.10 when a direct current is applied to the Ta/Au/FM/Au/Al device with the same symmetry expected from PHT. Moreover, the emission starts at similar current densities as the Ta/Au/FM/Ta device discussed in earlier. This indicates that strong spin orbit coupling is not necessary in the top layer for the generation of the observed torques.

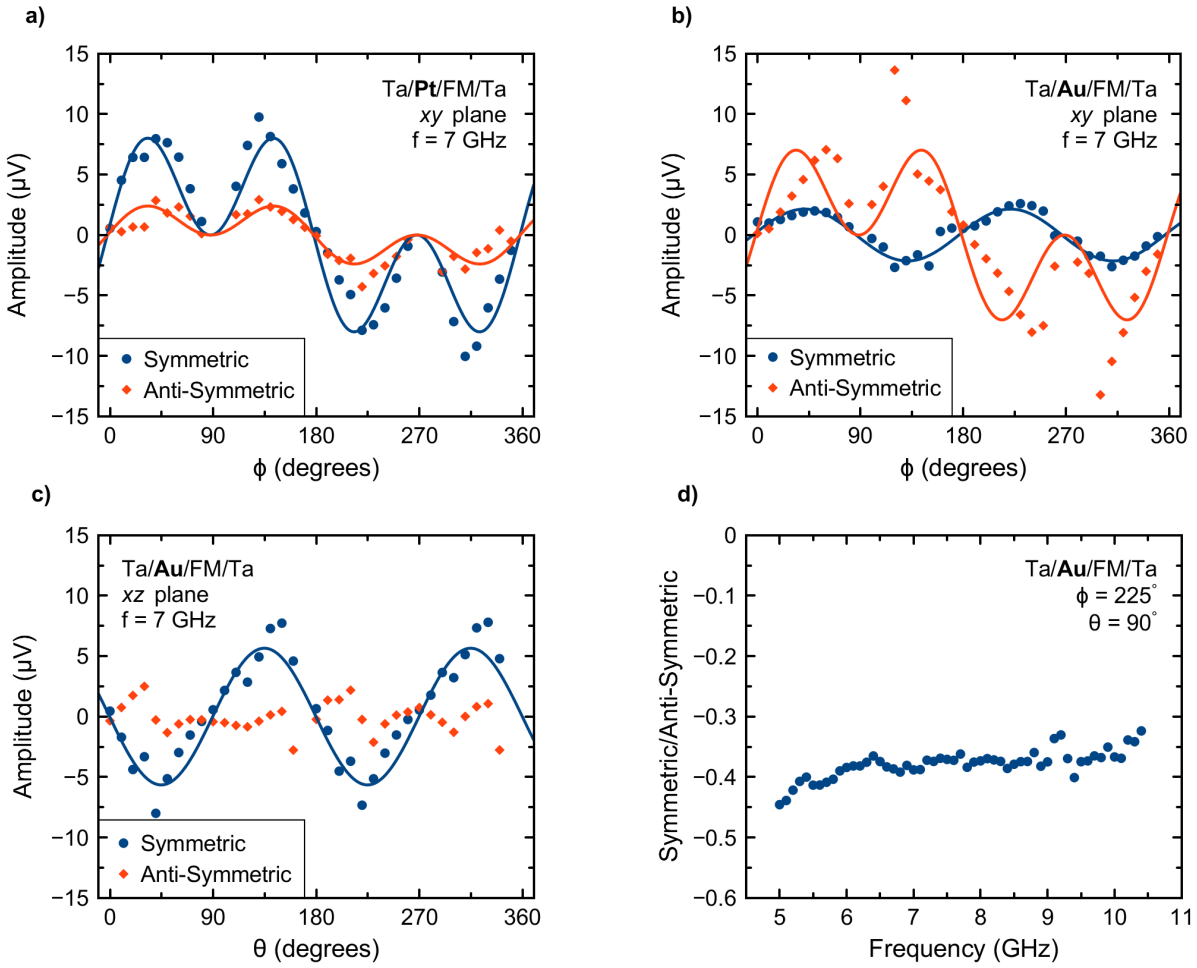

Figure 6.11: **a** Normalized resistance of the Ta(3 nm)/Au(3.9 nm)/FM/Ta(4 nm) film as a function of 4 kOe magnetic field angle applied in the xy plane at 77 K (blue symbols) and 295 K (red symbols).**b** ST-FMR linewidth of the M_1 mode as a function of direct sheet current density J_{dc} applied to the Ta(3 nm)/Au(3.9 nm)/FM/Ta(4 nm) nanowire device at $T = 77$ K (blue symbols) and $T = 295$ K (red symbols).

6.7 ST-FMR Lineshape Analysis

Analysis of ST-FMR lineshapes has been used to identify and quantify torques[86–88] originating from spin Hall and Rashba effects. In the linear regime, the voltage produced sweeping an applied field H trough a resonance H_{res} is the sum of a symmetric and anti-symmetric

Lorentzian:

$$V_{\mathrm{dc}} = \frac{S\Delta H^2}{(H - H_{\mathrm{res}})^2 + \Delta H^2} + \frac{A\Delta H\,(H - H_{\mathrm{res}})}{(H - H_{\mathrm{res}})^2 + \Delta H^2}. \tag{6.10}$$

where δH is the HWFM linewidth. S and A represent the amplitudes of the symmetric and anti-symmetric components, respectively. These amplitudes can be determined from the LLG equation where the spin torque effective fields are used as a perturbation $\delta H$to the static H field as discussed in ref [87]:

$$\frac{\partial \mathbf{M}}{\partial t} = -\gamma\left[\mathbf{M} \times (\mathbf{H}_{\mathrm{eff}} + \delta\mathbf{H})\right] + \frac{\alpha}{M_{\mathrm{s}}}\left[\mathbf{M} \times \frac{\partial \mathbf{M}}{\partial t}\right]. \tag{6.11}$$

where in Cartesian:

$$\delta\mathbf{H} = (h_x, h_y, h_z)\, e^{i\omega t} \tag{6.12}$$

Taking into account the dynamic change of resistance during resonance, the resulting amplitudes for the symmetric and anti-symmetric components are then:

$$S \propto h_z \sin 2\phi. \tag{6.13}$$

$$A \propto -h_x \sin\phi \sin 2\phi + h_y \cos\phi \sin 2\phi. \tag{6.14}$$

where h is the component of the spin torque equivalent field for the conventional field like (τ_{fl}) and Slonczewski (τ_{s}) torques:

$$\mathbf{T} \;= -\frac{\gamma\tau_{\mathrm{fl}}}{M_{\mathrm{s}}}\mathbf{M} \times [\mathbf{M} \times \mathbf{P}] - \gamma\tau_{\mathrm{s}}\mathbf{M} \times \mathbf{P} \tag{6.15}$$

For in-plane rotations, the magnitude τ_s of the Slonczewski damping-like torque[1] is proportional to h_z

For this section, we perform ST-FMR measurements using an amplitude modulated scheme rather than field modulated, since it provides a direct value for the amplitude. Figure 6.11a shows the angular dependence of the lineshape components for the Pt based sample in the xy plane. For damping–like spin torques produced by the spin Hall and Rashba effects, the effective field h_z varies as $\cos\phi$ [87, 88]resulting in the observed $\cos\phi \sin 2\phi$ angular dependence of the symmetric component. In this system, the anti–symmetric component caries the same symmetry since the Oersted field drive it corresponds to is in the y direction.

If the observed PHT was related to the spin Hall and Rashba effects, we would then expect a similar result for the sample where the NM layer is switched to gold. As seen in Fig. 6.11b, the symmetric component no longer exhibits a $\cos\phi \sin 2\phi$ angular dependence, but rather varies as $\sin 2\phi$. This suggests that h_z is primarily a constant drive. This is most likely due to inhomogeneities of the microwave Oersted field from the drive current.

Figure 6.11c shows the amplitudes for the lineshape components when the magnetic field is rotated in the xz plane. Assuming the symmetric component still represents the strength of the Slonczewski damping-like torque, the angular dependence of the symmetric component varies as $\sin 2\phi$. This indicates that the effective field is roughly constant in the direction normal to the xz plane. In this configuration, the Oersted field is in this direction.

Measurements of the relative amplitude between the symmetric and anti-symmetric components can be complicated by phase differences between the microwave drive and resulting response. These phase differences arising from the coupling reactance are frequency dependent. To check for this issue, we measure the ratio of the symmetric to anti-symmetric components. As shown in Fig. 6.11d, this ratio remains relatively constant from 5 GHz to 10 GHz indicating that the drive and response phase is relatively constant.

6.8 High Bias Magnetoresistance

Measuring the resistance as a function of field at a high DC bias can be used to give early evidence of large angle precession. During auto-oscillations the cone angle of the magnetization opens up. The dynamically changing magnetization results in a decrease in the static magnetization and therefore a change in the sample resistance[89, 90].

Figure 6.12a shows the resistance vs field of a Pt/FM based wire with field applied perpendicular to the wire in the xy plane. For this measurement a low current bias is used and the loop shows a symmetric behavior about zero field. In contrast, Fig.6.12b shows the resistance vs field measured at a high bias where this symmetry is broken due to the spin Hall effect. For the polarity of current applied, positive field corresponds to a damping condition and the negative to anti-damping.

In the case of the planar Hall torque, a given polarity current gives the same type of action for positive and negative fields. However, traces of auto oscillations can still be seen in these measurements. In Fig. 6.12c, magnetic field is applied at an angle where PHT is maximal and a large anti-damping current is applied. The trace taken shows a rough behavior with large jumps at low field. In comparison, Fig. 6.12d shows the case for high damping-like current. The curve now appears much smother with the large jumps near zero field disappearing.

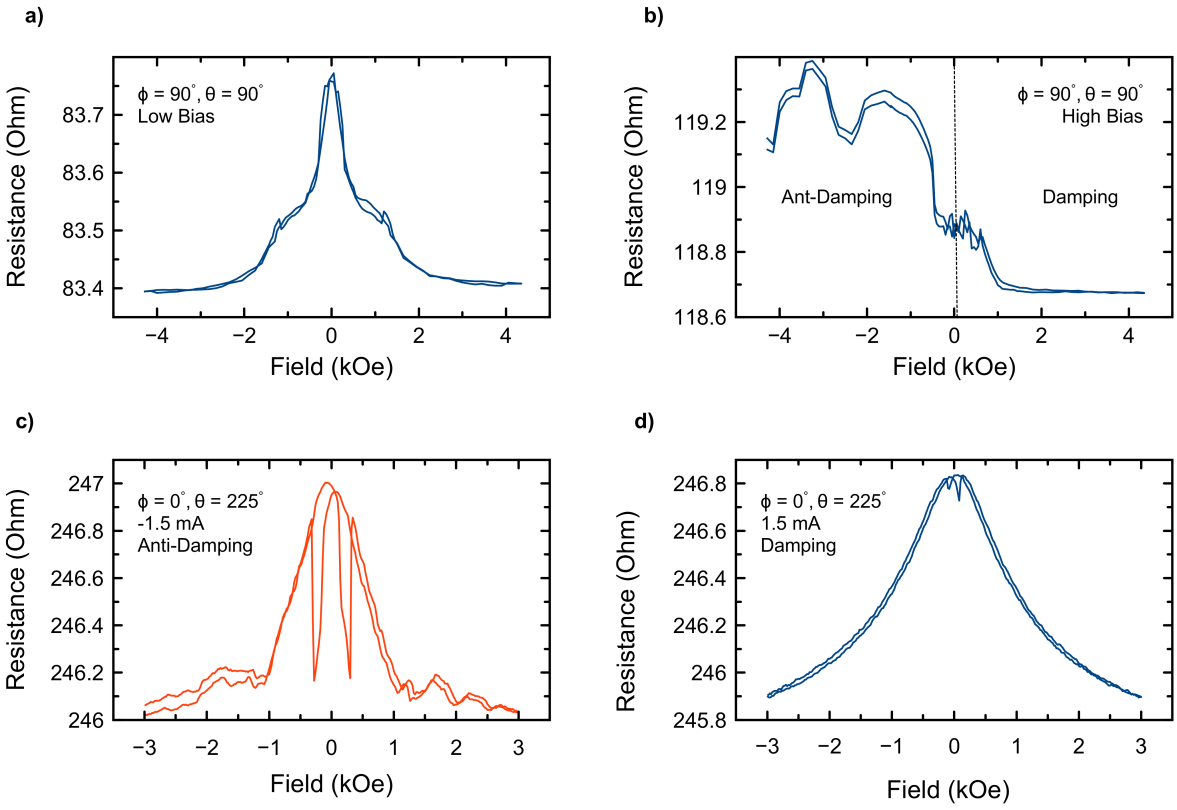

Figure 6.12: Resistance vs field for a Pt/FM sample with field applied in the xy plane perpendicular to the wire at **a)** low bias current and **b)** high current bias. Resistance vs field for Ta/Au/FM sample with **c)** anti-damping and **d)** damping currents.

Conclusion

In conclusion, spin torque oscillators hold potential as nanoscale sources of microwave power. These devices rely on the modification and eventual canceling of damping in a ferromagnetic material through the use of spin polarized currents. Traditionally, spin filtering or the spin Hall effect has been used to achieve this state. In this manuscript, the creation of spin torque oscillators has been achieved using two novel means. One through the harnessing of thermal gradients to generate a spin current via the spin Seebeck effect. Second, through the planar Hall effect found in ferromagnetic metals. The addition of new drives for spin torque oscillators should greatly expand the class of materials that can be used for spintronics applications. Further work involving the optimization of the planar Hall torque is expected to greatly expand its efficiency and theoretical modeling of its microscopic mechanism will be of great scientific interest.

Bibliography

[1] Slonczewski, J. Current-driven excitation of magnetic multilayers. *J. Magn. Magn. Mater.* **159**, L1–L7 (1996).

[2] Berger, L. Emission of spin waves by a magnetic multilayer traversed by a current. *Phys. Rev. B* **54**, 9353–9358 (1996).

[3] Sun, J. Z. Current-driven magnetic switching in manganite trilayer junctions. *J. Magn. Magn. Mater.* **202**, 157–162 (1999).

[4] Miron, I. M. *et al.* Perpendicular switching of a single ferromagnetic layer induced by in-plane current injection. *Nature* **476**, 189–193 (2011).

[5] Worledge, D. C. *et al.* Spin torque switching of perpendicular Ta—CoFeB—MgO-based magnetic tunnel junctions. *Appl. Phys. Lett.* **98**, 98–101 (2011).

[6] Liu, L. *et al.* Spin-Torque Switching with the Giant Spin Hall Effect of Tantalum. *Science (80-.).* **336**, 555–558 (2012).

[7] Landau, L. & Lifshits, E. on the Theory of the Dispersion of Magnetic Permeability in Ferromagnetic Bodies. *Phys. Zeitsch. der Sow.* **169**, 14–22 (1935).

[8] Gilbert, T. A lagrangian formulation of the gyromagnetic equation of the magnetization field. *Phys. Rev.* **100**, 1243 (1955).

[9] Kiselev, S. I. *et al.* Microwave oscillations of a nanomagnet driven by a spin-polarized current. *Nature* **425**, 380–383 (2003).

[10] Petit, S. *et al.* Spin-torque influence on the high-frequency magnetization fluctuations in magnetic tunnel junctions. *Phys. Rev. Lett.* **98**, 3–6 (2007).

[11] Liu, L., Moriyama, T., Ralph, D. C. & Buhrman, R. A. Spin-torque ferromagnetic resonance induced by the spin Hall effect. *Phys. Rev. Lett.* **106**, 1–4 (2011).

[12] Demidov, V. E. *et al.* Magnetic nano-oscillator driven by pure spin current. *Nat. Mater.* **11**, 1028–1031 (2012).

[13] Liu, L., Pai, C. F., Ralph, D. C. & Buhrman, R. A. Magnetic oscillations driven by the spin hall effect in 3-terminal magnetic tunnel junction devices. *Phys. Rev. Lett.* **109**, 1–5 (2012).

[14] Duan, Z. *et al.* Nanowire spin torque oscillator driven by spin orbit torques. *Nat. Commun.* **5**, 5616 (2014).

[15] Collet, M. *et al.* Generation of coherent spin-wave modes in yttrium iron garnet microdiscs by spin-orbit torque. *Nat. Commun.* **7**, 10377 (2016).

[16] Safranski, C. *et al.* Spin caloritronic nano-oscillator. *Nat. Commun.* **8**, 117 (2017).

[17] Thirion, C., Wernsdorfer, W. & Mailly, D. Switching of magnetization by nonlinear resonance studied in single nanoparticles. *Nat. Mater.* **2**, 524–527 (2003).

[18] Rivkin, K. *et al.* Physical principles of microwave assisted magnetic recording **214312** (2017).

[19] Thomson, W. On the Electro-Dynamic Qualities of Metals:–Effects of Magnetization on the Electric Conductivity of Nickel and of Iron. *Proc. R. Soc. London* **8**, 546–550 (1856).

[20] Nakayama, H. *et al.* Spin Hall Magnetoresistance Induced by a Nonequilibrium Proximity Effect. *Phys. Rev. Lett.* **110**, 1–5 (2013).

[21] Avci, C. O. *et al.* Unidirectional spin Hall magnetoresistance in ferromagnet/normal metal bilayers. *Nat. Phys.* **11**, 570–575 (2015).

[22] Baibich, M. N. *et al.* Giant magnetoresistance of (001)Fe/(001)Cr magnetic superlattices. *Phys. Rev. Lett.* **61**, 2472–2475 (1988).

[23] Binasch, G., Grünberg, P., Saurenbach, F. & Zinn, W. Enhanced magnetoresistance in layered magnetic structures with antiferromagnetic interlayer exchange. *Phys. Rev. B* **39**, 4828–4830 (1989).

[24] Miyazaki, T. & Tezuka, N. Giant magnetic tunneling effect in Fe/Al2O3/Fe junction. *J. Magn. Magn. Mater.* **139**, 94–97 (1995).

[25] Moodera, J. S., Kinder, L. R., Wong, T. M. & Meservey, R. Large magnetoresistance at room temperature in ferromagnetic thin film tunnel junctions. *Phys. Rev. Lett.* **74**, 3273–3276 (1995).

[26] Tsoi, M. *et al.* Excitation of a magnetic multilayer by an electric current. *Phys. Rev. Lett.* **80**, 4281–4284 (1998).

[27] Butler, W. H., Zhang, X.-G., Schulthess, T. C. & MacLaren, J. M. Spin-dependent tunneling conductance of Fe—MgO—Fe sandwiches. *Phys. Rev. B* **63**, 054416 (2001).

[28] Dyakonov, M. I. & Perel, V. I. Possibility of orientating electron spins with current. *Sov. Phys. JETP Lett.* **13**, 467 (1971).

[29] Hamadeh, A. *et al.* Full control of the spin-wave damping in a magnetic insulator using spin-orbit torque. *Phys. Rev. Lett.* **113**, 1–5 (2014).

[30] Uchida, K. I. *et al.* Observation of longitudinal spin-Seebeck effect in magnetic insulators. *Appl. Phys. Lett.* **97** (2010).

[31] Xiao, J., Bauer, G. E. W., Uchida, K.-c., Saitoh, E. & Maekawa, S. Theory of magnon-driven spin Seebeck effect. *Phys. Rev. B* **81**, 214418 (2010).

[32] Hoffman, S., Sato, K. & Tserkovnyak, Y. Landau-Lifshitz theory of the longitudinal spin Seebeck effect. *Phys. Rev. B - Condens. Matter Mater. Phys.* **88**, 1–8 (2013).

[33] Rezende, S. M. *et al.* Magnon spin-current theory for the longitudinal spin-Seebeck effect. *Phys. Rev. B - Condens. Matter Mater. Phys.* **89**, 1–10 (2014).

[34] Bender, S. A. & Tserkovnyak, Y. Thermally driven spin torques in layered magnetic insulators. *Phys. Rev. B - Condens. Matter Mater. Phys.* **93**, 1–6 (2016).

[35] Lu, L., Sun, Y., Jantz, M. & Wu, M. Control of ferromagnetic relaxation in magnetic thin films through thermally induced interfacial spin transfer. *Phys. Rev. Lett.* **108**, 1–5 (2012).

[36] Jungfleisch, M. B. *et al.* Heat-induced damping modification in yttrium iron garnet/platinum hetero-structures. *Appl. Phys. Lett.* **102** (2013).

[37] Lauer, V. *et al.* Auto-oscillations in YIG/Pt microstructures driven by the spin Seebeck effect arXiv:1612.07305 (2016).

[38] McGuire, T. & Potter, R. Anisotropic Magnetoresistance in Ferromagnetic 3d Alloys. *IEEE Trans. Magn.* **11**, 1018–1038 (1975).

[39] Taniguchi, T., Grollier, J. & Stiles, M. D. Spin-Transfer Torques Generated by the Anomalous Hall Effect and Anisotropic Magnetoresistance. *Phys. Rev. Appl.* **3**, 1–18 (2015).

[40] Kokado, S., Tsunoda, M., Harigaya, K. & Sakuma, A. Anisotropic magnetoresistance effects in Fe, Co, Ni, Fe 4N, and half-metallic ferromagnet: A systematic analysis. *J. Phys. Soc. Japan* **81**, 1–17 (2012).

[41] Tulapurkar, A. A. *et al.* Spin-torque diode effect in magnetic tunnel junctions. *Nature* **438**, 339–342 (2005).

[42] Sankey, J. C. *et al.* Spin-transfer-driven ferromagnetic resonance of individual nanomagnets. *Phys. Rev. Lett.* **96**, 50–53 (2006).

[43] Chiba, T., Bauer, G. E. & Takahashi, S. Current-Induced Spin-Torque Resonance of Magnetic Insulators. *Phys. Rev. Appl.* **2**, 034003 (2014).

[44] Gonçalves, A. M. *et al.* Spin torque ferromagnetic resonance with magnetic field modulation. *Appl. Phys. Lett.* **103** (2013).

[45] Tsunegi, S. *et al.* Self-Injection Locking of a Vortex Spin Torque Oscillator by Delayed Feedback. *Sci. Rep.* **6**, 1–7 (2016).

[46] Donahue, M. J. & Porter, D. G. OOMMF User's Guide, Version 1.0. *National Institute of Standards and Technology, Gaithersburg, MD Interagency Report* **NISTIR 6376** (1999).

[47] Vansteenkiste, A. *et al.* The design and verification of MuMax3. *AIP Adv.* **4**, 107133 (2014).

[48] Venkat, G. *et al.* Proposal for a standard micromagnetic problem: Spin wave dispersion in a magnonic waveguides. *IEEE Trans. Magn.* **49**, 524–529 (2013).

[49] Safranski, C. J., Chen, Y.-J., Krivorotov, I. N. & Sun, J. Z. Material parameters of perpendicularly magnetized tunnel junctions from spin torque ferromagnetic resonance techniques. *Appl. Phys. Lett.* **109**, 132408 (2016).

[50] Chang, H. *et al.* Nanometer-Thick Yttrium Iron Garnet Films With Extremely Low Damping. *IEEE Magn. Lett.* **5**, 6700 (2014).

[51] Barsukov, I. *et al.* Magnetic phase transitions in Ta/CoFeB/MgO multilayers. *Appl. Phys. Lett.* **106** (2015).

[52] Yang, H. *et al.* Electron beam lithography of HSQ/PMMA bilayer resists for negative tone lift-off process. *Microelectron. Eng.* **85**, 814–817 (2008).

[53] Ngyuyen, M. H., Zhao, M., Ralph, D. C. & Buhrman, R. A. APS March Meeting 2016, http://meetings.aps.org/link/BAPS.2016.MAR.K18.8 .

[54] Evelt, M. *et al.* Spin Hall-induced auto-oscillations in ultrathin YIG grown on Pt. *Sci. Rep.* **8**, 1269 (2018).

[55] Arora, M. *et al.* Magnetic properties of Co/Ni multilayer structures for use in STT-RAM. *J. Phys. D. Appl. Phys.* **50**, 505003 (2017).

[56] Daalderop, G. H. O., Kelly, P. J. & den Broeder, F. J. A. Prediction and Confirmation of Perpendicular Magnetic Anisotropy in Co/Ni Multilayers. *Phys. Rev. Lett.* **68**, 682–685 (1992).

[57] Arora, M., Hübner, R., Suess, D., Heinrich, B. & Girt, E. Origin of perpendicular magnetic anisotropy in Co/Ni multilayers. *Phys. Rev. B* **96**, 024401 (2017).

[58] Montoya, E., McKinnon, T., Zamani, A., Girt, E. & Heinrich, B. Broadband ferromagnetic resonance system and methods for ultrathin magnetic films. *J. Magn. Magn. Mater.* **356**, 12–20 (2014).

[59] Montoya, E. *et al.* Magnetization Dynamics. In Camley, R. E., Celinski, Z. & Stamps, R. L. (eds.) *Magn. Surfaces, Interfaces, Nanoscale Mater.*, vol. 5, chap. 3, 113–167 (Elsevier B.V., 2015), 1 edn.

[60] Heinrich, B. & Cochran, J. Ultrathin metallic magnetic films: magnetic anisotropies and exchange interactions. *Adv. Phys.* **42**, 523–639 (1993).

[61] McMichael, R. D., Twisselmann, D. J. & Kunz, A. Localized Ferromagnetic Resonance in Inhomogeneous Thin Films. *Phys. Rev. Lett.* **90**, 227601 (2003).

[62] Heinrich, B. Spin Relaxation in Magnetic Metallic Layers and Multilayers. In Bland, J. A. C. & Heinrich, B. (eds.) *Ultrathin Magn. Struct.*, vol. III, chap. 5, 143–206 (Springer-Verlag, Berlin/Heidelberg, 2005).

[63] Urban, R., Woltersdorf, G. & Heinrich, B. Gilbert Damping in Single and Multilayer Ultrathin Films: Role of Interfaces in Nonlocal Spin Dynamics. *Phys. Rev. Lett.* **87**, 217204 (2001).

[64] Šimánek, E. & Heinrich, B. Gilbert damping in magnetic multilayers. *Phys. Rev. B* **67**, 144418 (2003).

[65] Tserkovnyak, Y., Brataas, A., Bauer, G. E. W. & Halperin, B. I. Nonlocal magnetization dynamics in ferromagnetic heterostructures. *Rev. Mod. Phys.* **77**, 1375–1421 (2005).

[66] Yang, J. K. W. & Berggren, K. K. Using high-contrast salty development of hydrogen silsesquioxane for sub-10-nm half-pitch lithography. *J. Vac. Sci. Technol. B Microelectron. Nanom. Struct.* **25**, 2025 (2007).

[67] Gredig, T., Krivorotov, I. N., Eames, P. & Dahlberg, E. D. Unidirectional coercivity enhancement in exchange-biased Co/CoO. *Appl. Phys. Lett.* **81**, 1270–1272 (2002).

[68] Schreier, M. *et al.* Current heating induced spin Seebeck effect. *Appl. Phys. Lett.* **103** (2013).

[69] COMSOL Multiphysics v. 4.3a. www.comsol.com. COMSOL AB, Stockholm, Sweden.

[70] Slack, G. A. & Oliver, D. W. Thermal conductivity of garnets and phonon scattering by rare-earth ions. *Phys. Rev. B* **4**, 592–609 (1971).

[71] Zhang, X. *et al.* Experimental studies on thermal and electrical properties of platinum nanofilms. *Chin. Phys. Lett.* **23**, 936–938 (2006).

[72] Warkusz, F. The size effect and the temperature coefficient of resistance in thin films. *J. Phys. D: Appl. Phys.* **11**, 689–694 (1978).

[73] Furukawa, G. T., Reilly, M. L. & Gallagher, J. S. Critical analysis of heatcapacity data and evaluation of thermodynamic properties of ruthenium, rhodium, palladium, iridium, and platinum from 0 to 300 K. A survey of the literature data on osmium. *J. Phys. Chem. Ref. Data* **3**, 163–209 (1974).

[74] Bayer, C. *et al.* Spin-wave excitations in finite rectangular elements of Ni80Fe20. *Phys. Rev. B* **72**, 064427 (2005).

[75] Duan, Z. *et al.* Spin wave eigenmodes in transversely magnetized thin film ferromagnetic wires. *Phys. Rev. B - Condens. Matter Mater. Phys.* **92**, 1–10 (2015).

[76] McMichael, R. D. A mean-field model of extrinsic line broadening in ferromagnetic resonance. *J. Appl. Phys.* **103**, 07B114 (2008).

[77] Bartell, J. M. *et al.* Imaging Magnetization Structure and Dynamics in Ultrathin Y3Fe5 O12/Pt Bilayers with High Sensitivity Using the Time-Resolved Longitudinal Spin Seebeck Effect. *Phys. Rev. Appl.* **7**, 1–8 (2017).

[78] Divinskiy, B. *et al.* Nanoconstriction spin-Hall oscillator with perpendicular magnetic anisotropy. *Appl. Phys. Lett.* **111**, 032405 (2017).

[79] Slavin, A. & Tiberkevich, V. Nonlinear Auto-Oscillator Theory of Microwave Generation by Spin-Polarized Current. *IEEE Trans. Magn.* **45**, 1875–1918 (2009).

[80] Naletov, V. V. *et al.* Identification and selection rules of the spin-wave eigenmodes in a normally magnetized nanopillar. *Phys. Rev. B - Condens. Matter Mater. Phys.* **84**, 1–23 (2011).

[81] Hoffmann, A. Spin Hall Effects in Metals. *IEEE Trans. Magn.* **49**, 5172–5193 (2013).

[82] Manchon, A., Koo, H. C., Nitta, J., Frolov, S. M. & Duine, R. A. New perspectives for Rashba spin orbit coupling. *Nat. Publ. Gr.* **14**, 871–882 (2015).

[83] Ralph, D. C. & Stiles, M. D. Spin transfer torques. *J. Magn. Magn. Mater.* **320**, 1190–1216 (2008).

[84] Kurt, H., Venkatesan, M. & Coey, J. M. Enhanced perpendicular magnetic anisotropy in Co/Ni multilayers with a thin seed layer. *J. Appl. Phys.* **108** (2010).

[85] Zhang, P., Xie, K., Lin, W., Wu, D. & Sang, H. Anomalous Hall effect in Co/Ni multilayers with perpendicular magnetic anisotropy. *Appl. Phys. Lett.* **104** (2014).

[86] MacNeill, D. *et al.* Control of spinorbit torques through crystal symmetry in WTe2/ferromagnet bilayers. *Nat. Phys.* **13**, 300–305 (2016).

[87] Kurebayashi, H. *et al.* An antidamping spin-orbit torque originating from the Berry curvature. *Nat. Nanotechnol.* **9**, 211–217 (2014).

[88] Sklenar, J. *et al.* Unidirectional spin-torque driven magnetization dynamics. *Phys. Rev. B* **95**, 224431 (2017).

[89] Langenfeld, S. *et al.* Exchange magnon induced resistance asymmetry in permalloy spin-Hall oscillators. *Appl. Phys. Lett.* **108**, 192402 (2016).

[90] Li, T. *et al.* Origin of threshold current density for asymmetric magnetoresistance in Pt/Py bilayers. *Appl. Phys. Express* **10**, 073001 (2017).

Appendix A

Resist Recipes

This section details the recipes for spinning and developing the types of resists used in this study.

A.1 MAN-2401

MAN-2401 is a useful negative resist that can be removed making it good for a hard mask. It is UV sensitive so best to avoid exposure. The recipe to use is as follows:

- **Clean:** Ensure the surface of the chip is clean. If not sonicate in acetone then isopropyl alcohol.
- **Spin Coating:** Spin at 3500 rpm for 45 seconds.
- **Bake:** Bake the sample on a hotplate for 60 seconds at 90 degrees C.
- **EBL Writing:** The general dosage for this resist ranges from 250 - 300 in the NPGS software.

- **Development:** The devolper for this is maD-525 and is used for 60 seconds. Then rinse with HPLC water for 3 minutes. Sometimes extra development is needed and this is done in an as needed manner.
- **Removal:** Sometimes can be removed with acetone but usually needed oxygen plasma cleaning to be removed. If it does not need to be removed for another fab step, the wirebonder can easily make contact through the resist.

A.2 PMMA

PMMA is a versatile positive resist that is commonly used for EBL.

- **Clean:** Ensure the surface of the chip is clean. If not sonicate in acetone then isopropyl alcohol.
- **Prebake:** Prebake the sample on the hotplate for 1.5 minutes at 180 degrees C.
- **Spin Coating:** Spin at 3500 rpm for 45 seconds.
- **Bake:** Bake the sample on a hotplate for 1.5 minutes at 180 degrees C.
- **EBL Writing:** The general dosage for this resist is around 300 in the NPGS software.
- **Development:** The devolper for this is a 1:3 volume mix of methyl isobutal keytone and isopropyl alcohol. Development time is roughly 45 seconds. Clean the sample immediately after development with isopropyl alcohol.
- **Removal:** Usually acetone works well. Soak for at least 30 minutes.

A.3 MMA

PMMA is a versatile positive resist that is commonly used for EBL.

- **Clean:** Ensure the surface of the chip is clean. If not sonicate in acetone then isopropyl alcohol.
- **Prebake:** Prebake the sample on the hotplate for 1.5 minutes at 180 degrees C.
- **Spin Coating:** Spin at 3500 rpm for 45 seconds.
- **Bake:** Bake the sample on a hotplate for 1.5 minutes at 180 degrees C.
- **EBL Writing:** The general dosage for this resist is around 300 in the NPGS software.
- **Development:** The devolper for this is a 1:3 volume mix of methyl isobutal keytone and isopropyl alcohol. Development time is roughly 45 seconds. Clean the sample immediately after development with isopropyl alcohol.
- **Removal:** Usually acetone works well. Soak for at least 30 minutes.

A.4 HSQ

HSQ is a high resolution negative resist that forms a material similar to silicone oxide when developed. It has a time limit from when spun so for long writes is not desirable.

- **Clean:** Ensure the surface of the chip is clean. Argon rf cleaning in the sputter system greatly improves adhesion.
- **Prebake:** None

- **Spin Coating:** Spin at 4000 rpm for 45 seconds.
- **Bake:** None. The MIBK solvent is volitile and resist will dry on its own.
- **EBL Writing:** The general dosage for this resist is around 2000-7500 in the NPGS software depending on feature size.
- **Postbake:** None
- **Development:** The devolper for this is 0.5 wt % NaOH and 2.0 wt % NaCl. Development time is 3 minutes. Take care not to agitate during development. Clean the sample immediately after development with HPLC water.